January 2020

Exploration Of Model-Resolution Dependence Of Forecasted Wind Hazards For Small Unmanned Aircraft System Operations

Lucas Andrew Reilly

EXPLORATION OF MODEL-RESOLUTION DEPENDENCE OF FORECASTED WIND HAZARDS FOR SMALL UNMANNED AIRCRAFT SYSTEM OPERATIONS

by

Lucas Andrew Reilly

Bachelor of Science, State University of New York at Oswego, 2018

A Thesis

Submitted to the Graduate Faculty

of the

University of North Dakota

in partial fulfillment of the requirements

for the degree of

Master of Science

Grand Forks, North Dakota

August

2020

Name: Lucas Reilly

Degree: Master of Science

This document, submitted in partial fulfillment of the requirements for the degree from the University of North Dakota, has been read by the Faculty Advisory Committee under whom the work has been done and is hereby approved.

DocuSigned by:
Mark Askelson
903659E33D54466...
Dr. Mark Askelson

DocuSigned by:
Catherine Finley
9AB547FA88FB427...
Dr. Catherine Finley

DocuSigned by:
Mounir Chrit
85189FBD9AD740E...
Dr. Mounir Chrit

This document is being submitted by the appointed advisory committee as having met all the requirements of the School of Graduate Studies at the University of North Dakota and is hereby approved.

DocuSigned by:
Chris Nelson
2E0AF088C733403...
Chris Nelson
Dean of the School of Graduate Studies

7/27/2020
Date

PERMISSION

Title	Exploration of Model-Resolution Dependence of Forecasted Wind Hazards for Small Unmanned Aircraft System Operations
Department	Atmospheric Sciences
Degree	Master of Science

In presenting this thesis in partial fulfillment of the requirements for a graduate degree from the University of North Dakota, I agree that the library of this University shall make it freely available for inspection. I further agree that permission for extensive copying for scholarly purposes may be granted by the professor who supervised my thesis work or, in his absence, by the Chairperson of the department or the dean of the School of Graduate Studies. It is understood that any copying or publication or other use of this thesis or part thereof for financial gain shall not be allowed without my written permission. It is also understood that due recognition shall be given to me and to the University of North Dakota in any scholarly use which may be made of any material in my thesis.

Lucas Andrew Reilly

July 30th, 2020

TABLE OF CONTENTS

LIST OF FIGURES vii

LIST OF TABLES ix

ACKNOWLEDGMENTS x

ABSTRACT xi

1. INTRODUCTION 1

2. sUAS CHARACTERISTICS AND HAZARDS 4

3. TOPOGRAPHY 13

a. Gap Flow 13

b. Valley Circulation 14

c. Wind Channeling 16

d. Valley Flow Mechanisms 16

4. METHODS 19

a. WRF Model Details 20

b. New York State Mesonet and Verification 32

c. Processing 37

5. RESULTS 41

a. Verification 41

b. Wind Speed 48

c. Wind Direction 53

d. Vertical Velocity 58

e. Temperature 61

f. Airflow Stability 65

6. DISCUSSION 68

a. Future Work 77

7. CONCLUSIONS 78

APPENDIX 81

REFERENCES 83

LIST OF FIGURES

Fig. 1. MSL Terrain Map with Topographic Feature Labels. 2

Fig. 2. sUAS Yaw, Pitch, and Roll. 8

Fig. 3. sUAS Maximum Flight Speeds from Ranquist et al. (2017) 9

Fig. 4. PBL Components and Evolution from Markowski and Richardson (2010). 11

Fig. 5. sUAS Encountering a Downdraft. 12

Fig. 6. sUAS Encountering an Updraft. 12

Fig. 7. Valley Circulation Evolution from Markowski and Richardson (2010). 15

Fig. 8. Valley Flow Mechanism Wind Directions from Whiteman and Doran (1993). 18

Fig. 9. WPC Surface SLP and Precipitation Analysis. 22

Fig. 10. WRF Nested Domain Structure. 23

Fig. 11. Comparison of Default and Utilized Model Vertical Levels. 29

Fig. 12. NYSM Station Locations 33

Fig. 13. Detailed Terrain Contours and Model Cross-Sectional Areas. 38

Fig. 14. Hourly Model 10 m Wind Speed (m s^{-1}) Errors. 43

Fig. 15. Five-Minute Model 10 m Wind Speed (m s^{-1}) Errors. 45

Fig. 16. Binned Five-Minute Wind Speed Data Comparison. 46

Fig. 17. Hourly 10 m Wind Direction (°) Comparison of Observations and Model Data. 48

Fig. 18. Average Low-Level Wind Speed (m s^{-1}) of Model Subdomains at 13 UTC. 49

Fig. 19. Average Low-Level Wind Speed (m s^{-1}) of Model Subdomains at 21 UTC. 50

Fig. 20. North-South Cross-Sections of Wind Speed (m s^{-1}) at 13 UTC. 52

Fig. 21. North-South Cross-Sections of Wind Speed (m s^{-1}) at 21 UTC. 53

Fig. 22. Average Low-Level Wind Direction (°) of Model Subdomains at 13 UTC. 54

Fig. 23. Average Low-Level Wind Direction (°) of Model Subdomains at 21 UTC. 55

Fig. 24. North-South Cross-Sections of Wind Direction (°) at 13 UTC. 57

Fig. 25. North-South Cross-Sections of Wind Direction (°) at 21 UTC. 58

Fig. 26. North-South Cross-Sections of Vertical Velocity (cm s^{-1}) at 13 UTC. 60

Fig. 27. North-South Cross-Sections of Vertical Velocity (cm s^{-1}) at 21 UTC. 61

Fig. 28. Model Produced Skew-T Log-P Graphs for WEST at 13 UTC. 63

Fig. 29. Average Low-Level Temperature (°F) of Model Subdomains at 13 UTC. 64

Fig. 30. North-South Cross-Sections of Temperature (°F) at 13 UTC. 65

Fig. 31. West-East Cross-Sections of R_B (unitless) at 13 UTC. 67

Fig. 32. West-East Cross-Sections of R_B (unitless) at 21 UTC. 68

Fig. 33. 1.33 km Model Domain Vertical Velocity (cm s^{-1}) at 13 UTC with Cressman Weighting Function Applied. 74

Fig. 34. 10 m Wind Barbs (m s^{-1}) for Model Subdomains at 13 UTC 76

LIST OF TABLES

Table 1. Model Characteristics and Parameterizations. 21

Table 2. Developed Scripts and Their Purpose. 40

Table 3. Hourly Error Statistics. 44

Table 4. Five-Minute Error Statistics 44

ACKNOWLEDGMENTS

The present work could not have been done without the encouragement, input, and guidance from many individuals. In no particular order: my parents and sister, Kathy, Tim, and Kimber Reilly; my soulmate, Norah Mattice; my advisor, Dr. Mark Askelson; members of my committee, Dr. Mounir Chrit and Dr. Cathy Finley; the original inspiration for this work, TruWeather Solutions CEO Don Berchoff; local modeling expert, Dr. Gretchen Mullendore; and all of my past teachers and peers who helped bestow their expertise upon me. Special thanks extend to all of you, including whoever may be reading this – thank you!

The University of North Dakota has proven extremely helpful in providing a productive atmosphere that allowed for personal efficiency. Hockey! Hockey! Hockey! Oi! Oi! Oi!

NCAR CISL supercomputing was essential in providing the necessary computing power for this experiment. I would like to thank all the staff at these facilities that worked to answer my questions and keep the Cheyenne supercomputer running efficiently.

This work was made possible by the New York State (NYS) Mesonet. Original funding for the NYS Mesonet was provided by Federal Emergency Management Agency grant FEMA-4085-DR-NY, with the continued support of the NYS Division of Homeland Security & Emergency Services; the state of New York; the Research Foundation for the State University of New York (SUNY); the University at Albany, SUNY; the Atmospheric Sciences Research Center (ASRC) at SUNY Albany; and the Department of Atmospheric and Environmental Sciences (DAES) at SUNY Albany.

To good times, good friends, good hockey,

and most of all, great family.

ABSTRACT

Use of the small Unmanned Aircraft System (sUAS) for commercial applications is growing. Once approval is granted to conduct flights Beyond Visual Line Of Sight (BVLOS), utilization of the sUAS will accelerate. Hazards associated with sUAS flight, including weather hazards, must be understood when flying BVLOS. One of the leading weather hazards is wind. In this study, nested Weather Research and Forecasting (WRF) model simulations with horizontal grid spacings of 12 km, 4 km, 1.33 km, and 0.444 km were conducted to evaluate the impact changing resolution has on wind fields and, thus, on the forecasting of sUAS wind hazards. The simulated area lies within Central New York (CNY); the surrounding topographic features commonly generate small-scale wind patterns, creating excellent opportunities to explore the dependence of winds on model resolution. Results suggest the importance in increasing model resolution to increase sUAS safety, where a 1.33 km resolution well-identifies hazardous winds. The 0.444 km resolution resolved more detailed atmospheric features at the cost of an increase in computational power. An ensemble model approach along with human interpretation is hypothesized to best facilitate a sUAS-centric forecast.

1. INTRODUCTION

The use of the small Unmanned Aircraft System (sUAS), typically less than 55 lbs, for commercial operations is increasing. Their expected positive economic influence has elevated interest in developing a regulated airspace in which sUASs can fly safely. Flights Beyond Visual Line Of Sight (BVLOS) offer significant opportunity for commercial applications. Routine maintenance in difficult to reach areas is expected to be a value of the sUAS; these areas are likely difficult to reach due to adverse travel conditions, relevant to people but not necessarily a sUAS. Additional hazards arise when a sUAS is flown BVLOS, as flying within Line Of Sight (LOS) enables significant hazard mitigations. Efforts to mitigate BVLOS-driven hazards are promising but require guidance (whether through flight testing or simulations) in order to create the necessary systems that produce the required level of safety. The primary difference between manned and Unmanned Aircraft (UA) is the lack of an onboard pilot. Fittingly, the Federal Aviation Administration (FAA) views to handle UA rules and regulations no differently than manned aircraft. For this reason, the safety methods and regulations implemented for sUASs must allow for operations to be just as safe, if not safer, than manned aircraft flight (Askelson et al. 2013). The present study focuses on wind hazards that are expected to be associated with flying a sUAS within complex terrain regimes. The complex terrain within Central New York (CNY) was chosen for analysis in this study. Understanding wind flows and their evolution becomes necessary to a successful mission, as wind can, and has, resulted in a loss of sUAS flight control.

Complex terrain can be described by the proximity between various topographic features. In this case, CNY is characterized by the Allegheny Plateau (AP) to the south, Adirondack Mountains to the northeast, Tug Hill Plateau to the north-northeast, Lake Ontario to the northwest, and the Mohawk and St. Lawrence River Valleys that make-up its center (Fig. 1**)**. This valley

structure within the heart of CNY will be the primary area of interest and referred to as the Central Valley (CV). The CV's surrounding bounds influence wind flow patterns in numerous ways that will be discussed in the latter portions of this paper.

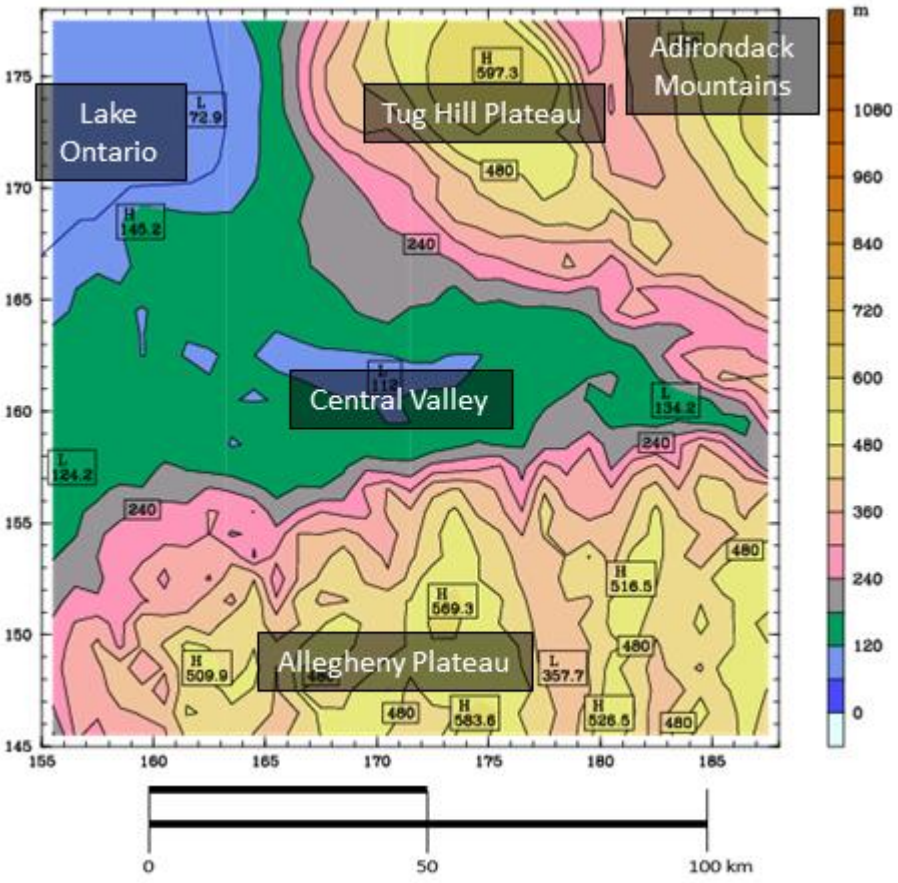

Fig. 1: MSL terrain map with topographic feature labels. The x and y axes convey the number of grid points (distance = # Grid Points × 4 km). A reference length scale is provided.

Utilization of Numerical Weather Prediction (NWP) as a tool in guiding sUAS travel is a natural solution to this problem. Understanding weather model performance in this scenario must

be investigated. Therefore, conducting a high-resolution model simulation and testing its ability to resolve momentum and subsequent turbulent evolution within the boundary layer is necessary.

A common exploration of model sensitivity involves horizontal and vertical grid spacing used within NWP. Model vertical resolution is typically held constant throughout model nests, and, thus, horizontal resolution impacts are evaluated herein. Use of the Weather Research and Forecasting (WRF) model (Skamarock et al. 2008) allows for a nested domain structure, enabling simulations using multiple horizontal grid spacing – hereinafter Δx – intervals. Decreasing Δx increases detail within model output; however, decreasing Δx to lower values leads to higher computational cost.

The primary focus is understanding wind vector sensitivities associated with decreasing Δx. To evaluate this, subsequent model nests utilize 12 km, 4 km, 1.33 km, and 0.444 km Δx values. While not an exhaustive study, as the sensitivities are subject to change with different ambient conditions, the goal of this work is to identify a Δx that enables identification of sUAS wind hazards while remaining computationally affordable.

The following paper is divided into seven chapters beginning with the previous Introduction. sUAS characteristics and associated hazards are described in Chapter 2, with an in-depth discussion regarding topography provided in Chapter 3. Chapter 4 then includes an explanation of the methodology, discussing the WRF model details and use of the New York State Mesonet (NYSM). Results and their discussion are included in Chapter 5 and Chapter 6, respectively. Conclusions for this experiment are presented within Chapter 7.

2. sUAS CHARACTERISTICS AND HAZARDS

Use of UA, as discussed by Marshall et al. (2016), has been relevant since the early 1900's when on-board systems such as the rudder, autopilot, and radio helped shape unmanned flight. Early usage, like most aviation and weather-related technology, was primarily militaristic, as the remote guided aerial torpedoes of 1916 were utilized in World War I. In general, modern UA are referred to as autonomous or remotely piloted aircraft that rely on their autopilot or transmitters, respectively.

The Unmanned Aircraft System (UAS) community uses technology that must be guided by regulations. While recreational users are not required to register their machines, doing so helps in commercializing the technology (UAS Summit 2019). In the current state of UA, situations that threaten human life or property are of particular interest. For this reason, the FAA has implemented the Part 107 regulation to provide guidelines for sUAS flight (FAA 2016). The rules include weather-related constraints pertaining to avoidance of clouds—500 ft vertically and 2000 ft horizontally, and a minimum three-mile visibility, where operations must be conducted within Visual Line Of Sight (VLOS). If suitable BVLOS capabilities are supported by the UAS, the VLOS requirement may be waived. One means for receiving a Part 107 waiver that enables BVLOS operations involves the sUAS being equipped with proper Detect And Avoid (DAA) instrumentation. This DAA technology acts to sense nearby encounters and maneuver the sUAS to avoid them. As previously stated, sUAS safety regulations must be at least equal to that of manned aircraft. Provided an on-board pilot's sight was a means to DAA with manned aircraft, UA DAA technology must act to replicate this ability (Askelson et al. 2013). The absence of such capabilities while flying BVLOS leaves a sUAS and any nearby aircraft susceptible to dangerous situations, such as a Mid-Air Collision (MAC). DAA technology is essential to ensuring the safety

of the airspace and surrounding population. Efforts to implement an automated and certified DAA system are ongoing.

General weather guidelines are vague and not summarized within Part 107, which states that operators should refer to local forecasts from reputable sources. The provided flight constraints permit operations up to 400 ft (0.121 km) Above Ground Level (AGL) or 1,600 ft AGL if within 400 ft of a structure. At these heights, atmospheric conditions are sensitive to the Planetary Boundary Layer (PBL) structure and evolution. Understanding the weather phenomena that impact the efficacy of a sUAS in the PBL must be considered. This implication provides the basis for weather parameters that must be investigated. Ranquist et al. (2017) provides an overview of weather hazards to which sUAS are typically exposed, which are described subsequently.

Weather hazards are important even when the UAS is operated within VLOS. Glare and flight between the sun and pilot can take away an operator's vision of the UA, decreasing safety. This is true for the pilot's view of both the sUAS as well as the tablet possibly being used to control it. Solar activity can also interfere with GPS and should be a general consideration when flying.

Humidity can create condensation on the electronics within an UAS, potentially leading to a loss of communication, command, and control. In addition, condensation can cause the circuitry to spark and set afire. If an UAS utilizes a partially damaged lithium polymer battery prone to hydrogen build-up, one of these sparks can trigger an explosion (Drone Registration 2016). Humidity trends vary locally as a result of geography, time of day/year, and current weather patterns; therefore, it should be considered before every flight.

Temperature variation is similar to humidity and can have significant impacts on an UAS. UAS flight operations typically occur between temperatures of 253-323 K. Flying with certain

UAS at temperatures as low as 223 K or as high as 343 K is possible, but negative hardware and performance impacts are expected. These negative impacts mainly pertain to the battery and circuitry. Higher temperatures can lead to deformation of the hardware, while lower temperatures can result in on-board materials becoming brittle and easily broken. Lower temperatures can also alter UAS communication and operation. Battery life can deplete quickly in higher temperatures, as the generation of lift inversely relates to temperature; thus, more energy is required to fly in higher temperatures. Lower temperatures lead to less overall battery capacity; even with an increase in lift generation, the overall performance/flight time of the UAS becomes limited (Warner 2015).

Having knowledge of weather conditions and how they will evolve with time is essential to a successful BVLOS mission. sUAS operations can oftentimes be visualized using an on-board camera. The effectiveness of this camera becomes limited with visibility concerns arising within clouds, fog, and haze, which may also act to blur the camera lens and increase the risk of collision. Overall, avoiding flight through condensed moisture is recommended.

Flying below clouds can expose a sUAS to precipitation, which can adversely affect operations in more ways than one. Accumulation of precipitation on a sUAS can create an uneven mass distribution. This shifting of the center of mass can result in control issues, as can any precipitation that encounters circuitry. Also, the impact of hydrometeors on the airframe creates a downward torque, resulting in a downward pitch. This effect coincides with rain intensity, as heavier rain will likely force a sUAS downwards and impact aerodynamic efficiency. It should be noted that certain airframe materials may respond poorly to intense rainfall. Hansman and Craig (1987) showed that wet conditions increased the critical angle, an angle at which an aircraft experiences stall, of the NACA 0012 airfoil by 4º. While being a larger structure, implications for

sUAS, specifically fixed-wing systems, can be assumed to be similar. Being able to identify precipitation during a BVLOS mission flight is necessary for avoiding these hazards.

While icing is less of a threat at lower elevations, it is still possible and should be considered. The most common cause of aircraft icing is supercooled water freezing onto the airframe. Icing on the wings and body increases drag and decreases lift, creating substantial flight safety issues. With a sUAS, the primary threat is rime ice (Politovich 2015), a rough and opaque form of ice that forms from droplets within low clouds/fog (FAA 1975). When considering a rotor-blade powered sUAS, rime ice tends to form on the blades themselves. Blade rotation results in a centrifugal force that acts as a de-icing method, but it can also produce problematic uneven ice distribution. This also impacts fixed-wing aircraft, as the imbalance in mass can be detrimental to flight (Brouwers et al. 2010).

Impacts of wind and turbulence are particularly relevant. While producing the greatest number of weather-related aviation accidents, windy and turbulent conditions can also lead to travel limitations. In addition to the effects of wind and turbulence through vertical and horizontal displacement, the implications upon sUAS battery life must be considered. Both factors rely on the orientation (roll, pitch, and yaw) of the aircraft (Fig. 2). These parameters define sUAS orientation in terms of aircraft control: roll pertains to rotation about the airframe's main body, pitch refers to the angle of the airframe's nose, and yaw guides the aircraft's horizontal direction. An issue arises when the prevailing wind impacts aircraft orientation and, thus, control. For example, to avoid collision with nearby structures, operators may conduct take-off in open areas that are prone to crosswinds (winds that blow across the aircraft's path). A crosswind of just 5-8 m s^{-1} can displace a larger UA aircraft on a runway, resulting in delays or even cancelation of the flight (Master Sergeant Nelson, personal communication, 27 August 2019). Exposing aircraft to

these conditions can result in the airframe flipping entirely, as the yaw and roll of the airframe are directly affected by the horizontal winds. Once airborne, winds and turbulence can continue to encourage a loss of controlled flight, impacting sUAS travel.

Fig. 2: Yaw, pitch, and roll with respect to a sUAS.

It is not unrealistic for wind speeds, especially at higher altitudes, to exceed the maximum flying speed of a sUAS (Fig. 3). On average, multi-rotor sUAS harness a maximum flight speed of about 15 m s^{-1}. The resulting loss of control can lead to stagnant flight or significant displacement, which could result in loss of VLOS. Examples of such cases are available through public video platforms (e.g., YouTube), where sUAS operators experience significant aircraft displacement, typically leading to unsafe crash landings. Multi-rotor sUASs generally have lower

maximum flight speeds than fixed wing sUAS, as indicated in Fig. 3, and they are subject to experience a loss of control within low-level wind speed regimes. sUAS are typically equipped with multiple flight modes that permit different flight speed maxima. Recreational users must enable a feature to actively switch modes and unlock higher flight speeds that may be necessary to overcome the prevailing winds. Failing to do so before flight could result in a dangerous situation.

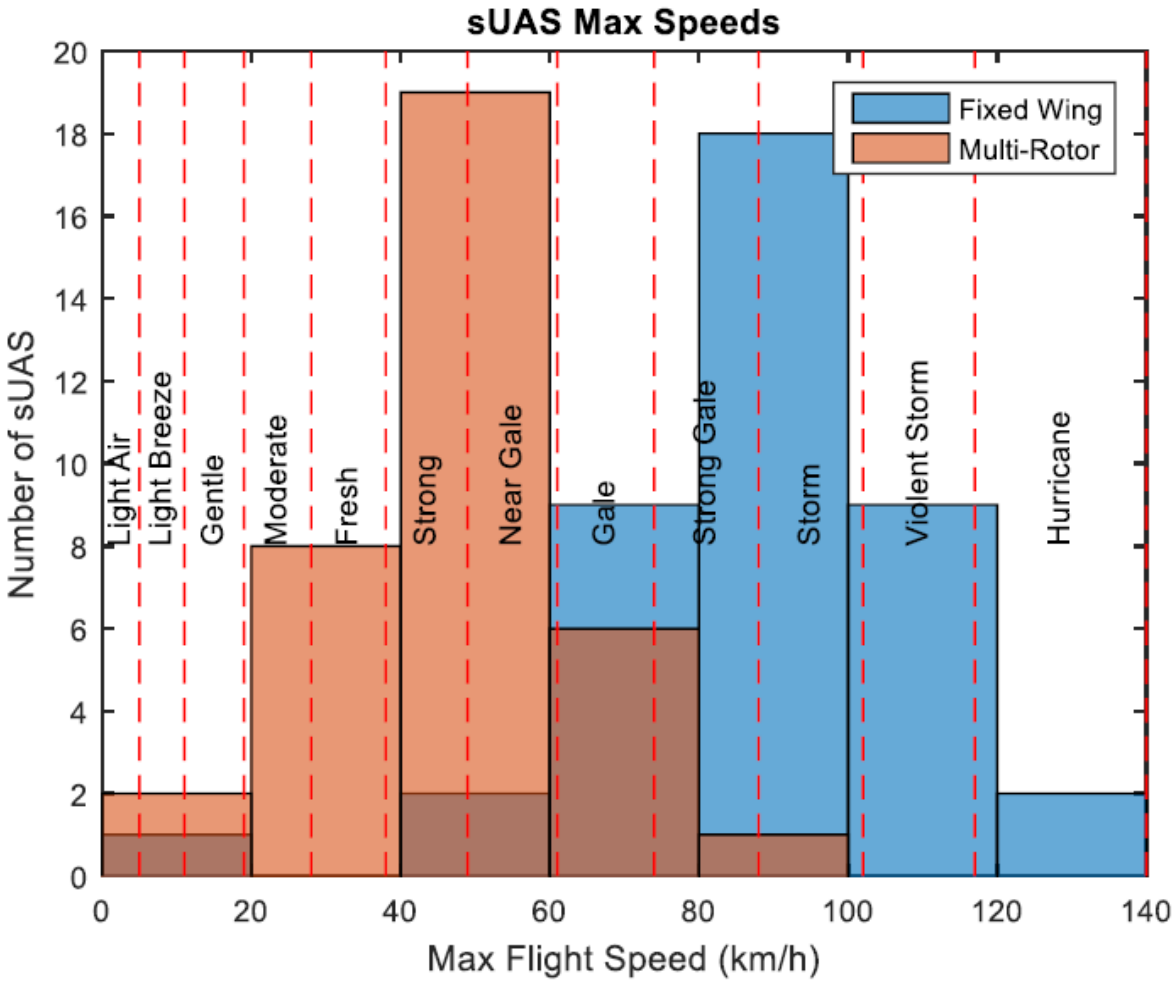

Fig. 3. Survey of 92 different sUAS maximum flight speeds with the Beaufort wind scale overlaid. The darker brown color indicates an overlap in fixed wing and multi-rotor aircraft travel speeds (1 km hr^{-1} = 0.27 m s^{-1}). Reproduced from Ranquist et al. (2017).

Maximizing battery life enables a successful and efficient mission. Headwinds require an increase in sUAS velocity, and, thus, battery life is shortened. The opposite is true for a tailwind, as less battery power is needed to fly at the intended speed. Optimizing flight path to reduce wind-related adversity can have substantial benefits. According to Master Sergeant Nelson of the Grand Forks Air Force Base, optimizing the level at which an UAS is flying can result in an efficiency increase of up to 400% (UAS Summit 2019). While this occurs with the large RQ4-B, or Global Hawk, the same principle applies to sUAS. Battery life is arguably one of the more important factors from an economic standpoint: longer flights are generally more successful/productive. In order to maximize flight duration, wind fields must be understood both prior to and during flight. Avoiding a strong headwind within the permitted flight region for a sUAS will elongate flight. Identifying a tailwind at a permitted altitude, both towards and returning from a destination, is optimal. Battery depletion as a result of fighting a headwind before returning to a safe landing location could result in a dangerous situation. Flight software often detects wind-flow adversity, but, by the time the UAS is airborne, wind speeds may quickly result in an unsafe landing condition. Maintaining flight to reach a safe landing location leaves a low battery sUAS prone to a hazardous emergency landing.

Wind gusts must also be considered, as they can be on the order of two-times larger than the sustained wind speed. Given that a wind gust can last up to 20 seconds, there is plenty of time to lose control of a sUAS (NOAA 2013). It is also important to consider the degree to which gusts and wind-fields vary spatially. Like many atmospheric features, wind-fields are stratified as well as spatially and temporally semi-chaotic. The frictional effects of surface features can disrupt wind-fields, creating phenomena such as wind tunnels and gap flow. Both meso- and micro-scale

wind features must be analyzed to assure sUAS flight safety. Consideration of the PBL is essential. The height of the PBL evolves diurnally and relies upon several environmental factors (Fig. 4). Wind speeds within the PBL generally increase with height as a result of friction. Above this friction, or surface, layer, momentum tends to be well-mixed, implying generally consistent wind speed magnitudes, dependent upon local stability, throughout what is known as the Mixed Layer (ML). Mixing coincides with vertical motions that can have detrimental impacts on sUAS flight. A strong downdraft (updraft) could immediately force the aircraft downwards (upwards) into a hazardous situation (Fig. 5). It is also possible for a vertical draft to force a sUAS into a pocket of wind speed shear (Fig. 6). Such scenarios could also lead to a MAC. Horizontal wind vectors are not guaranteed to be unidirectional as a result of variable pressure gradients that are dependent upon several environmental factors, including the local topography.

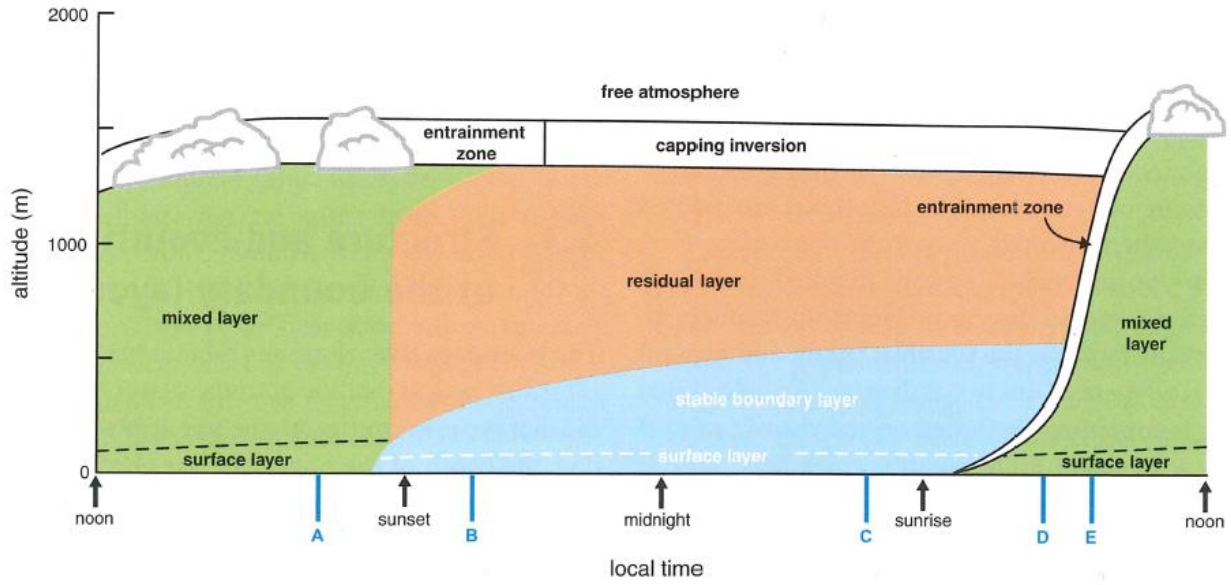

Fig. 4: Illustration of PBL diurnal evolution and its components. Figure reproduced from Markowski and Richardson (2010).

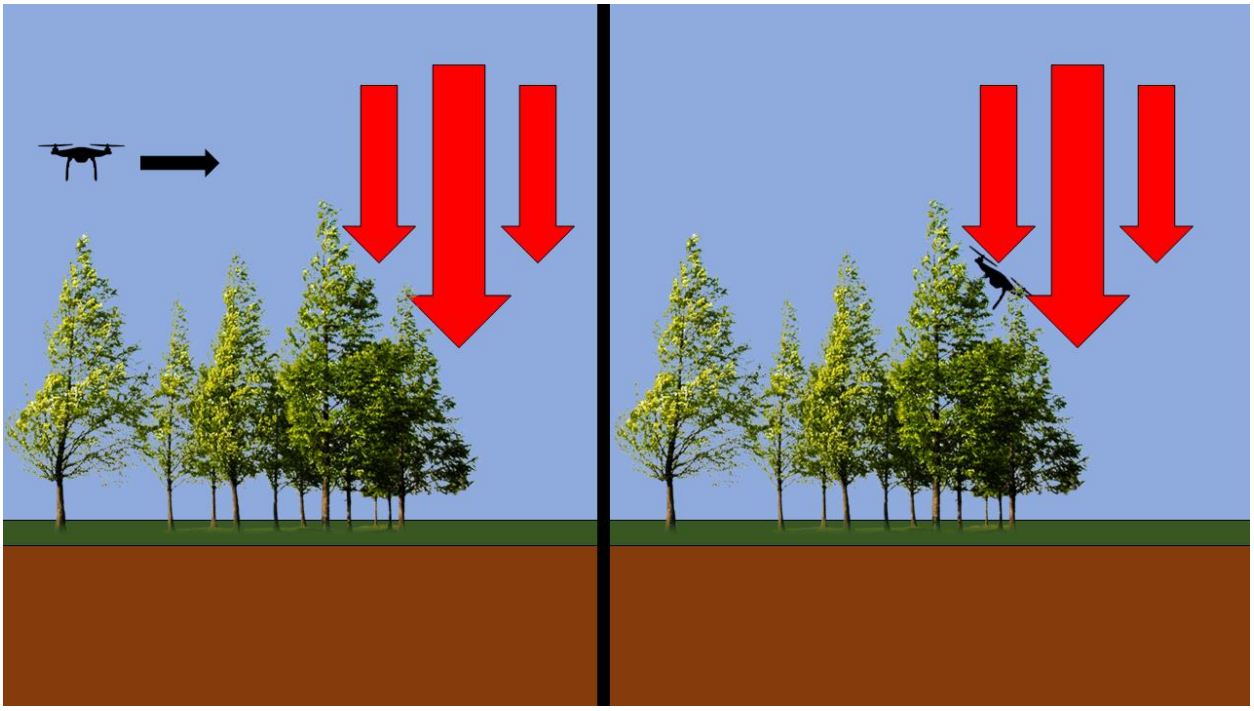

Fig. 5: Illustration of a sUAS encountering a downdraft (red vectors) that creates a hazardous situation with respect to obstacles.

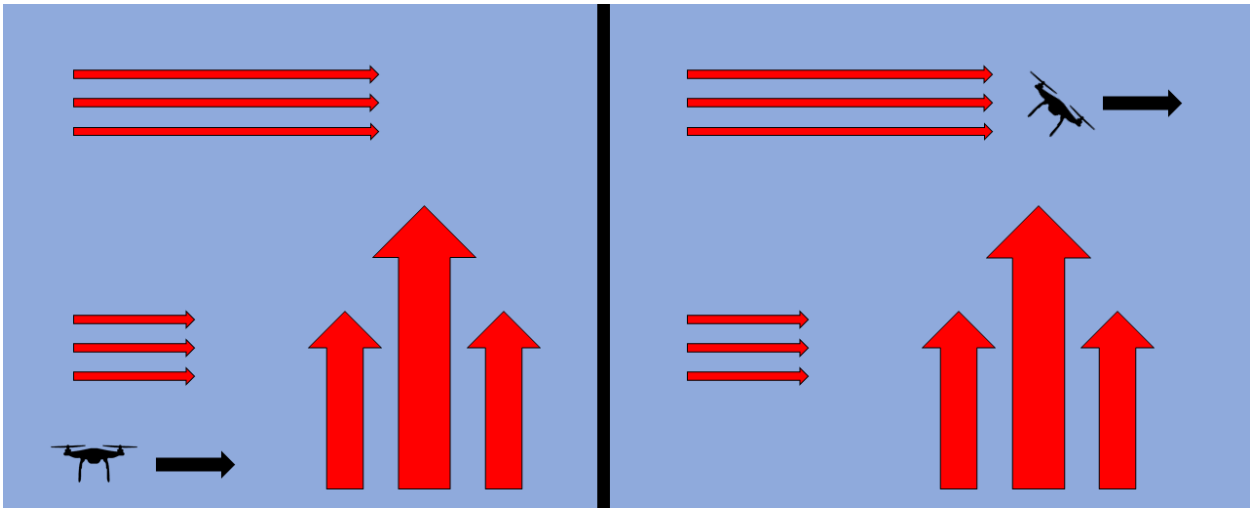

Fig. 6: Illustration of a sUAS encountering an updraft that creates a hazardous situation with respect to wind speed shear. Red vectors illustrate air flow.

3. TOPOGRAPHY

The area of interest is CNY's detailed valley system that envelops the area previously described as the CV. Most discussion will revolve around this area's complex terrain. The CV is bounded to the: south by the AP, northeast by the beginning of the Adirondack Mountains, north-northeast by the Tug Hill Plateau, and northwest by Lake Ontario (Fig. 1). This variation in topography enables production of many complex wind flow scenarios; the present experiment involves a southerly flow aloft. Thus, wind flow aloft prevails over the AP, traverses the CV, then encounters the edge of the Adirondack Mountains and Tug Hill Plateau on the leeward side of the CV. The terrain elevation drops ~400 m from the crest of the AP into the heart of the CV. The leeward climb in elevation is smoother and involves about a 500 m rise over about 58 km to the Tug Hill's cap. Within the CV wind flow is easterly, following the Mohawk Valley's drainage gradient that begins around 123 m Mean Sea Level (MSL) and sinks, with detailed height variations along the way, about 50 m downstream to Lake Ontario. Wind flow behavior as a result of this terrain variation becomes a blend of numerous, primarily valley induced factors.

a. Gap Flow

Considering the valley terrain and low-level wind flow of the present simulation, the gap flow phenomenon is briefly discussed. A gap flow typically occurs when airflow accelerates within a topographically constricted area; after exiting the area of constriction, the airflow continues to accelerate downstream of the constriction and achieves a wind speed maximum (Mayr et al. 2007). In the case of the CV, an easterly wind flow is bounded and could lead to downstream wind speed maxima.

b. Valley Circulation

Typical valley flow behavior involves a diurnally influenced wind pattern that is driven by terrain-induced temperature and pressure differences. The airflow within a valley is well covered by Rampanelli et al. (2004), and the following is largely derived from their work. A valley's large daily temperature range is primarily driven by the diurnal heating cycle. The subsequent temperature differences within the mountain-valley system drives hydrostatically-generated, pressure-gradient-based wind flows. More specifically, Weigel et al. (2006) describes the slope walls warming (cooling) at a faster rate than the valley's central air mass, creating a density driven upslope (downslope) flow. This process is known as a slope wind, of which there are usually two—one on each valley slope—that typically blow up (down) the valley walls during the day (night). Mass conservation from the resulting divergence (convergence) at the valley floor completes a circulation with sinking (rising) air within the center of the valley. Flow along the valley axis is similar, in that it rises up-valley during the day and sinks down-valley at night. The combination of the slope winds and airflow along the valley axis results in a three-dimensional circulation termed the Valley Circulation (VC) (Fig. 7). Ideal VC conditions involve weak upper-level flow and a strong diurnal cycle. Daytime subsidence warming as a result of the rising slope winds helps to increase valley air temperatures relative to adjacent plains. The process also reverses, where subsidence warming acts to drive the slope winds (Weigel et al. 2006). Provided the subsidence is strong in an unstable environment, advective heat transport within the valley can complicate temperature profiles. For example, cold air advection at the surface can act to stabilize low level air while upper level subsidence develops a strong capping inversion (Weigel et al. 2006). Inversions and their evolution are important in identifying a wind speed maximum that could become hazardous to sUAS flight. The nature of wind flow within complex topography may

involve the superposition of several mechanisms, and a subsequent valley-based PBL profile is commonly not the same as that at surrounding locations (Weigel et al. 2006).

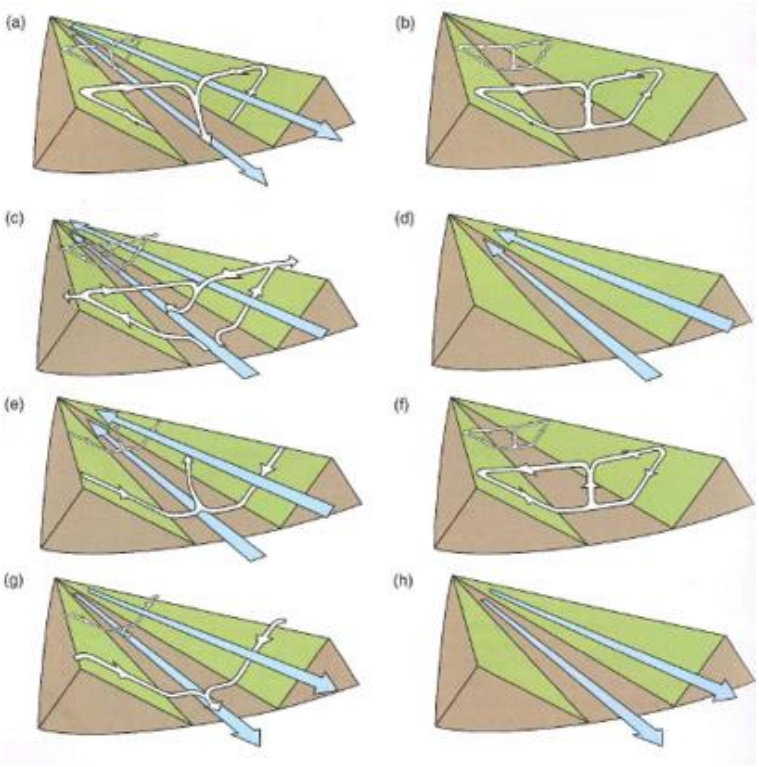

Fig. 7: Valley circulation behavior at: a) sunrise, b) mid-morning, c) early afternoon, d) late afternoon, e) evening, f) early night, g) middle of night, and h) late night. White arrows depict slope wind circulation and blue arrows convey the direction of valley axis flow. Figure reproduced from Markowski and Richardson (2010).

c. Wind Channeling

Valley wind behavior is further complicated by channeling. Wind channeling is well defined by Gross and Wipperman (1987). Airflow decelerates when entering a valley and disturbs the equilibrium between horizontal pressure gradient and Coriolis forces. The air, now within the valley, is forced to flow along the walls of the bordering topography, as the geostrophic pressure gradient's along-valley component becomes dominant. Thus, the airflow is deflected along the valley axis, resulting in a valley channeled flow. This behavior is best exhibited when wind flow is perpendicular to the valley. Channeling can be complex, as a variety of wind flow regimes, dependent on both wind speed and direction, can produce different scenarios.

d. Valley Flow Mechanisms

These scenarios are best explained by a combination of different valley wind mechanisms. Four mechanisms that influence airflow above and within a valley are defined by Whiteman and Doran (1993), each of which is well explained and relevant herein. The first mechanism is thermal forcing, which is essentially the VC. The downward transport of momentum is the second mechanism considered. An example of this mechanism occurs through gravity waves. The horizontal momentum of the winds aloft is transported downwards by gravity-wave-induced turbulent mixing that works to entrain momentum aloft into the valley's airflow. The reliance on vertical mixing inherently involves a dependence on stability, as unstable conditions are beneficial in momentum entrainment. Downward transport of momentum is noted to commonly occur in valleys that are wide and flat along their axis, like the CV. Pressure-driven channeling, the third mechanism, is synonymous to the geostrophic pressure gradient channeling behavior described above. This mechanism is very similar to the fourth mechanism: forced channeling. Forced channeling also involves the channeling of ambient winds into the valley that then align with the

valley axis. The difference involves a phenomenon known as a countercurrent, in which pressure driven channeling influences valley winds to flow in the opposite direction of winds aloft. As an example, consider a northeast to southwest valley structure. For a southerly wind flow aloft, forced channeling would involve an up-valley flow out of the southwest while a pressure-driven channeling valley flow would be down-valley, out of the northeast (Fig. 8). This quick turning of the winds associated with a strong pressure gradient is the countercurrent nature that defines pressure-driven channeling. A valley's airflow can be explained by a blend of these four effects in combination with the overlying synoptic and mesoscale conditions. Further, the dominant mechanism is subject to vary seasonally (Carrera et al. 2009).

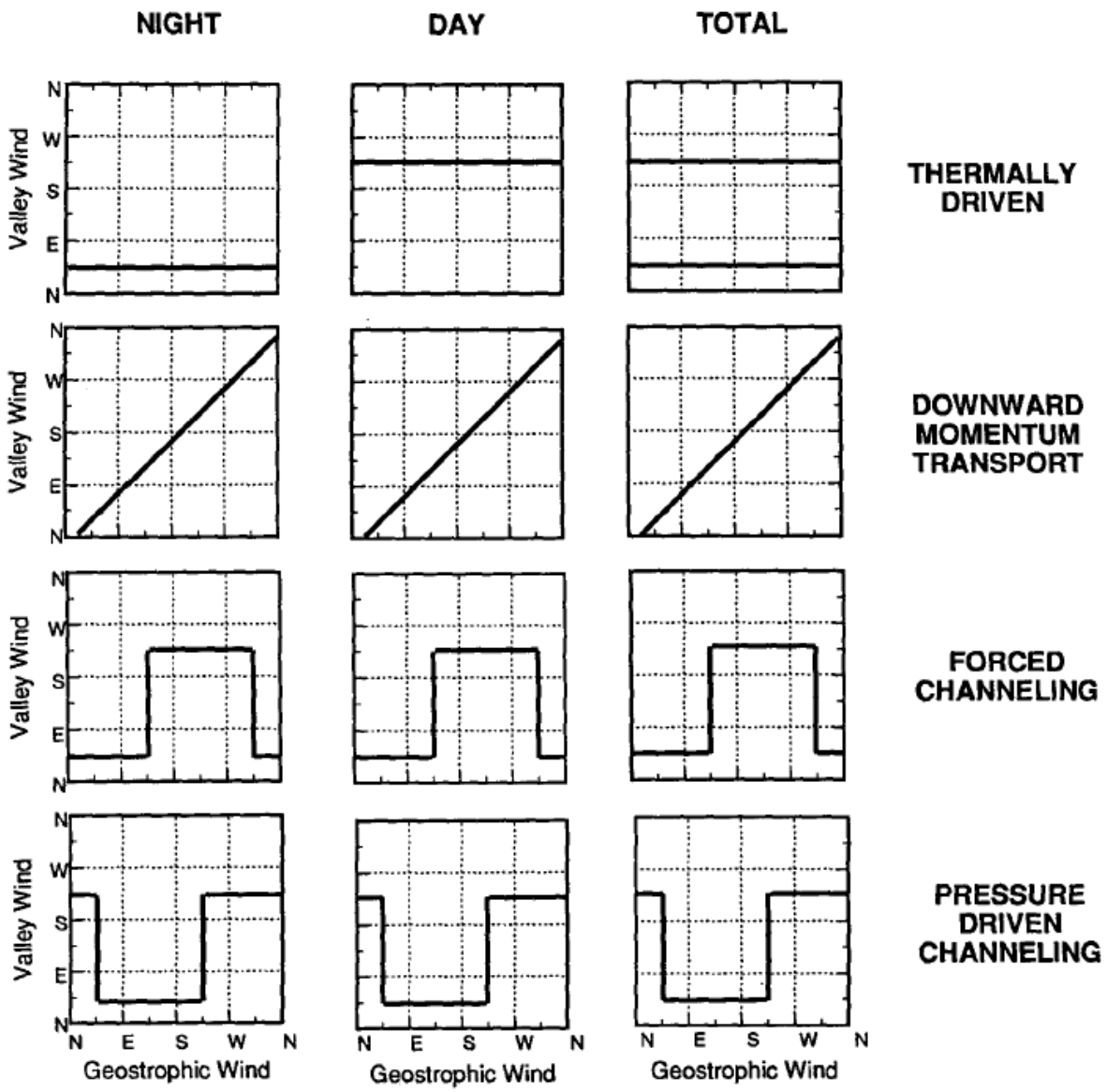

Fig. 8. Wind direction for both the aloft geostrophic and low-level valley flow for a NE to SW valley orientation as described by four mechanisms: thermal forcing, downward transport of momentum, forced channeling, and pressure driven channeling. Reproduced from Whiteman and Doran (1993).

Resolution of wind channeling behavior within models becomes crucial to producing a good forecast. This was well depicted by Roebber and Gyakum (2003) in their analysis of frontogenetical channeling that led to a prolonged freezing rain event in New York's St. Lawrence River Valley. That event involved cold air from a northerly high-pressure system pooling at the valley surface as a result of pressure driven channeling, while southerly winds aloft drove upper level warming. This resulted in two freezing rain events, each of which, when modeled without the effects of channeling, produced less simulated freezing rain volume (12.1% and 16.5%, respectively). The resulting $4 billion in damages stresses the importance of resolving wind channeling within models. Ensuring the resolution of channeling in numerical models will benefit an accurate forecast of small-scale wind behavior pertinent to sUAS flight.

4. METHODS

Weather conditions within CNY on 5 November 2017 are simulated herein. Simulations were executed using version 3.9.1.1 of the WRF model (Skamarock et al. 2008). WRF is a numerical weather model that can be used to simulate specific parameters that are poorly sampled by observations. This type of issue is relevant in areas of varying topography, as small-scale features are often generated around complex terrain. Visualizing the occurrence and evolution of these features is essential to understanding the low-level dynamic interactions of the atmosphere – where sUAS flights are conducted. Utilizing NWP as a tool to predict such weather hazards will provide a useful tool for UAS pilots. WRF can be used to simulate multiple domains, nesting each inner domain within a parent domain to achieve a higher resolution. The typical method for this involves reducing Δx by a factor of three for each nest (e.g., a 12 km parent domain with 4 km, 1.33 km, etc., nested domains). A higher resolution, or smaller grid spacing, resolves smaller scale

atmospheric features (e.g. X km grid spacing poorly resolves atmospheric features of 2X km large and well-resolves 10X km features). Thus, resolving weather features of interest relies on this, and resolving pertinent atmospheric wave features within a model encourages better results. In order to resolve waves small enough to impact sUAS, likely created by terrain, it is hypothesized that a resolution better than 4 km is needed. Being able to model the timing and intensity of terrain-induced waves is expected to be crucial to flight mission success.

Ambient weather conditions involved a synoptic scale low pressure system with warm frontal precipitation and southerly wind flow throughout the AP (Fig. 9). Higher temperatures and easterly wind flow are notable features of the CV when compared to the surrounding area. Cold frontal passage associated with the synoptic low pressure occurs outside of the simulation window. In the following subsections model details, use of surface observations, and handling of model output are discussed.

a. WRF Model Details

WRF contains a highly customizable physics suite that can be curated toward specific scenarios. Simulations for this experiment were initialized with North American Regional Reanalysis (NARR) 12 km data. These data were used to initialize the parent 12 km domain that included three, one-way nested domains of 4 km, 1.33 km, and 0.444 km Δx (Fig. 10). Each domain utilized 30 s (~0.926 km) United States Geological Survey (USGS) terrain resolution data. Aside from the Cumulus Parameterization (CP), parameterizations were consistent for each domain. Parameterizations, also referred to as a scheme, are the model physics that attempt to estimate impacts of atmospheric processes that cannot be resolved with the model grid spacing that is utilized (Rontu 2006). Thus, there is a larger dependence on parameterizations for coarse

resolutions. The discussion below details each parameterization and model characteristic used herein, each of which is summarized within Table 1.

Table 1: Summary of model domain characteristics and parameterizations.

	Nested	Δx (km)	Δy (km)	Δt (s)	Vertical Levels	MP	LSM	LW	SW	CP	PBL	Surface	topo_wind
Domain 1	No	12	12	36	50	WDM6	Unifed Noah LSM	RRTM	Dudhia	Kain-Fritsch	YSU	Revised MM5	Yes
Domain 2	Yes	4	4	12	50	WDM6	Unifed Noah LSM	RRTM	Dudhia	N/A	YSU	Revised MM6	Yes
Domain 3	Yes	1.33	1.33	4	50	WDM6	Unifed Noah LSM	RRTM	Dudhia	N/A	YSU	Revised MM7	Yes
Domain 4	Yes	0.444	0.444	1.33	50	WDM6	Unifed Noah LSM	RRTM	Dudhia	N/A	YSU	Revised MM8	Yes

For each simulation, the WRF Double-Moment Six-Class (WDM6) Microphysics (MP) scheme was used (Lim and Hong 2009). This is an extension of the WRF single-moment six class MP scheme, adding cloud condensation nuclei to the extensive list of hydrometeors (Pérez et al. 2014). While rainfall is not a concern of this experiment, the simulation day does involve warm frontal precipitation. In order to best replicate and produce fine scale wind patterns, accurate latent heating and cloud cover are needed.

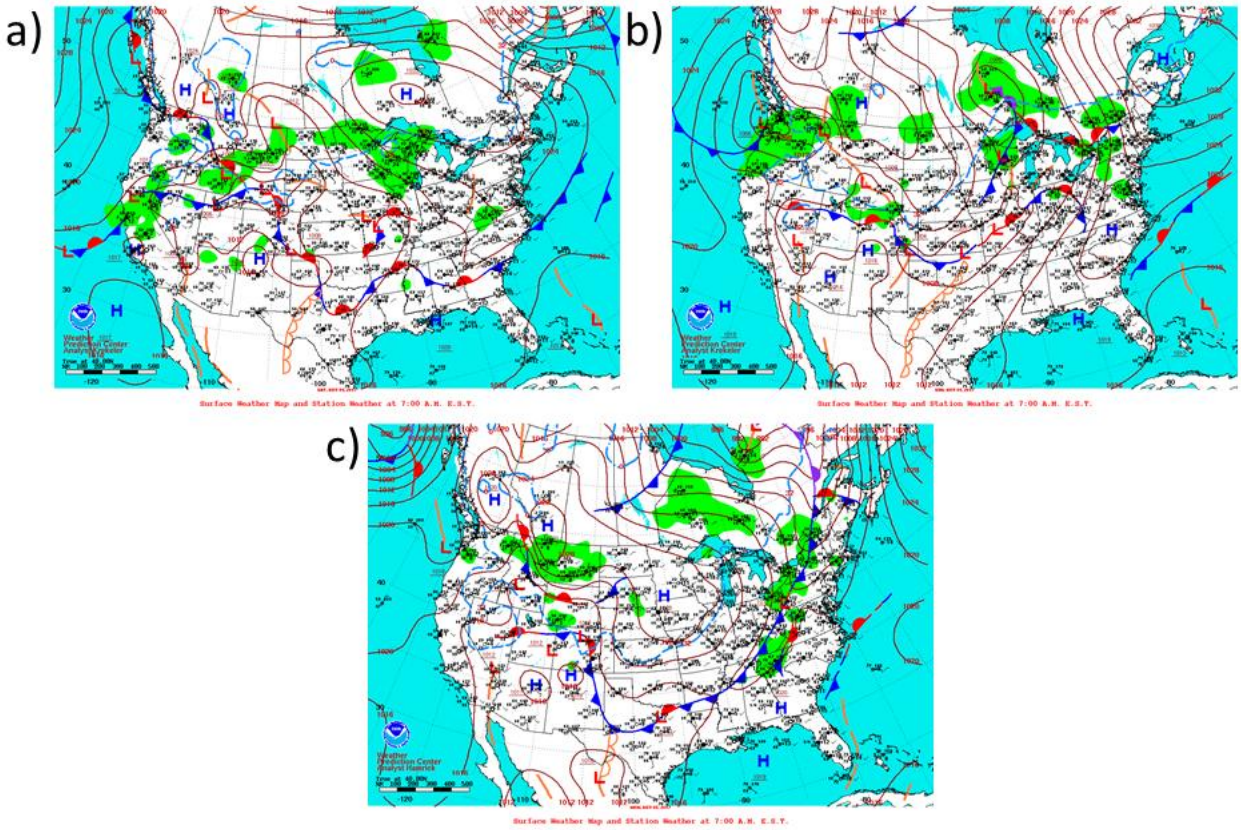

Fig. 9: Surface sea-level pressure and precipitation plots for 4 (a), 5 (b), and 6 (c) November 2017 at 7 AM EST. Images acquired from the Weather Prediction Center (WPC) surface analysis archive.

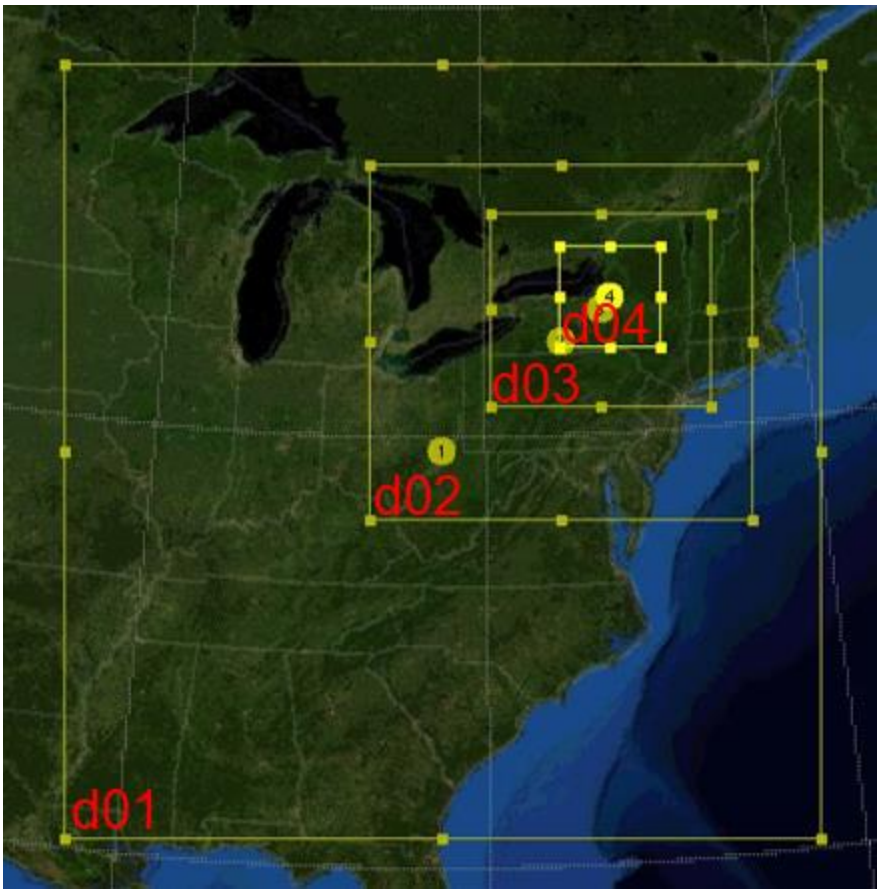

Fig. 10: The WRF nested domain structure utilized herein. The parent domain is represented by d01, with d02, d03, and d04 being the nested grids, respectively.

The Land Surface Model (LSM) used is the Unified Noah LSM (Tewari et al. 2004). This scheme has been shown to have an improved urban treatment compared to other LSMs, while taking surface emissivity into account as well (Skamarock et al. 2008). In addition, the Unified Noah LSM provides reasonable diurnal variations in fluxes (Pérez et al. 2014). An urban canopy representation is important for wind vector replication as well as its downstream evolution within and around the dense urban development of CNY.

The Longwave (LW) and Shortwave (SW) radiation schemes utilized consisted of the Rapid Radiative Transfer Model (RRTM) and Dudhia schemes respectively (Mlawer et al. 1997; Dudhia 1988). The use of the Dudhia SW scheme allows for implementing the "slope_rad" and "topo_shading" physics options. While not used in this experiment, their availability provides the opportunity for future work that could improve wind replication through better resolution of the diurnal heating cycle within complex terrain. The RRTM LW scheme is commonly paired with the Dudhia SW.

The CP of choice is the Kain–Fritsch scheme, which was only employed on the outermost 12 km domain (Kain 2004). CPs are commonly utilized for a coarse Δx of 10 km or greater, allowing it to be absent in the model's nests (Skamarock et al. 2008).

The dynamics of the PBL are typically parameterized along with a surface scheme to aid in estimation of vertical fluxes such as heat, momentum, and moisture (Pérez et al. 2014). Surface layer schemes estimate surface fluxes and stresses that in turn influence development of the PBL. The PBL scheme used was the Yonsei University Scheme (YSU) (Hong et al. 2006). The YSU has been shown to produce a dry, deeper boundary layer that quickly relieves capping inversions (Weisman et al. 2008). The Revised MM5 Scheme, based on the Monin-Obukhov similarity theory (Monin and Obukhov 1954), is recommended for use with the YSU, and thus, it was employed to parameterize the surface layer (Jiménez et al. 2011).

PBL schemes are essential in estimating both surface winds and mixing accurately throughout the PBL. WRF tends to produce negative wind speed biases around mountain- and hill-tops, and positive wind speed biases in plains and valleys (Jiménez and Dudhia 2012). As a result of this, WRF-produced wind speeds could be misleading. Along with the previous discussion, it can be hypothesized that decreasing Δx, thus, increasing terrain resolution, should tend towards

correcting this wind speed bias. Yet, the opposite can be proposed: higher resolutions complicate both terrain and wind patterns beyond model capabilities. This could lead to early chaotic divergence in a simulation if the synoptic flow is not governing small-scale motion. Considering the complexity of CNY's terrain, it is important to note that areas of steep terrain create a larger wind bias (Jiménez and Dudhia 2012). These findings have led to the "topo_wind" parameterization when using the YSU PBL scheme; this adjustment implements a sink term as a function of surface roughness, in accordance with terrain, within the momentum equation (Jiménez and Dudhia 2012). This adjustment was included within this experiments YSU simulated model domains.

Testing of the topo_wind parameterization has led to encouraging results. Model bias in flat terrain was shown to improve, while mountainous areas experienced an increase in bias when compared to a monthly average of observations (Lee et al. 2015). This mountainous bias is hypothesized to be as a result of representativeness error, sensor location, and crude orographic resolution. Representativeness error results in inaccurate model output that is typically a product of poorly replicated local terrain variation within a model simulation; further discussion on this error is included within the following sub-section. An important result of the Lee et al. (2015) study is the improvement in surface latent heat flux. Resolution of heat flux in a valley is crucial to the valley wind diurnal cycle, as discussed in Chapter 3.

Momentum flux is crucial in resolving accurate wind speeds and ensuring safe sUAS flight. Thus, the PBL parameterization is critical to estimating the presence of hazardous winds. This importance diminishes in coarse resolutions, as a 4 km Δx would generalize a great distance of sUAS travel. Generalization may lead to wind errors that in turn result in pilots conducting an unsafe flight. Considering this determinant of parameterizations in combination with topographic

detail, resolution of model output can significantly degrade the quality of a forecast. A decrease in Δx resolves more detailed terrain which leads to improvement in model performance (Rontu 2006). As air flows over model-resolved terrain, small-scale terrain variations that encourage atmospheric wave development may not be resolved. Thus, even a 0.444 km Δx will inevitably contain wind vector errors. Relatively small atmospheric features, typical of the micro- and meso-gamma scales, are usually heavily influenced by the prevailing synoptic and mesoscale patterns that govern a general forecast. Given sUAS sensitivity to winds, a general sUAS-centric forecast will differ and must be evaluated. Synoptic scale operational models are typically simulated with a $\Delta x \geq 12$ km, which is suitable for resolving large-scale pressure systems that influence local weather patterns. In this case, the smoothing of surface topography is not much of a concern. Synoptic models are used as operational forecasting guidance, producing reliable weather patterns to enable accurate, human-produced forecasts. This same concept should be applied not only to higher resolutions but to the blending of operational model forecasts. For example, a 4 km resolution may capture the presence of a meso-scale low pressure system well, while a 1 km output best exemplifies the local change in wind vectors. Such analysis could aid in the human identification of wind hazards and, thus, a reliable sUAS-centric forecast. Improving this forecast would then rely on proper model output that is dependent upon PBL parameterization performance and Δx replication of terrain.

The behavior of parameterizations when approaching small Δx values can become problematic. While most parameterizations have been tested in many situations/simulations, approaching higher resolutions may involve a change in parameterization performance. PBL schemes are considered satisfactory up to 500 m, where the sub-grid scale processes do not replicate model physics resolved processes. This duplication starts to become an issue around 100 m, where model dynamics can appropriately replicate boundary layer mass flux. These smaller Δx

intervals enter a "gray zone" where model parameterizations and physics resolve the same eddy behavior (Hong and Dudhia 2012). This gray zone is best known in modeling through CP, where it is incorporated for a Δx greater than 10 km and disregarded when Δx is less than 4 km. This 6 km gray area is comparable to the hundreds of meters in Δx that is expected to define the gray area of PBL parameterizations.

The gray zone is complicated by how turbulent eddies are handled in PBL schemes. Eddy cascade involves large momentum circulations dissipating into the smallest of eddies that then become irreversibly dampened by viscosity and converted into thermal energy. Large eddies can be driven by both wind shear and stability. Free convection within the PBL involves the buoyant, or thermal, mixing of air while forced convection mixes mechanically by wind shear. Mixing transfers several thermodynamic and kinematic variables (e.g. heat, moisture, and momentum) between different levels of the atmosphere. Buoyant mixing relies upon the surface heat flux that is positive during the daytime when heating typically occurs within the surface layer – the section of the PBL that is most effected by friction. Thus, heat is exchanged between the surface layer and a vertically adjacent layer of air. This process can be labeled as local mixing, which in turn drives the thermal properties of larger eddies, or non-local mixing (Shin and Hong 2013). In other words, the exchange between the surface layer and the lowest level of the ML is essential in developing mixing throughout the entire PBL. As a result of differing magnitudes, PBL schemes treat local and nonlocal mixing separately and, thus, their gray areas are associated with different Δx intervals (Shin and Hong 2013). Consideration of this issue is relevant for other parameterizations as well. A flexible, scale-aware parameterization would allow higher resolution simulations to be less impacted by the gray area. Specifically, when approaching a $\Delta x \leq 400$ m, parameterization of non-local mixing would be turned off while the local mixing could still be parameterized. Scale-aware

parameterizations are still being tested and developed, and they should be considered for future high-resolution simulation studies.

An increase in horizontal resolution should be paired with an increase in vertical resolution. The vertical grid should enable resolution of features that are resolved horizontally. A couple issues with this are discussed by Warner (2011). Many higher resolution simulations fail to satisfy the criteria for vertical resolution, as an increase in vertical levels creates the need for more computational power. For a Δx less than 1 km, hundreds, potentially thousands, of vertical layers are needed to fully resolve wave features in the vertical. A satisfactory number of vertical layers depends upon the slope of the resolvable feature: a smaller feature requires more layers. In a nested simulation, it is commonplace to keep the amount of vertical levels consistent in each domain. This combination of factors results in a challenge with respect to both computational time and space. More vertical layers, in combination with a smaller Δx, leads to large output files that take longer to produce. Yet, failing to provide enough vertical resolution can lead to spurious gravity wave generation, destabilizing and terminating model execution. Modelers tend to compromise and focus on Δx while increasing the number of vertical levels dependent on the nature of the experiment. Provided that this experiment relies on resolving features around topography, 50 vertical layers were used. This value is low for the aforementioned reasons. However, a computationally cost-effective model is desirable. Thus, the use of fewer vertical levels could be viewed as efficient if output is satisfactory. Furthermore, use of σ levels in WRF, which are terrain following vertical levels, encourages high resolution of the atmosphere's lower levels. Compacting vertical levels near the surface is valuable in PBL-centric simulations and is employed for this experiment (Fig. 11).

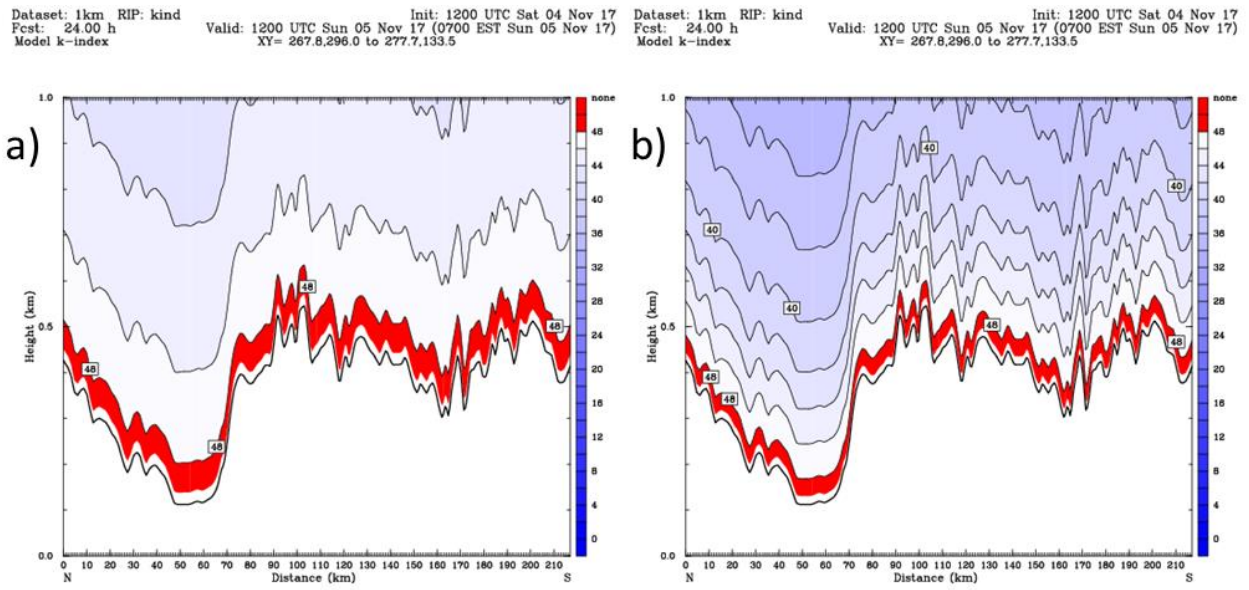

Fig. 11: Illustration of the default (a) and manually compacted (b) vertical σ levels within the WRF model up to 1 km MSL. The red contour signifies the lowest model layer while increasingly blue contours show higher levels of the atmosphere.

Model time step, Δt, indicates how often calculations involving neighboring model grid points are performed. The calculation load increases with decreasing Δx, which must be considered for computational stability. Model stability is usually discussed in terms of the Courant Number, μ, which is expressed as a negative linear relationship between Δx and Δt. Commonly, the $\mu = \frac{c\Delta t}{\Delta x}$ relationship where Δt = 6Δx enables maintenance of model stability; this, at first, resulted in a model Δt of 72 s herein. The nested grids, as with Δx, generally follow a 3:1 Δt ratio, resulting in a Δt of 24 s, 8 s, and 2.6 s for the second, third, and fourth nests, respectively. However, with use of condensed σ levels within the PBL, stability became an issue. Stability with respect to the vertical can also be expressed using the Courant Number, where Δz replaces Δx. The typical

solutions for increasing stability, in this case, involve increasing Δz, decreasing Δt, or a combination of the two. In order to maintain a high vertical resolution of the PBL, Δt was decreased to half of its original value. This 36 s Δt of the parent domain resulted in a 12 s, 4 s, and 1.33 s Δt for the respective nests. Thus, to maintain high resolution and stability, computational cost was effectively doubled. The University Corporation for Atmospheric Research (UCAR) and National Center for Atmospheric Research (NCAR) made this possible through the Cheyenne supercomputer provided by the Computational and Information Systems Lab (CISL). Cheyenne is a 5.34 petaflops computing system that provides users with high-performance processing power. Use of Cheyenne will be further discussed in the results and discussion chapters, as it is important to the production of high-resolution model output.

Another possible parameterization is a gust parameterization. With an optimization of local and non-local parameterizations in combination with high horizontal and vertical resolutions, resolving wind gusts can still be an issue. Wind gusts, as previously defined, coincide with brief fluctuations in pressure and force that impact aviation operations (Harris and Kahl 2017). As shown by Harris and Kahl (2017), utilizing a gust factor, which is used to measure the average intensity of a wind gust in a specific area, can help to forecast peak wind gusts. Measuring this gust factor relies heavily on temporal resolution; observations for a specific time of day or year will vary with the prevailing ambient conditions, and, thus, impact the resultant gust factor. Specifically, wind speed, diurnal heating, and wind direction were shown to impact a gust factor's magnitude.

- Wind speed exhibited an inverse relationship with gust factor
- Diurnal heating relates to wind speed as an afternoon increase in wind speed can result from the local mixing process

- Wind direction leads to the advection of air regimes that impact local stability

These are then further complicated by surface roughness, which in turn can influence local stability and result in the hyperlocal variation of gust factors. Current model parameterizations for wind gusts fail to consider this variation, which suggests an area for improvement.

A study by Gutiérrez and Fovell (2018) investigated the development of a gust parameterization while utilizing various PBL schemes and Δx intervals. Their findings suggest the importance of Bulk Richardson Number (R_B) and PBL structure, as substantial gusts are identified within neutral R_B and a shallow PBL. R_B is an estimation of airflow stability within a layer of air that derives from buoyancy and shear. Higher values of static stability can suppress mechanical shear and result in laminar air flow; unstable, turbulent air flows result from mechanical shear that is larger than the local buoyancy value; a R_B of zero is considered neutral. Further, R_B is better defined when more vertical model layers are resolved. This would suggest that as PBL resolution increases, wind gusts would become increasingly identifiable. Indeed, gust detection was shown to improve with increasing resolution – however, the false detection of wind gusts remains notably high. The suggested solution involves utilizing a 4 km Δx, which was shown to perform rather well, in an ensemble format of various gust parameterizations and PBL schemes to produce an accurate forecast. This conclusion is reached with knowledge of current computational cost limits, as producing an ensemble consisting of many 1 km Δx models is usually not temporally efficient for a forecast. Greater value is derived from several relatively coarse simulations as compared to a single high-resolution deterministic run. However, future computational capabilities will inevitably allow for these higher resolution ensembles. Therefore, developing an understanding of hyperlocal environments could result in detailed gust factor

mapping. Essentially, the value in understanding these environments and determining local gust factors will derive from collecting consistent hyperlocal measurements. With time, pockets of air that are safe for sUAS travel will be identified and collecting consistent, once improbable, measurements becomes possible. The result is a positive feedback for both NWP and the sUAS economy.

b. New York State Mesonet and Verification

A modeling experiment is best conducted with a set of verification measures. Verification is the practice of comparing model output to observations, thus evaluating model behavior (Warner 2011). Several common methods exist, and herein simulated winds are compared to surface observations and analysis data to assess model accuracy. Analysis data were acquired from various archives; their primary use was to inspect the synoptic pattern and expected airflow. Surface observation data within CNY is available through the NYSM, which provides detailed wind measurements on a five-minute temporal scale. The NYSM stations used is limited to 15 – each of which resides within the innermost domain (Fig. 12). These 15 stations, along with their respective station ID are: Belleville (BELL), Camden (CAMD), Cold Brook (COLD), Central Square (CSQR), Fayetteville (FAYE), Glenfield (GFLD), Harrisburg (HARR), Herkimer (HERK), Jordan (JORD), Morrisville (MORR), Osceola (OSCE), Redfield (REDF), Tully (TULL), Westmoreland (WEST), and Woodgate (WGAT). This set of station IDs is recorded in the Appendix, and each station is referred to by their respective ID acronym herein. Several factors must be considered when comparing specific observation stations values to model output.

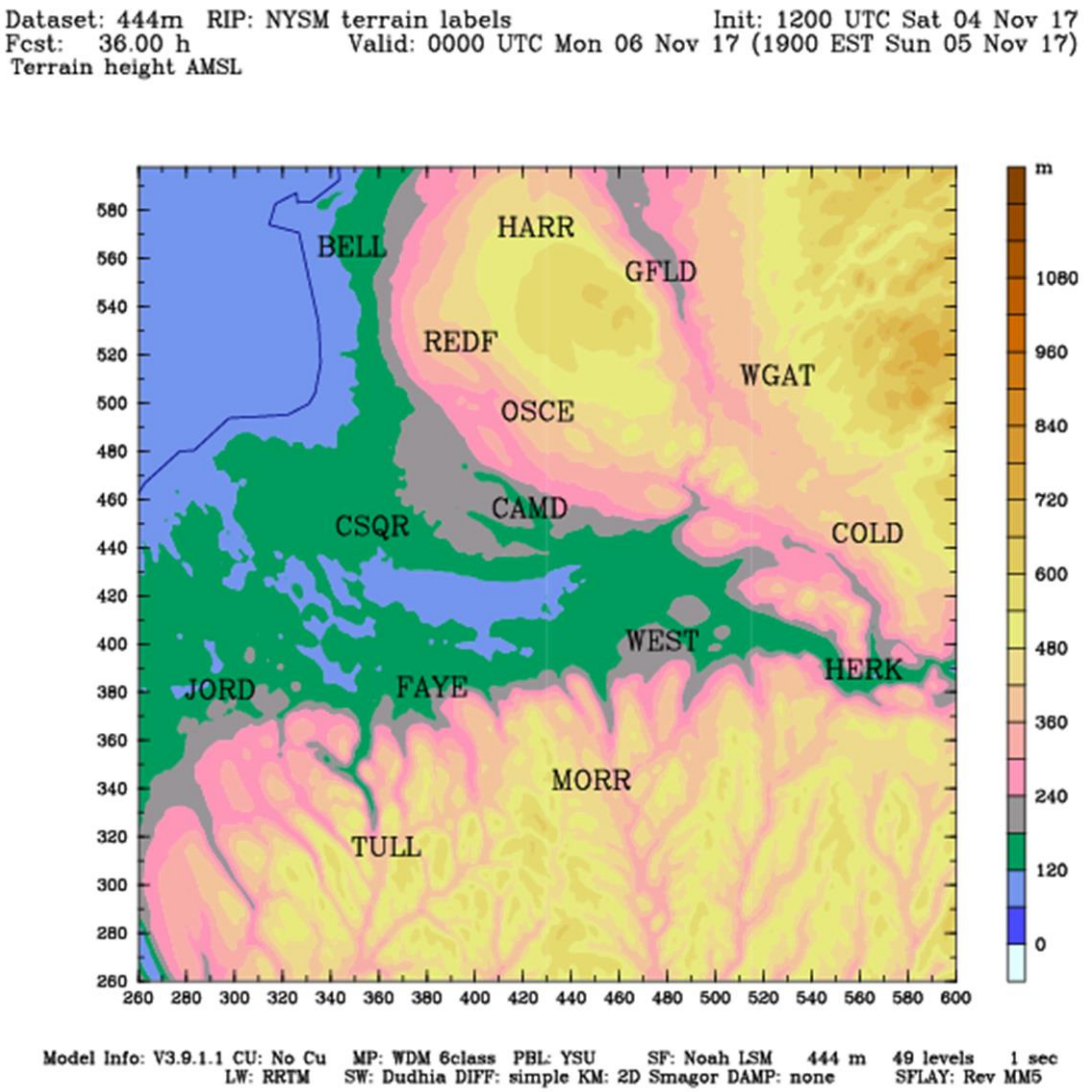

Fig. 12: MSL terrain of the CV with location labels for the NYSM stations.

Owing to the presence of complex topography, observations may not be representative of the simulated area as a result of orographic smoothing (Warner 2011). However, comparison with model output should ensure confidence in reproduction of wind-flow using a mesoscale model (Jiménez et al. 2010a). When comparing an observation to a value from a model location that does not correspond with a model grid point, the model value becomes a blend of the surrounding grid-

point calculations. Thus, this blend can poorly resolve local terrain and lead to an inaccurate representation of the sub grid-scale Reynolds-averaged surface conditions (Jiménez et al. 2010a). This inaccurate representation that arises from comparing observational data to the calculation blend produced from a model is referred to as representativeness error (Jiménez and Dudhia 2012). Representativeness error is essentially the misrepresentation of scales smaller than the one being observed. When comparing observational data from a station in a valley to a value estimated from a relatively coarse simulation, the smoothed topography in the model results in misrepresentation of the valley and, thus, error. Therefore, comparing non-grid-point model values to an averaged area of observations could remove some effects of representativeness error. However, if a blend of observations is unrealistic, selective grid-point comparison is recommended to mitigate misleading comparisons (Jimenez and Dudhia 2012).

WRF simulations are trending towards higher resolutions and larger domains (Steeneveld and Vilà-Guerau de Arellano 2019). Verifying fine-scale simulations will rely on dense networks of quality sensing data. Meteorological instruments require routine maintenance and have inherent thresholds and biases. When working with such observations, one must exercise care in order to assure that the data collected are reliable. Quality control and quality assurance, the examination of new and preexisting data respectively, are methods to ensure reliable data (Jiménez et al. 2010b). Both methods filter out erroneous readings that are likely to be the product of systematic and/or random error. Random error is essentially noise that results from the surrounding environment or instrument itself. Systematic error relies upon the use of an instrument, where miscalibration or mishandling of the instrument incur error. Filtered, quality wind measurements are necessary with the rising relevance of wind energy, dispersion of pollutants, and UA — to only name a few. Quality does not mean error free, but the smallest of improvements through routine maintenance

and quality control can ensure a dataset is: stored and managed correctly, within the environmental limits, and temporally consistent (Jiménez et al. 2010b). Inherently, this process can be made difficult if sensor stations are in a relatively hostile environment. For example, routine maintenance for a station within a mountainous region can be difficult, and its data could be less reliable as a result. This is an accepted issue that leads to observation investment elsewhere, leaving sensing gaps in these difficult to reach areas.

Sensing gaps have an adverse effect on modeling. It is difficult to forecast wind patterns on small scales given their dependence on local terrain, diurnal heating, and the overlying synoptic conditions (Rife et al. 2009). Wind vectors are sensitive to environmental changes, usually being one of the first parameters to fluctuate with the passing of atmospheric features. Essentially, winds are subject to high temporal and spatial variability. As with grid spacing, the spatial density of a sensing network corresponds to its spatial resolution of atmospheric features. Wind flow within sensing gaps will be disturbed as a result of topography, frontal boundaries, and storm systems (Wendell 1972). Thus, observing these disturbances relies upon an increased density in surface observations with a relatively high temporal resolution. Provided that sufficient mesoscale information can be derived from an accurate synoptic prediction (Roebber and Gyakum 2003), it is hypothesized that an accurate mesoscale prediction can provide sufficient microscale information. A Δx of about 1 km is thought to be enough to capture local wind variance in complex terrain, although replicating the spatial variability of wind patterns remains difficult (Rife et al. 2009; Mass et al. 2002). The lack of sensing data on the local scale is a barrier to verifying such features. Implementing a dense *in-situ* sensing network is expensive, and other methods for obtaining local data should be explored. A sUAS can obtain observational flight data within

sensing gaps and conduct maintenance on stations within hostile environments - providing a solution to both issues discussed.

While not utilized here, replication of complex wind flow patterns using ensemble modeling is worthy of discussion. Both the spatial and temporal evolution of a wind field are commonly displaced when compared with observations. More variability can be generated in simulations where more circulations are present – an issue that is best addressed by an ensemble approach (Rife et al. 2004). It is now commonplace in the meteorological community to evaluate performance of multiple models. While a few models may replicate the same feature, its simulated location and timing could be different. Ensemble models can be used to generate probabilistic areal percentages, where increased confidence in a forecast results from several simulations producing similar temporal and spatial characteristics of a phenomenon (Mass et al. 2002). The likelihood of occurrence based on this approach can be thought of as a threat index. This is an important consideration when modeling in complex terrain; upstream complex terrain may induce significant mesoscale phenomena that impact PBL features (Mass et al. 2002). Furthermore, changing Δx alone may not improve simulation quality, and the inclusion of proper parameterizations and higher resolution terrain data suggest areas for improvement (Carvalho et al. 2012). Therefore, implementing a blend of multiple Δx and PBL parameterizations to create a wind hazard threat index could prove beneficial in enabling safe sUAS operations.

It is difficult to define an approach to verification of model output from multiple nested domains. Fine-scale terrain variation and high temporal variations associated with both diurnal and sub-diurnal heating complicate local circulations on such fine scales that models will remain imperfect (Rife et al. 2004). Model data can be spatially rich but temporally sparse owing to computational storage limitations. The opposite is typically true for surface observations that have

high temporal and relatively low spatial resolutions. The existence of these combined issues leads to difficulty justifying verification measures at the higher resolutions (Rife et al. 2004). Further, use of traditional verification metrics may mask the benefits of high resolution simulations and favor coarse resolutions (Mass et al. 2002; Warner 2011). For example, as discussed above, the occurrence of a phenomenon at the incorrect location or timestep should be expected at smaller scales. For this study, traditional verification of model output is therefore difficult to execute, as a resolution bias may arise. Output for each domain must be evaluated using the same means of observational comparison in order to accurately assess differences associated with resolution changes. Thus, comparing model output (from a blend of nearby grid points) to observations for each domain will best characterize the effect of changing Δx. This method of verification is done for both hourly and five-minute intervals. Therefore, while model output seems to agree with observations, this experiment is not a deterministic representation of CNY on 5 November 2017. The simulations are used to visualize changes in wind-flow with changing Δx; a successful simulation will rely on the onset of phenomena, regardless of location (Weisman et al. 1997).

c. Processing

Model output is visualized using Read Interpolate Plot (RIP) software (Stoelinga et al. 2018). The weather parameters investigated primarily pertain to wind vectors and their sensitivity. Temperature and airflow stability, characterized by R_B, alongside wind speed and direction provide the basis for model output analysis. Considering the complex local valley terrain, cross-section plots are commonly used (Fig. 13). Cross-sections reveal atmospheric stratification with respect to terrain characteristics while also illustrating vertical variations. This allows for critical analysis with respect to FAA Part 107 guidelines. Further, as previously discussed, vertical levels

were held constant through each domain; thus, the differences visualized between each domain's cross-sections are dependent upon Δx.

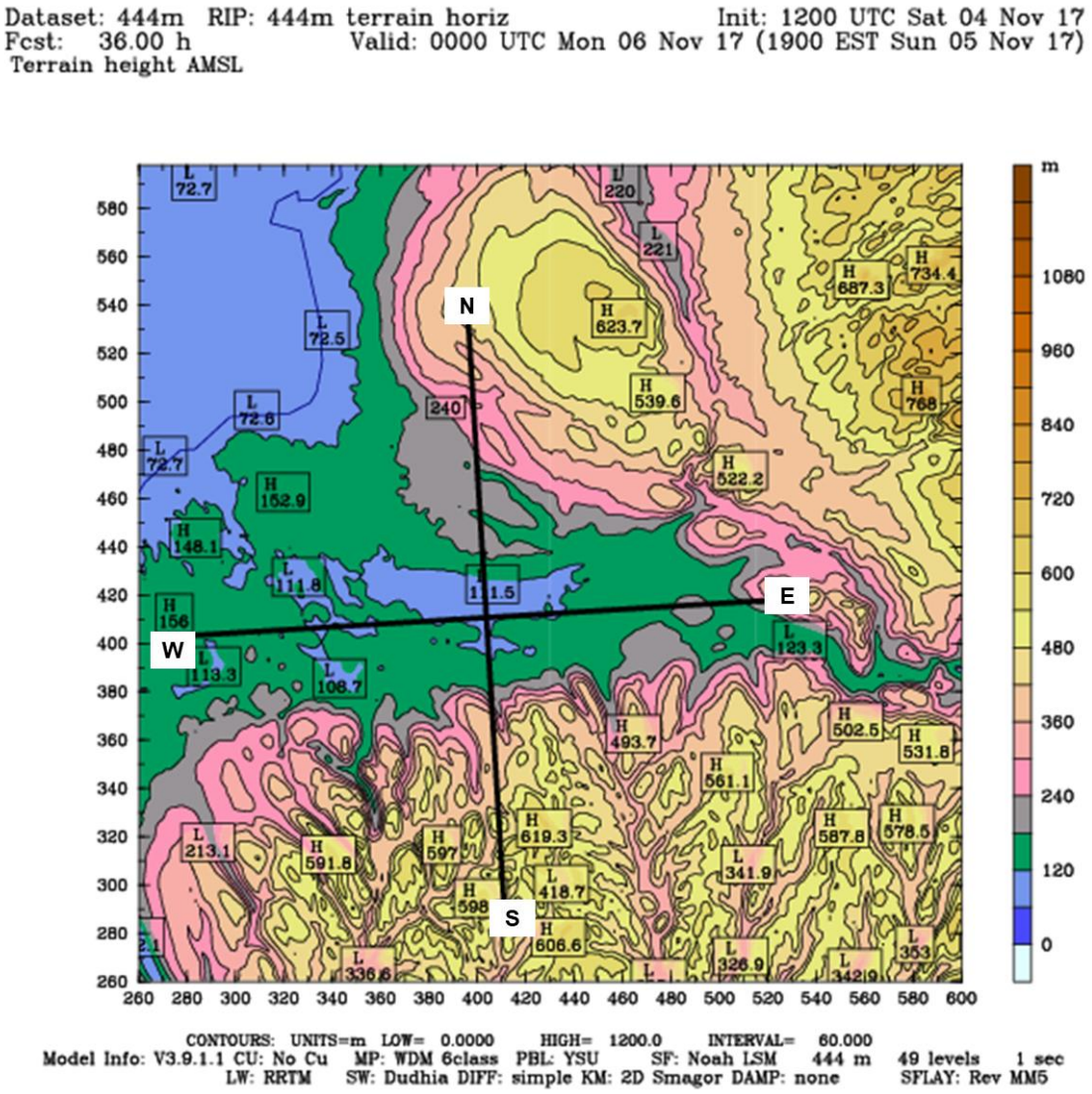

Fig. 13: MSL detailed terrain contours of the CV from the 0.444 km domain with lines indicating the east-west and north-south model cross-sectional coverage.

Plan-view plots of model output are also utilized. Given the difference in model domain nest sizes, a subdomain is used for comparison. Thus, the plan-view plots for each domain were

cropped to focus on the CV. The 0.444 km domain was cropped slightly to avoid analysis of noise near its lateral domain boundaries. Plan-view plots of model output are commonly visualized as a vertical layer average that embodies a PBL representation - one exception being model terrain, which was visualized using the lowest model level.

Multiple scripts were created to efficiently produce images. These scripts utilized the Python programming language to systematically execute RIP for each model nest. Separate scripts handled the generation of plan-view and cross-sectional plots. The RIP input files enable flexibility and customization that was not handled through scripting. However, a script was created to expedite the generation of multiple input files that each contained information necessary for subdomains and requested weather parameters. An outline of each script name, function, and use is provided in Table 2.

Time-series comparisons of model and NYSM 10 m wind data were generated using the Python programming language. The 10 m *u* and *v* wind components were extracted from model output and organized using RIP in the form of a time-series for each NYSM station's latitude and longitude. These data are used to calculate wind magnitude and direction. The NYSM data were organized in separate Microsoft Excel files that were combined and organized into a single spreadsheet. This enabled sorting of measurements of interest within station-respective arrays. The two sets of arrays are plotted with respect to time, both hourly and five-minute intervals, for each of the 15 NYSM locations. The full code-set is available upon request.

Table 2: Scripts created to execute and maintain organization of RIP output efficiently.

Name	Function	Use
Single_GIF	Produce one GIF for a given parameter and domain	Testing bounds and color scales of graphics
gifmaker	Create four GIFs, one for each domain, and name each accordingly	Creating four cross-section GIFs, one for each domain, of a given parameter
setup_subdom	Copy source input file templates to desired directory	Copying input files with subdomain coordinates for each domain to the present working directory
subdomains	Create four GIFs, one for each subdomain, and name each accordingly	Creating four horizontal contour plot GIFs, one for each domain, of a given parameter
RIP_Timestamp	Create several images at a model timestamp, both specified within the input file, and name them accordingly for each domain	Producing cross-section images of several variables at 13 UTC and 21 UTC for each domain
horiz_timestamps	Create several images at a model timestamp, both specified within the input file, and name them accordingly for each plan-view domain	Producing plan-view images of several variables at 13 UTC and 21 UTC for each domain
NYSM_skewT	Create several skew-T log-P diagrams at the specified input file timestamp and name them accordingly	Generating skew-T log-P profiles for each NYSM model latitude, longitude location at 13 UTC and 21 UTC

5. RESULTS

WRF was executed with Cheyenne supercomputing, and the simulation utilized 1440 processing cores to simulate 36 hours in 4 hours and 14 minutes of computational time. Simulations for coarse (resolution) domains with larger Δt completed quickly in comparison to the high resolution, small Δx nested domains. Subsequently, the file size for hourly 12 km domain output was the smallest at 4.51 GB. Each nested domain approximately doubled this value, resulting in a 0.444 km domain file size of 38.4 GB. Total file size of the five-minute model data (four, one-hour files for each domain) was 126 GB. The total size of all necessary RIP processing files generated from the hourly and five-minute output data totaled to ~40 GB and ~77 GB, respectively.

a. Verification

Comparison of model reflectivity to observations showed an overestimation of simulated morning warm frontal convective precipitation at 05 UTC. This was more apparent in the higher resolutions, which overestimated reflectivity values and discrete cell formation (not shown). Simulated precipitation through 11 UTC is displaced to the north while the intensity of afternoon showers is slightly underestimated by model output (not shown).

An example set of graphs depicting hourly NYSM observation and model output wind speed comparison is provided in Fig. 14. Error and standard deviation calculations for both the hourly and five-minute datasets are provided within Table 3 and Table 4, respectively. Wind speed comparisons show that at certain station locations (e.g. TULL and WGAT) the model has trouble replicating NYSM observations, while at other locations wind speeds appear to be well-resolved (e.g. CSQR and GFLD). Wind speed differences at TULL are as large as 8 m s^{-1}, while HERK

wind speed differences are ~1 m s^{-1} over much of the simulation window. Overall, when considering every station and resolution, model wind speeds have an average error of ±1.976 m s^{-1} for hourly data and ±1.935 m s^{-1} for five-minute data. Five-minute wind speed error graph examples are provided in Fig. 15. GFLD exhibits lower error for coarse resolutions while OSCE is best represented by the higher resolutions. Standard deviation calculations for the five-minute data show that higher resolutions capture more wind speed variability; the 0.444 km data are shown to overestimate variability (e.g. COLD) when compared to observations (Fig. 16).

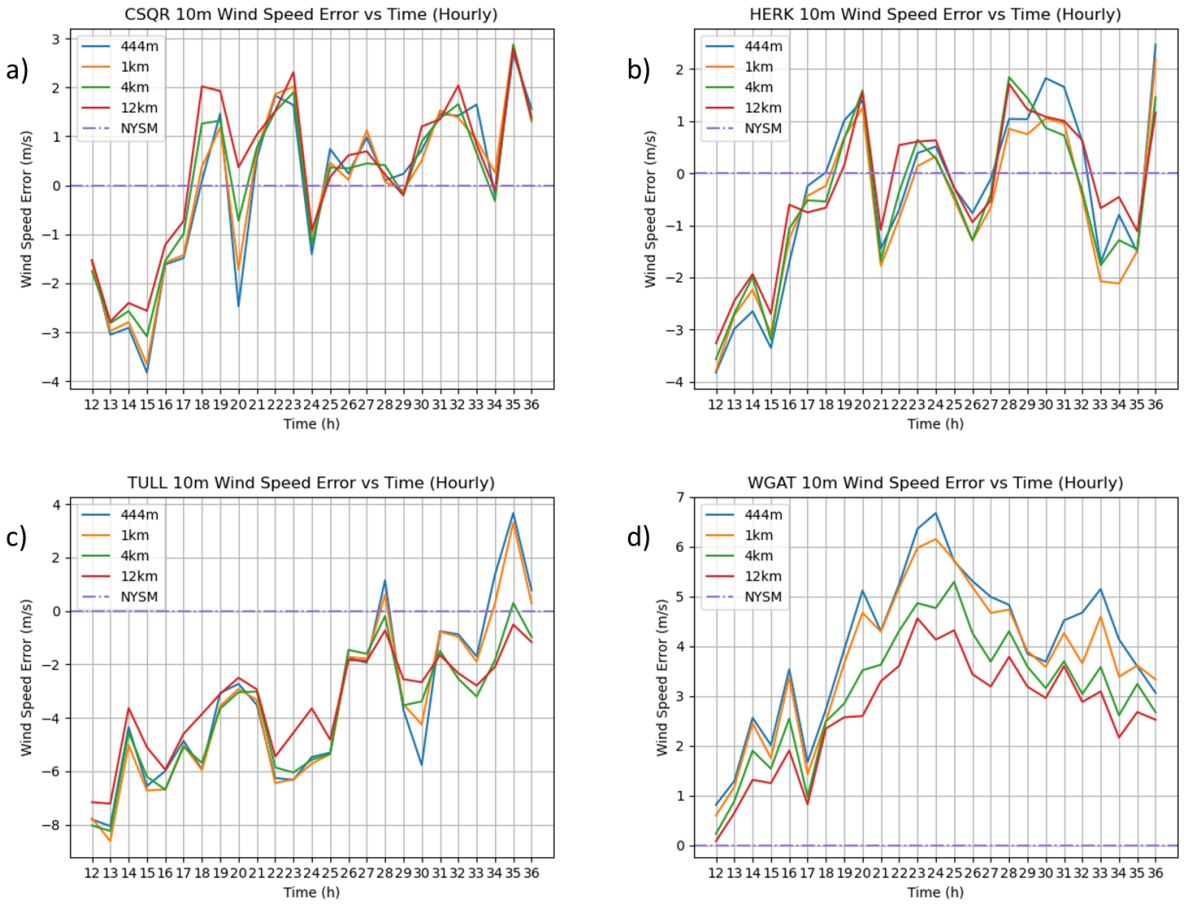

Fig. 14: Hourly 10 m wind speed comparison of NYSM station data with latitude-longitude model location output: a) CSQR, b) HERK, c) TULL, and d) WGAT. The x-axis represents the time (h) of the entire 24 h analysis window and the y-axis represents wind speed error (m s^{-1}). Different colored lines represent the NYSM observations and each model resolution's output: purple = NYSM, red = 12 km, green = 4 km, yellow =1.33 km, blue = 0.444 km. NYSM observations are represented as y=0; error within model output is depicted as a deviation from this line.

Table 3: Hourly NYSM station location wind data (m s^{-1}) for both observations and model output. Darker red shading indicates higher wind speed error; NYSM observation standard deviations and the model domain with the closest standard deviation are depicted by green cells.

	Hourly Wind Speed Data from 00 UTC 11/5 to 00 UTC 11/6									
	Errors					Standard Deviations				
Station	12km	4km	1km	444m	Station Average	Obs.	12km	4km	1km	444m	Station Average
BELL:	1.804	2.029	2.041	2.096	1.993	1.151	2.441	2.598	2.621	2.742	2.601
CAMD:	1.301	1.442	1.528	1.579	1.462	1.025	0.926	0.998	1.334	1.439	1.174
COLD:	1.400	1.622	1.783	2.152	1.739	0.735	1.156	1.258	1.322	1.434	1.293
CSQR:	1.318	1.293	1.343	1.436	1.347	1.524	0.933	0.843	0.927	0.943	0.912
FAYE:	1.511	1.702	2.059	2.297	1.892	1.555	1.306	1.450	1.385	1.496	1.409
GFLD:	1.200	1.228	1.394	1.552	1.343	1.266	1.553	1.897	2.119	2.310	1.970
HARR:	1.737	1.849	2.324	2.279	2.048	1.304	2.002	2.286	2.550	2.511	2.337
HERK:	1.108	1.281	1.326	1.360	1.269	1.185	1.027	1.167	1.145	1.190	1.132
JORD:	1.563	2.218	2.201	2.036	2.005	1.370	1.663	2.189	2.303	2.227	2.096
MORR:	1.751	1.890	2.079	2.339	2.015	1.064	1.769	1.902	1.898	1.839	1.852
OSCE:	2.013	1.565	1.409	1.316	1.576	0.740	0.911	0.957	0.892	0.891	0.913
REDF:	1.994	1.510	1.550	1.670	1.681	0.918	1.110	1.145	1.173	1.278	1.177
TULL:	3.386	3.899	3.948	3.983	3.804	1.378	1.253	1.619	2.063	2.140	1.769
WEST:	1.530	2.038	2.397	2.385	2.088	1.602	0.865	1.295	1.808	1.800	1.442
WGAT:	2.682	3.109	3.758	3.994	3.386	0.439	1.177	1.311	1.525	1.564	1.394
Average:	1.753	1.912	2.076	2.165	1.976	1.150	1.339	1.528	1.671	1.720	1.565

Table 4: Five-minute NYSM station location wind data (m s^{-1}) for both observations and model output. Darker red shading indicates higher wind speed error; NYSM observation standard deviations and the model domain with the closest standard deviation are depicted by green cells.

	5-Minute Wind Speed Data from 12, 13, 20, and 21 UTC									
	Errors					Standard Deviations				
Station	12km	4km	1km	444m	Station Average	Obs.	12km	4km	1km	444m	Station Average
BELL:	1.163	1.704	1.695	1.667	1.557	1.580	0.610	0.526	0.798	1.203	0.784
CAMD:	1.730	1.771	1.531	1.172	1.551	0.915	0.932	0.972	1.083	1.224	1.053
COLD:	1.164	1.241	1.424	1.689	1.380	0.721	0.599	0.932	1.257	1.410	1.050
CSQR:	0.793	0.809	0.883	0.978	0.866	1.637	0.942	0.960	1.063	1.143	1.027
FAYE:	1.643	2.286	3.037	2.908	2.468	1.015	0.669	0.559	0.455	0.585	0.567
GFLD:	0.849	0.959	1.121	1.326	1.064	1.700	0.834	1.092	1.255	1.412	1.148
HARR:	0.973	1.034	1.479	1.414	1.225	1.861	0.830	1.043	1.241	1.255	1.092
HERK:	0.941	1.250	1.396	1.190	1.194	1.639	0.945	1.223	1.356	1.393	1.229
JORD:	1.743	2.428	2.449	2.482	2.275	1.529	0.972	1.776	1.930	2.002	1.670
MORR:	0.910	1.139	1.593	2.339	1.495	0.780	0.541	0.628	0.751	0.916	0.709
OSCE:	2.162	1.606	1.389	1.352	1.627	0.779	0.864	0.987	0.994	1.042	0.972
REDF:	2.534	1.955	2.076	2.257	2.206	1.262	0.802	0.934	1.011	1.052	0.950
TULL:	3.089	3.550	2.958	2.883	3.120	1.357	0.416	0.505	0.922	1.053	0.724
WEST:	2.087	2.818	3.119	2.939	2.741	2.011	0.376	0.979	1.296	1.281	0.983
WGAT:	3.282	3.866	4.784	5.112	4.261	0.445	0.790	1.113	1.430	1.750	1.271
Average:	1.671	1.894	2.062	2.114	1.935	1.282	0.741	0.949	1.123	1.248	1.015

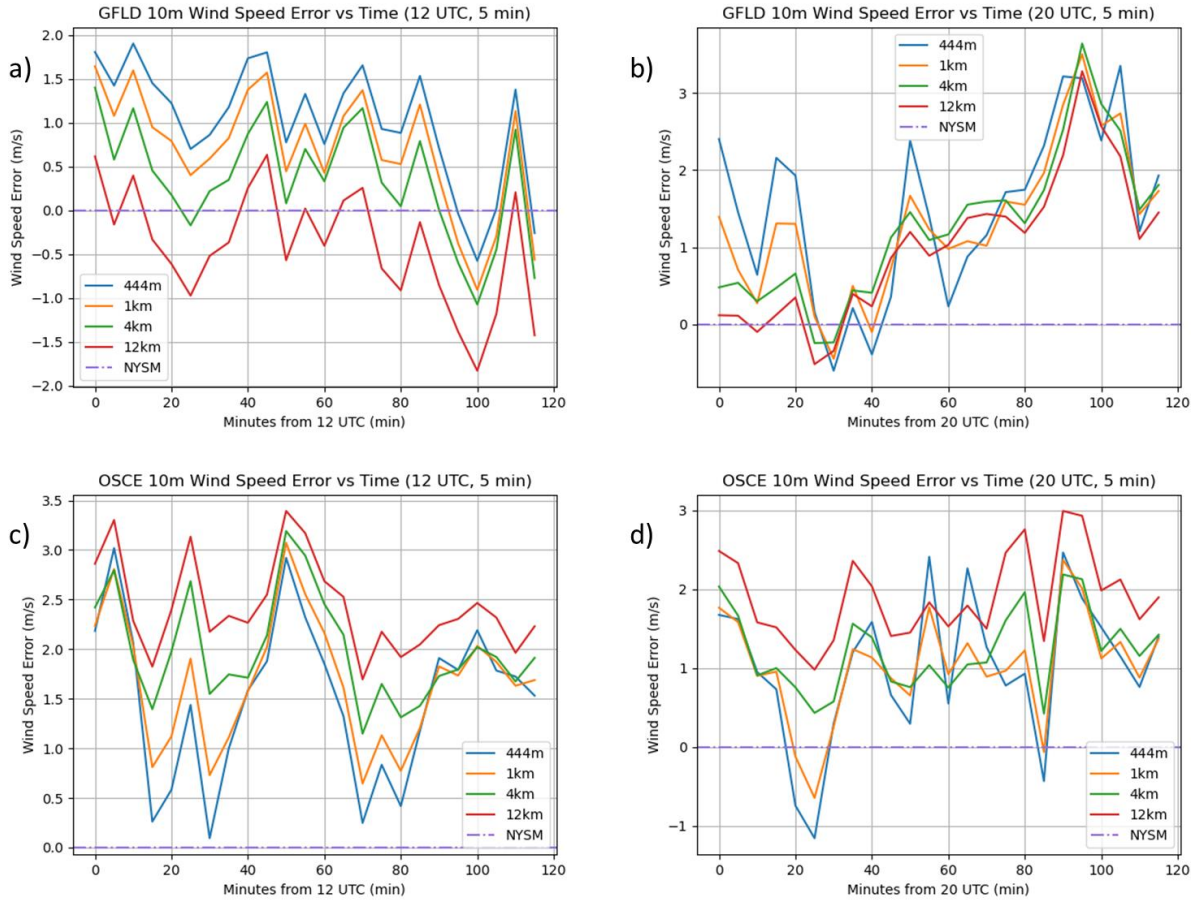

Fig. 15: As in Fig. 14, but showing five-minute 10 m wind speed (m s^{-1}) comparison of NYSM station data with latitude-longitude model location output: a) GFLD from 12-14 UTC, b) GFLD from 20-22 UTC, c) OSCE from 12-14 UTC, and d) OSCE from 20-22 UTC.

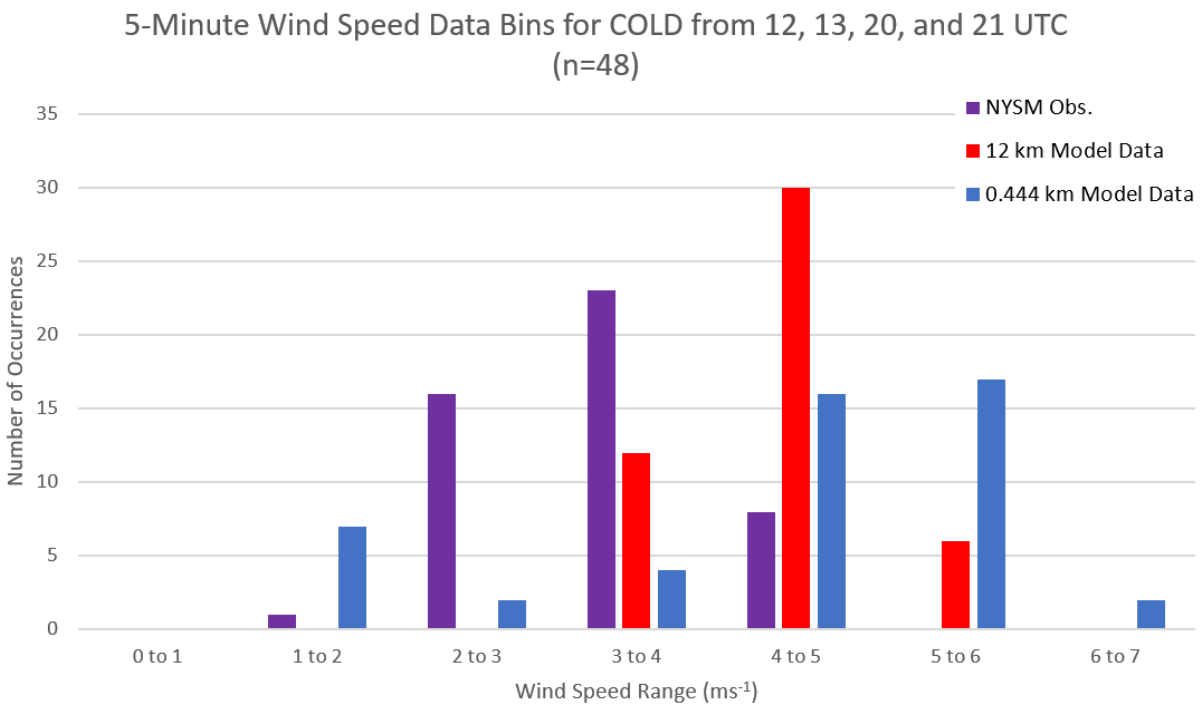

Fig. 16: Binned wind speed data of NYSM observations (purple), 12 km model output (red), and 0.444 km model output (blue) for COLD. The x-axis shows each 1 m s^{-1} range bin while the y-axis represents the number of occurrences each bin contains.

Example hourly wind direction comparison graphs are provided in Fig. 17. Both the NYSM observations and model output show easterly flow within the valley (e.g. WEST), south-easterly flow exiting the CV (e.g. CSQR), and southerly flow over the AP (e.g. TULL). At the FAYE and JORD locations the model struggles to replicate wind direction in the morning hours but performs better by the afternoon. The opposite occurs for WEST, which is the only location where simulation of afternoon wind direction is poor. Overall, the model produces accurate wind directions.

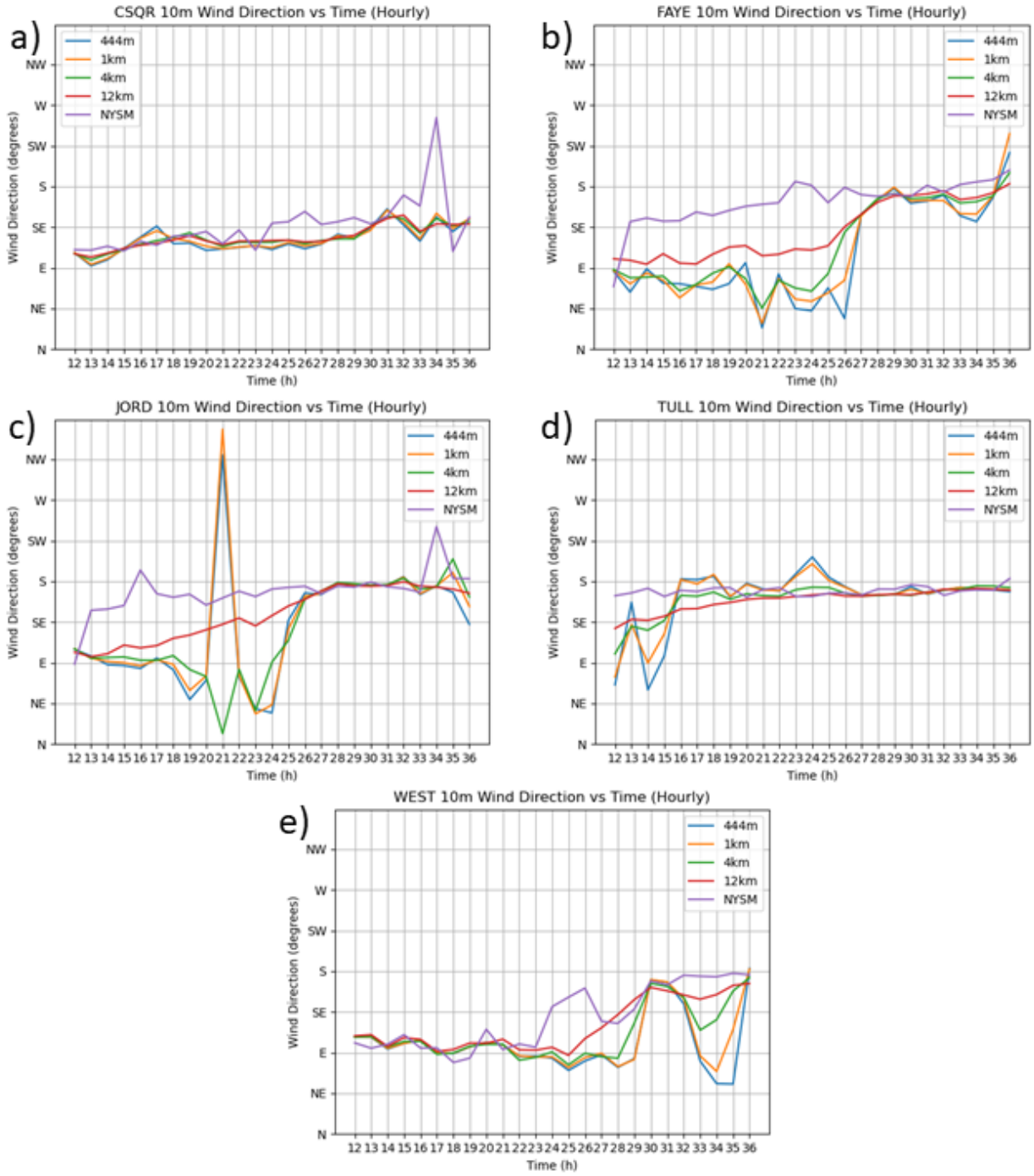

Fig. 17: Hourly 10 m wind direction (°) comparison of NYSM station data with latitude-longitude model location output: a) CSQR, b) FAYE, c) JORD, d) TULL, and e) WEST. The x-axis represents the time (h) of the entire 24 h analysis window and the y-axis represents wind direction (°) with the appropriate cardinal direction labels. Different colored lines represent the

NYSM observations and each model resolution's output: purple = NYSM, red = 12 km, green = 4 km, yellow =1.33 km, blue = 0.444 km.

b. Wind Speed

Simulated wind speeds vary with Δx. Fig. 18 & Fig. 19 display an average of the lowest model vertical levels to represent the environment sUAS would be flying in per Part 107. Results show that use of a smaller Δx results in resolution of pockets of both lower and higher wind speeds. The 1.33 km and 0.444 km Δx domains produce fine-scale wind speed fields while the 12 km and 4 km domains produce smooth fields within the subdomain at 13 UTC (Fig. 18). This feature associated with higher resolution continues into the afternoon, as the fine-scale output reveals pockets of air that may either benefit or be hazardous to sUAS operations (Fig. 19).

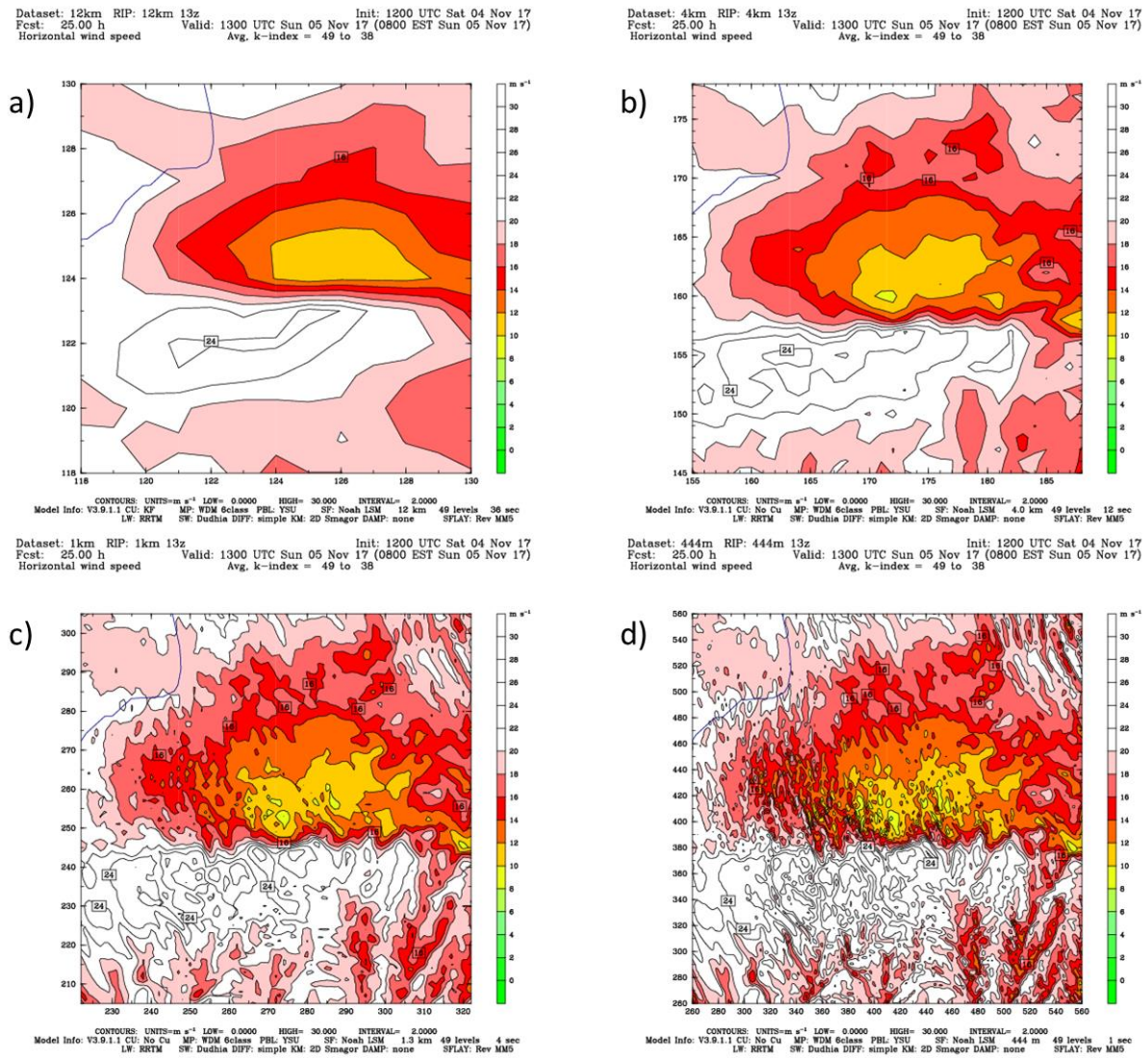

Fig. 18: Average low-level (surface up to model level 38: approximately 1600 ft MSL) wind speed in m s^{-1} within each subdomain at 13 UTC: a) 12 km, b) 4 km, c) 1.33 km, and d) 0.444 km. Color contoured scale represents wind speeds that would permit safe sUAS flight (green-yellow, 0-11 m s^{-1}) and also those that could be hazardous (orange-white, 12-30 m s^{-1}) based on Fig. 3.

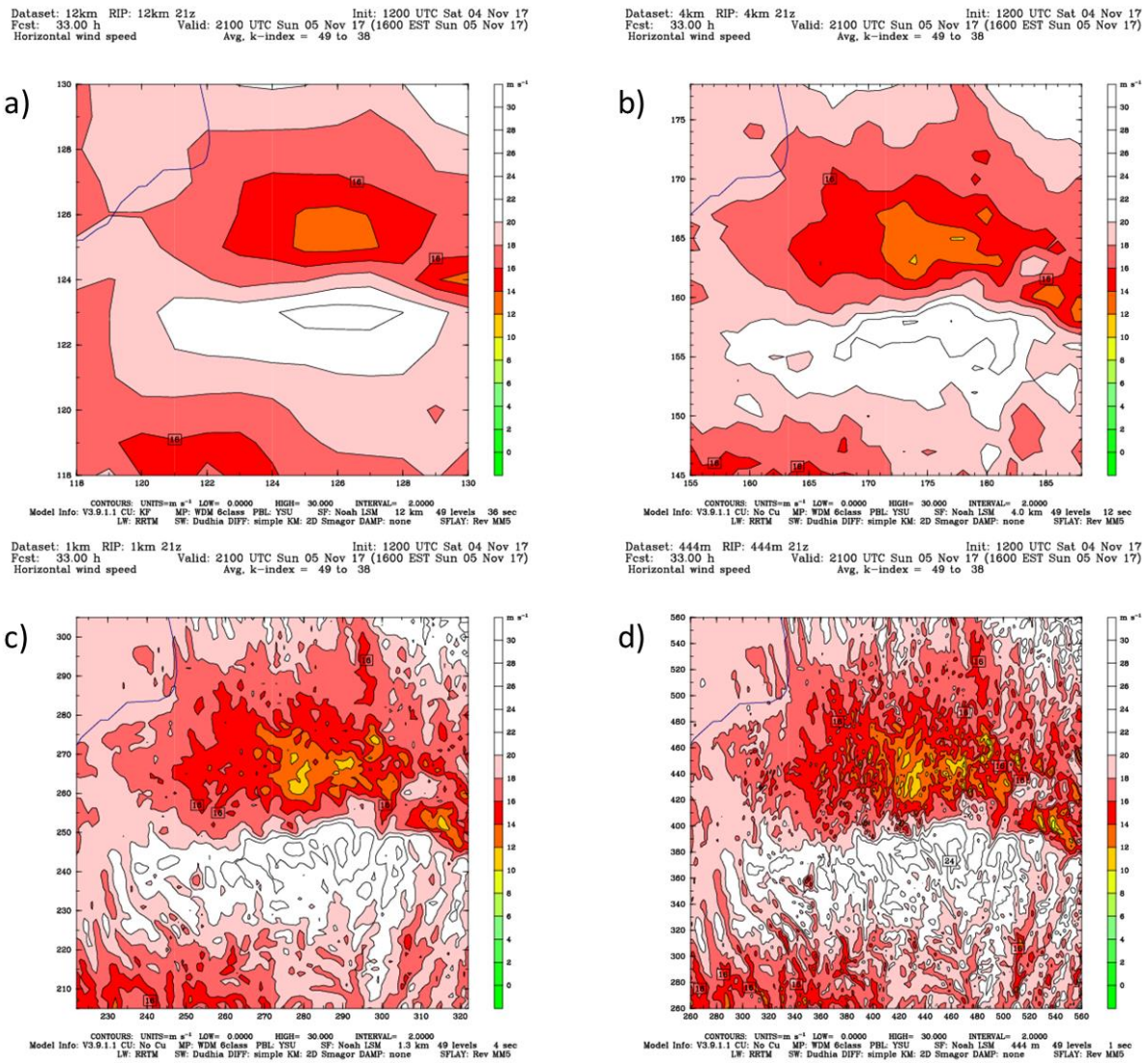

Fig. 19: As in Fig. 18, but at 21 UTC.

Cross-section plots display similar characteristics while revealing speed shear in the stratified atmosphere above the valley. The 13 UTC cross-section of wind speed is illustrated in Fig. 20. Each simulation indicates that the calmest pocket of air resides on the valley surface's windward side and that wind speed changes rapidly with height above the AP. A wind maximum of ~30 m s^{-1} just above the slope from the AP to CV is resolved and of equal magnitude in each

simulation. Its core resides between 0.8 km and 0.9 km MSL. The valley floor's wind speed becomes better resolved with a decrease in Δx. The 12 km domain fails to reproduce a pocket of wind speeds ≤ 8 m s^{-1} that is present on the leeward side of the CV in the three other domains. In addition, the resolution of wave activity with airflow out of the south is captured in the 1.33 km and 0.444 km Δx simulations. The 0.444 km Δx simulation provides more detail of this wave feature and minor wind speed discrepancies when compared with the 1.33 km Δx simulation.

Afternoon 21 UTC cross-sectional wind speeds are displayed in Fig. 21. Air above the AP maintains its relatively high shear while wind speeds above the valley show an increase in shear. The windward wind maximum has decreased in magnitude and elevation, prevailing at ~26 m s^{-1} between 0.5 km and 0.6 km MSL. Each simulation continues to capture wind speed minima on the valley surface and exhibit less overall variation between each other. In fact, the 13 UTC wind maximum on the leeward side of the CV becomes a notable minimum and is captured by each simulation at 21 UTC. The primary difference continues to be resolution of wave activity, as the 1.33 km and 0.444 km simulations resolve more vertical variations in wind speed than the 12 km and 4 km simulations. A low-frequency wave signature is present in the 4 km simulation; however, its amplitude is much smaller than in the higher resolution domains.

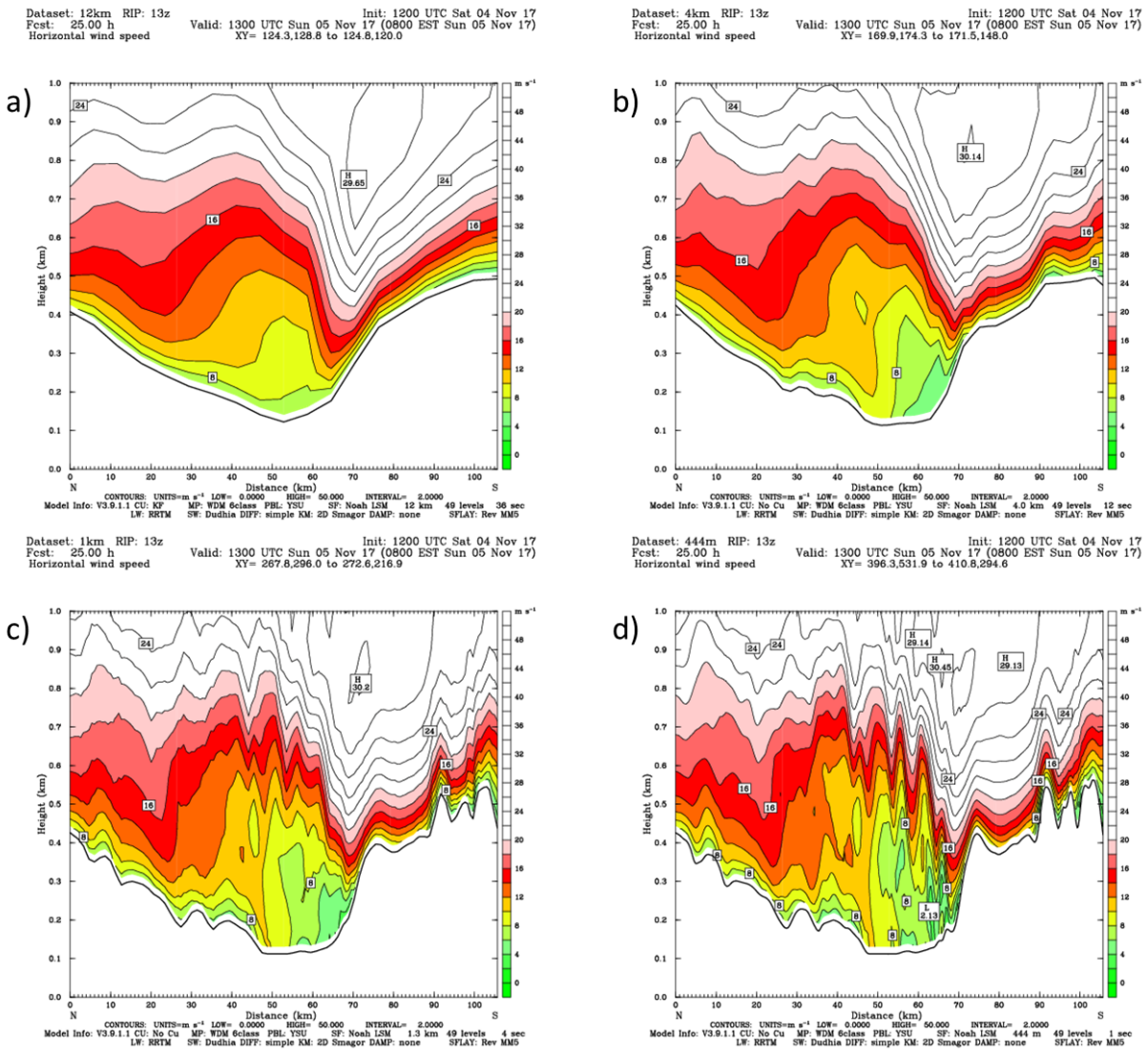

Fig. 20: North-south cross-section of wind speed in m s^{-1} at 13 UTC: a) 12 km, b) 4 km, c) 1.33 km, d) 0.444 km. Color contoured scale represents wind speeds that would permit safe sUAS flight (green-yellow, 0-11 m s^{-1}) and also those that would be hazardous (orange-white, 12-30 m s^{-1}) based on Fig. 3.

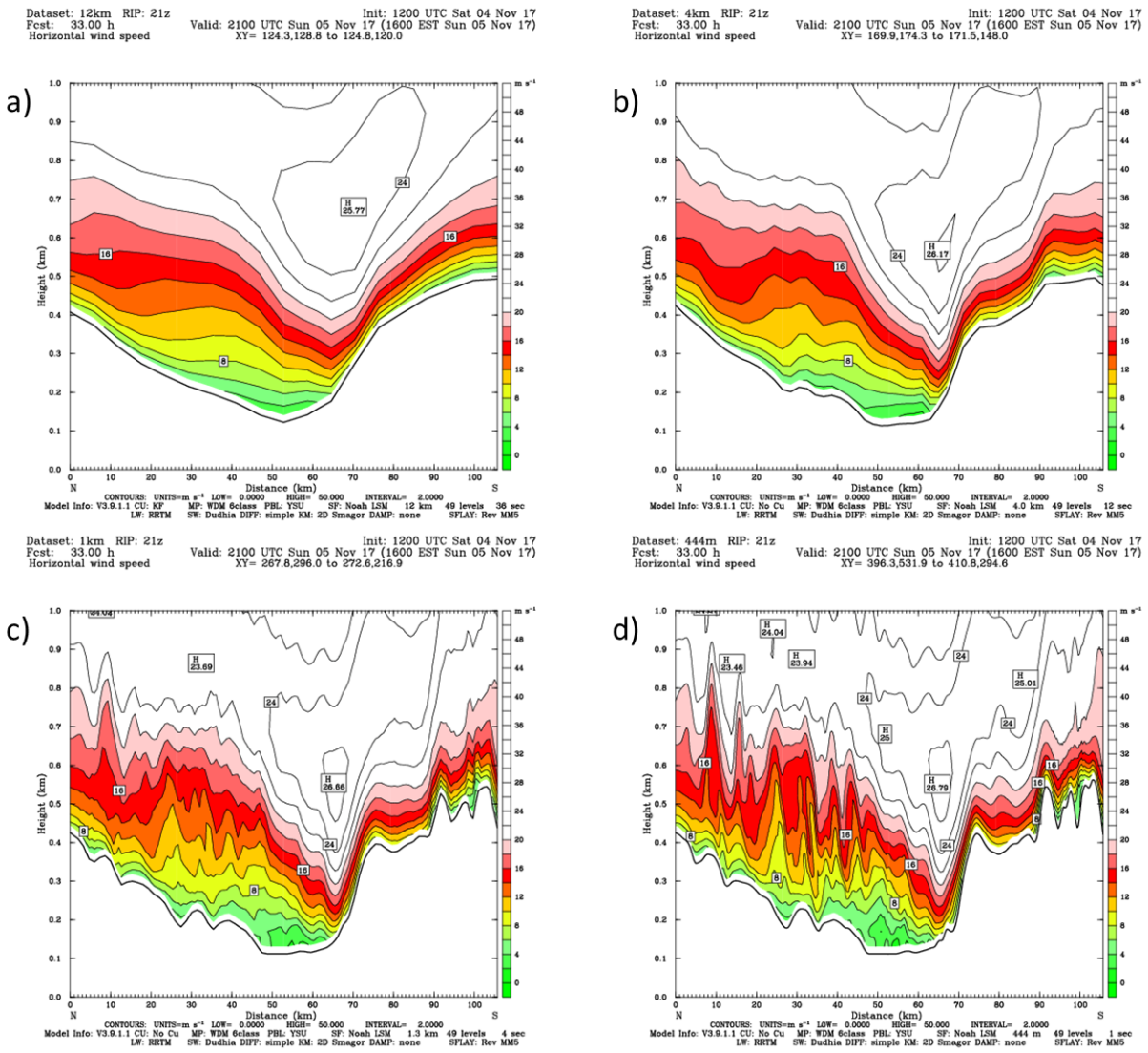

Fig. 21: As in Fig. 20, but at 21 UTC.

c. Wind Direction

Plan-view plots of low-level average wind direction convey the presence of a drainage flow. Southerly winds atop the AP are evident alongside easterly flow within the CV. The 12 km simulation poorly replicates this pattern at 13 UTC while the other simulations resolve this drainage behavior (Fig. 22). More detail in directional variation is a notable feature of the higher

resolutions. The same cannot be stated regarding the low-level vertical average of 21 UTC wind directions (Fig. 23). Southerly flow reigns over each subdomain with minor terrain-relative details becoming the only discrepancy between the different simulations.

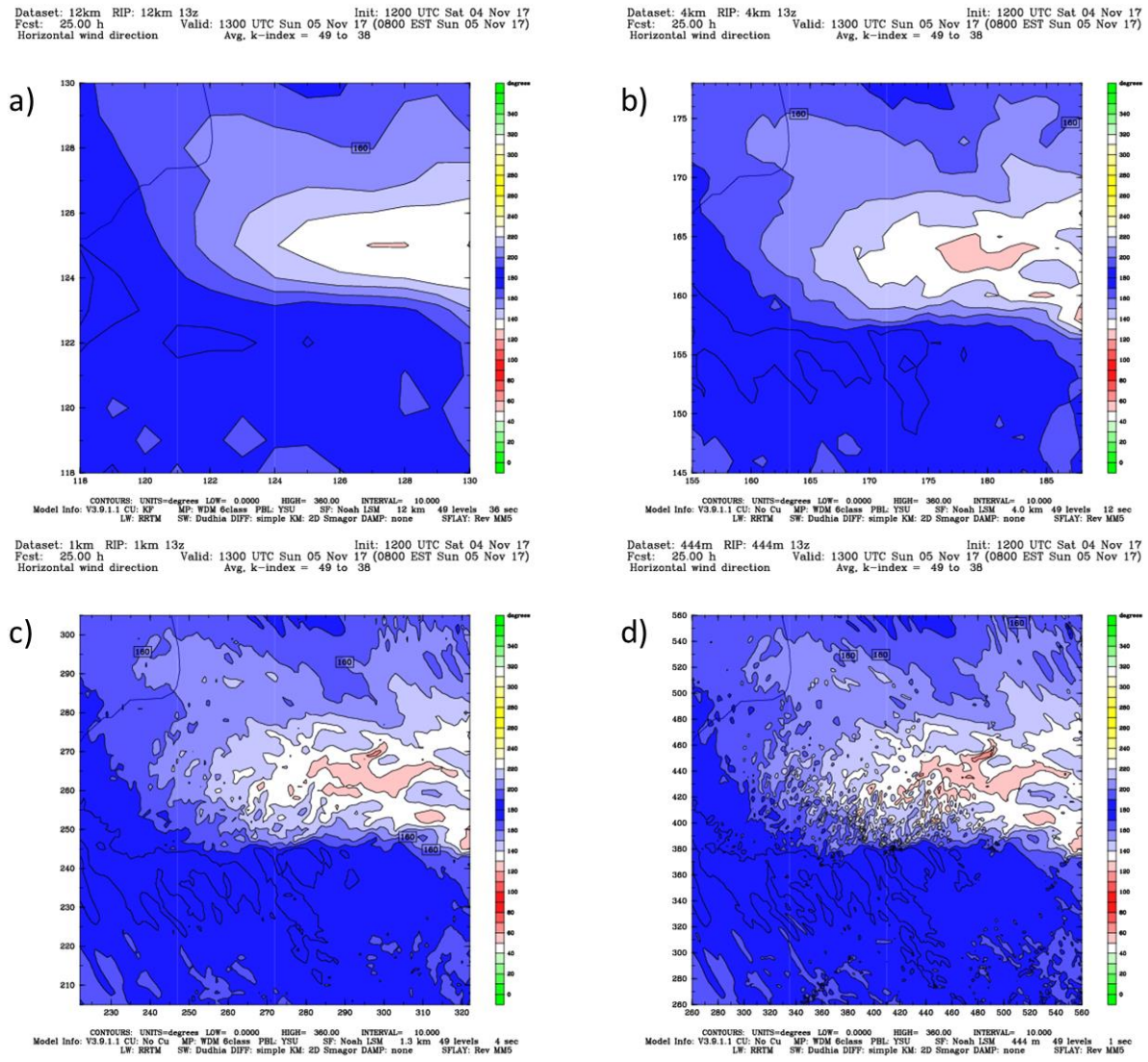

Fig. 22: Average low-level (surface up to model level 38: approximately 1600 ft MSL) wind direction (°) within each subdomain at 13 UTC: a) 12 km, b) 4 km, c) 1.33 km, d) 0.444 km. Blue contours indicate southerly wind flow and red contours indicate easterly wind flow.

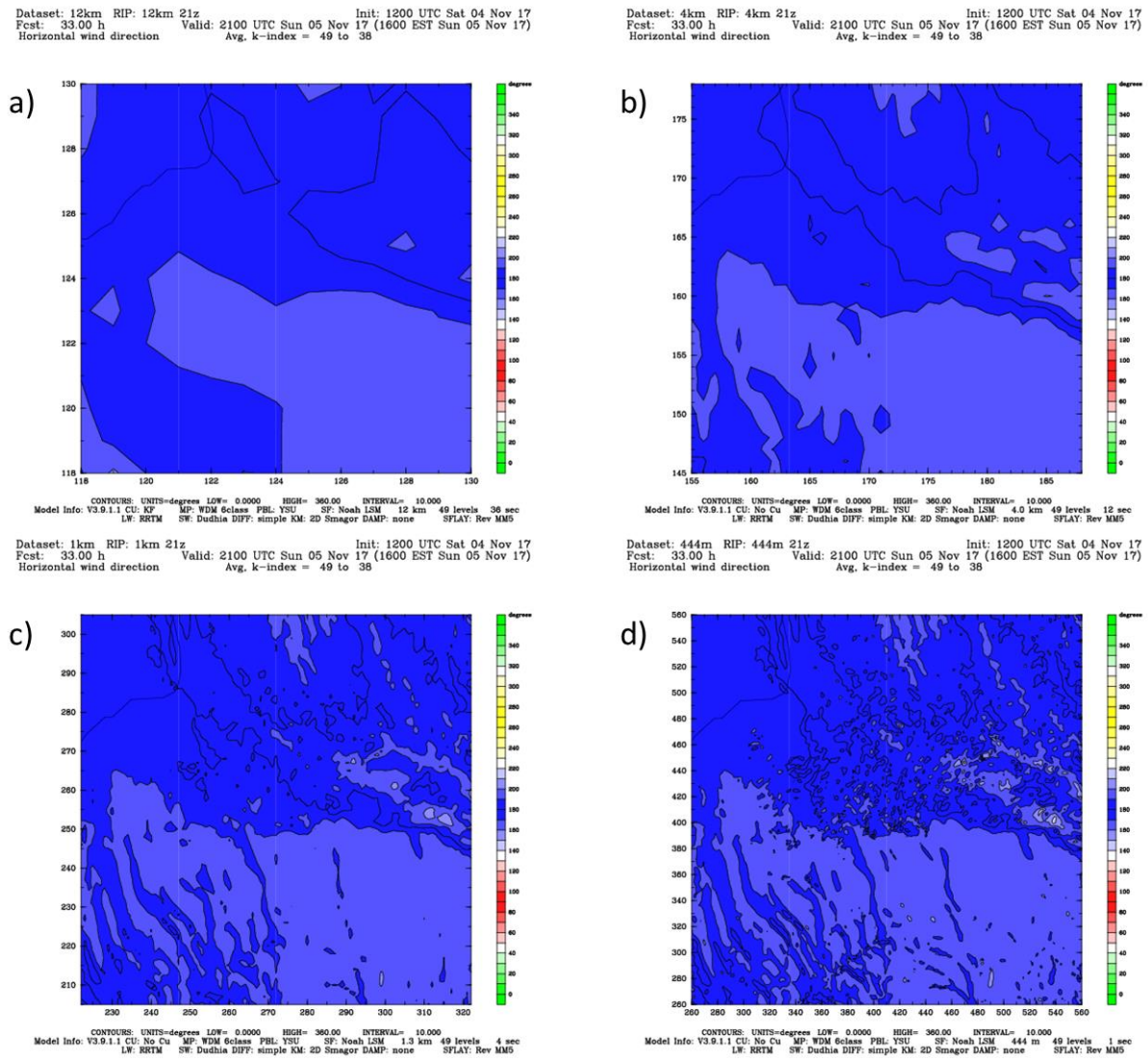

Fig. 23: As in Fig. 22, but at 21 UTC.

The north-south cross-sections of wind direction better exemplify the drainage flow, as easterly valley surface winds are notably present within each simulation at 13 UTC (Fig. 24). Similar to wind speed, the major discrepancy between each simulation is resolution of wave activity. While the 12 km domain expresses a gradual change in wind direction with height, the low-level variation increases with a decrease in Δx. Directional shear on the windward side of the

CV is captured by the 4 km, 1.33 km, and 0.444 km simulations. The easterly valley drainage flow is shown to reach higher elevations in the higher resolution domains. The afternoon wind direction cross-sections exhibit similar behavior to the horizontal plots, with southerly wind flow dominating the lower levels (Fig. 25). The vertical detail of the cross-sectional plots reveals surface easterly flow in each domain. Similar to previous results, an increase in wave detail is apparent with a decrease in Δx.

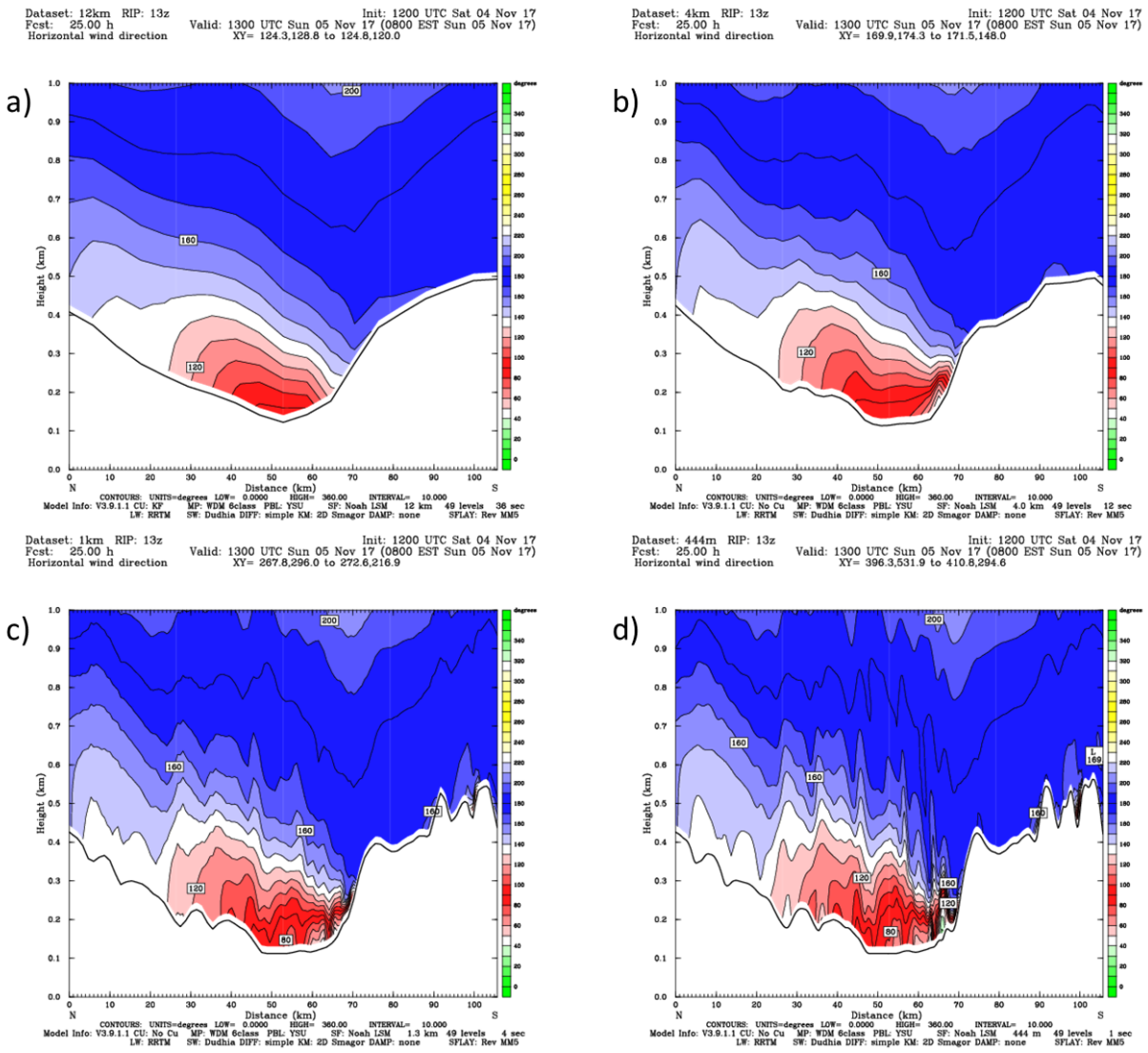

Fig. 24: North-south cross-sections of wind direction (°) at 13 UTC: a) 12 km, b) 4 km, c) 1.33 km, d) 0.444 km. Blue contours indicate southerly wind flow and red contours indicate easterly wind flow.

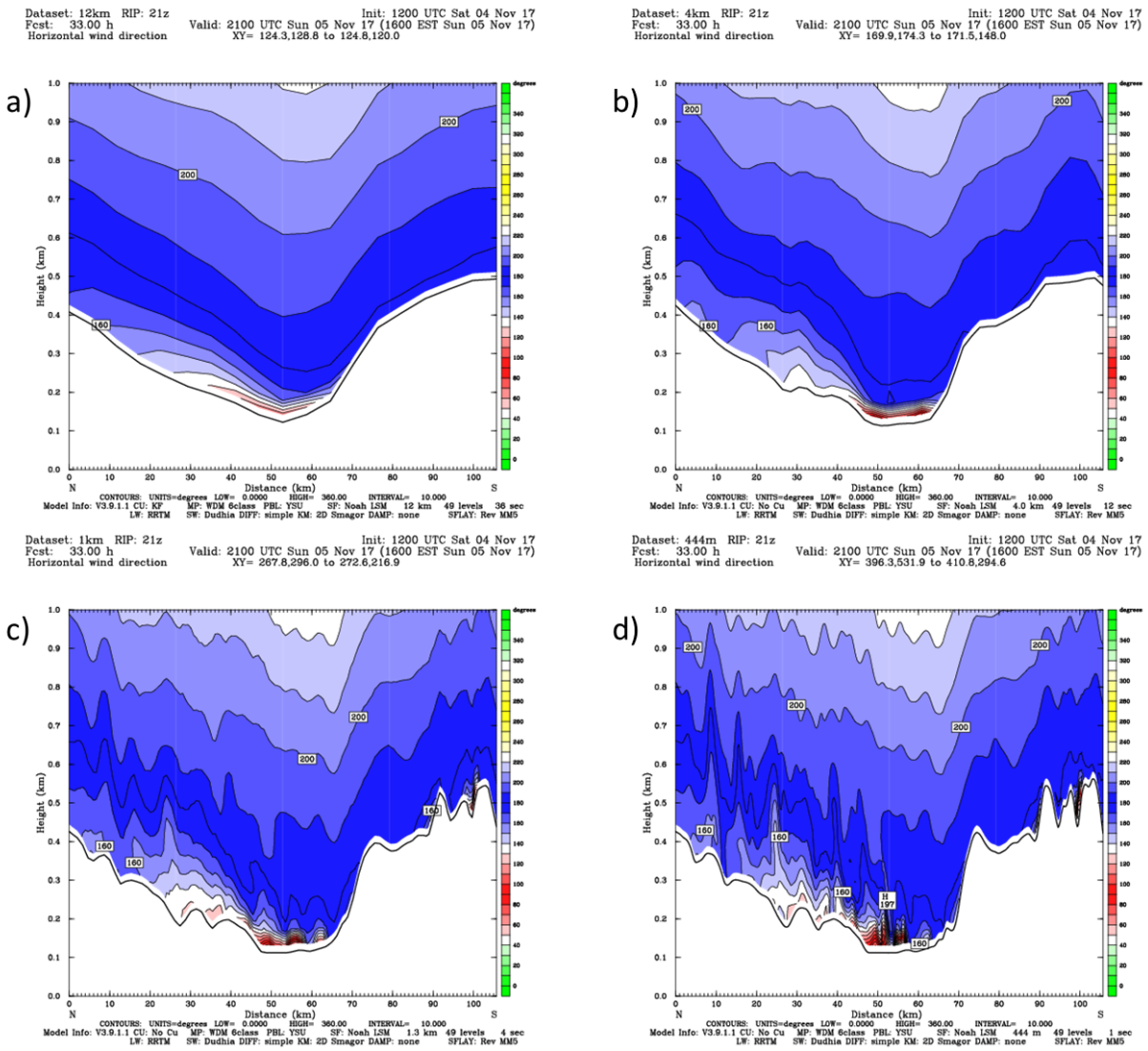

Fig. 25: As in Fig. 24, but at 21 UTC.

d. Vertical Velocity

Rising and sinking motions are a signature of the VC. For the 12 km and 4 km domains, 13 UTC model output shows sinking motion along the CV's walls with rising motion above its axis (Fig. 26). This detection of slope wind convergence and rising air in the valley's core is lost in the higher resolution simulations. Wave patterns detectable with a smaller Δx create a noisy

visualization of vertical velocity. While weaker in the coarse resolutions, each domain replicates a downdraft on the windward side of the valley that is coupled with an adjacent updraft. The downdraft magnitude is -30.77 cm s^{-1}, -47.29 cm s^{-1}, -69.0 cm s^{-1}, and -75.5 cm s^{-1} in the 12 km, 4 km, 1.33 km, and 0.444 km domains, respectively. The adjacent updraft difference is larger, with a magnitude of 38.74 cm s^{-1}, 53.63 cm s^{-1}, 135.7 cm s^{-1}, and 182.7 cm s^{-1} for each domain, respectively. Smaller Δx intervals show this behavior continuing within the air above the CV, with adjacently compact couplets.

Vertical motion fields are less chaotic by 21 UTC (Fig. 27). Sinking motion remains the primary feature of the CV's windward side for each domain. Aside from the 12 km domain, downdraft magnitudes have increased from 13 UTC with values of -26.32 cm s^{-1}, -75.8 cm s^{-1}, -106.5 cm s^{-1}, and -112.5 cm s^{-1} for each domain, respectively. The 12 km domain shows weak synoptic-scale vertical motions, while the 1.33 km and 0.444 km domains continue to resolve wave detail. Vertical motion couplets are more horizontally distributed throughout the domain in the higher resolution domains when compared to their 13 UTC model output. Notable ascent is resolved in each domain on the leeward side of the CV; ascent magnitudes are resolved as 20.02 cm s^{-1}, 44.34 cm s^{-1}, 82.7 cm s^{-1}, and 126.7 cm s^{-1} within each domain, respectively. Overall, the 0.444 km domain tends to resolve more vertical motions with higher magnitudes than other domains – including the 1.33 km Δx.

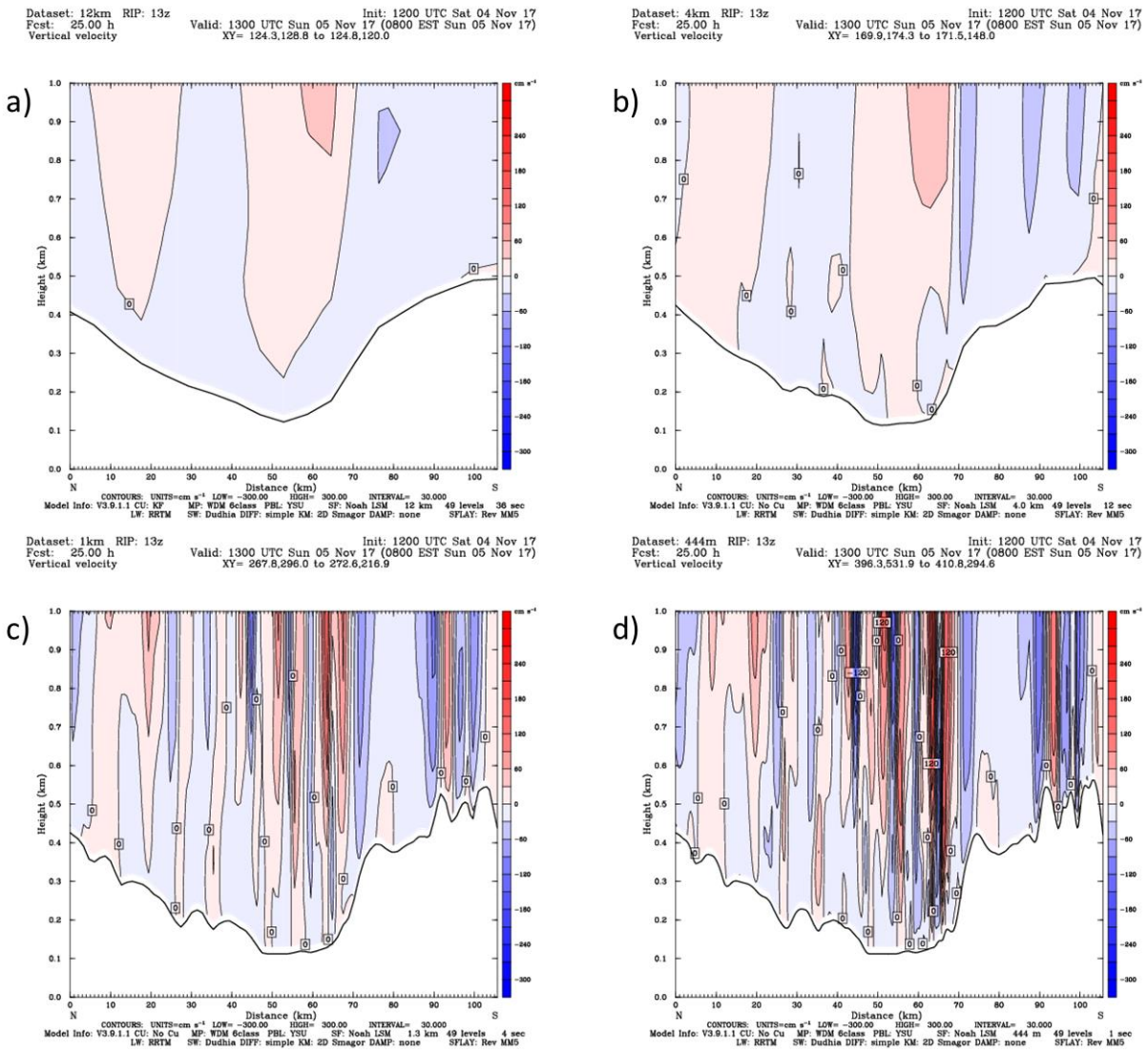

Fig. 26: North-south cross-sections of vertical velocity (cm s^{-1}) at 13 UTC: a) 12 km, b) 4 km, c) 1.33 km, d) 0.444 km. Blue contours indicate a sinking air and red contours illustrate rising air.

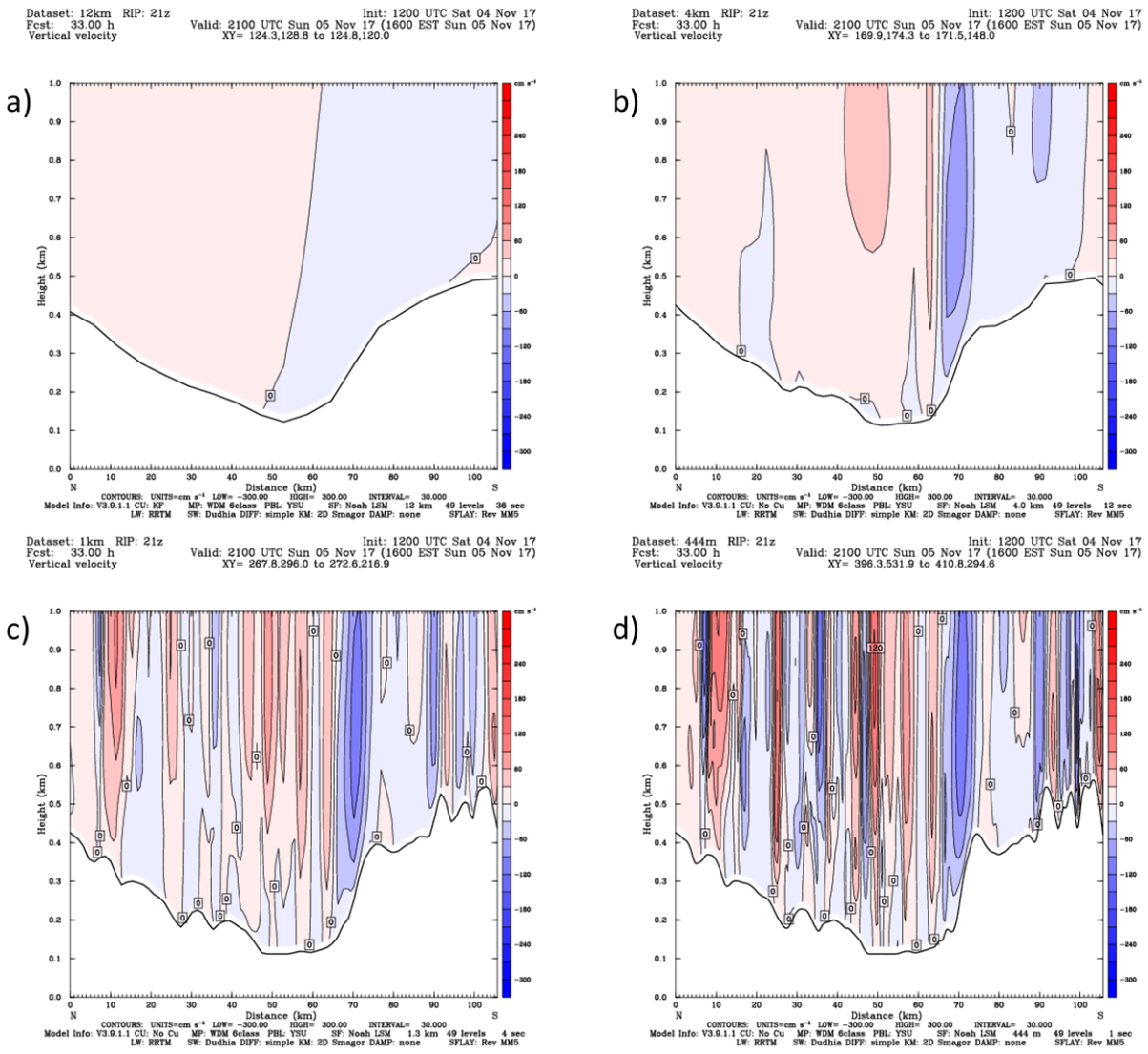

Fig. 27: As in Fig. 26, but at 21 UTC.

e. Temperature

Skew-T log-p diagrams for each domain are similar, with only minor differences. Thus, only the 12 km and 1.33 km profiles are provided for the WEST model location. This location was chosen to express the inversion resolution within the CV. Each domain resolves a surface inversion along with an overall stable profile at 13 UTC (Fig. 28). Inversion depth and detail is better

depicted by the 1.33 km resolution sounding. By 21 UTC this inversion erodes, and profiles typical of a well-mixed PBL are present in each domain (not shown).

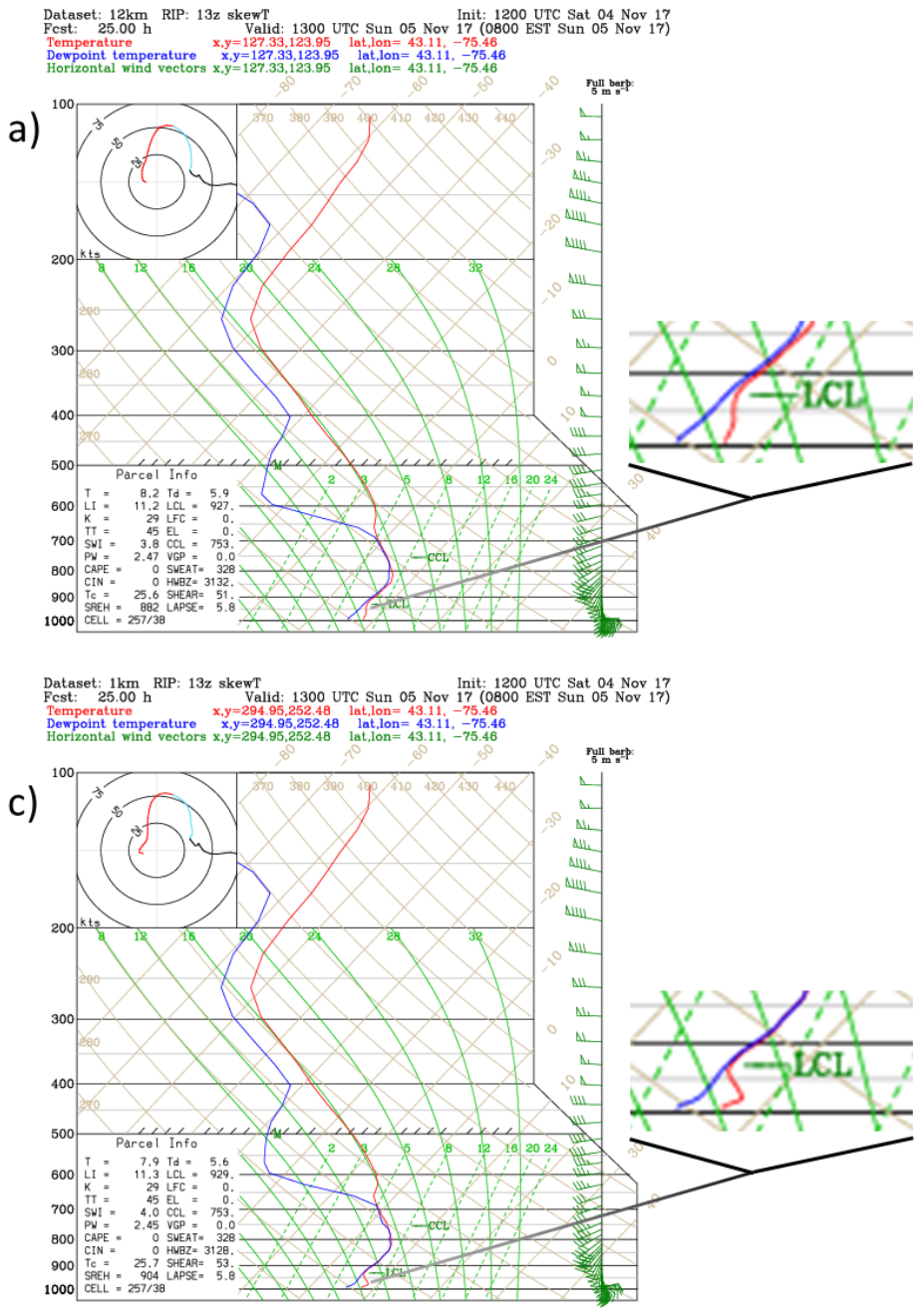

Fig. 28: Model produced skew-T log-p profiles along with hodographs and magnified surface inversions at 13 UTC for WEST: a) 12 km and c) 1.33 km. WEST provides a CV sounding

representation that depicts valley inversion resolution. Red and blue lines represent temperature (°C) and dewpoint (°C), respectively. Wind barbs (m s^{-1}) are provided for every model level in dark green along the right side of each image.

A better spatial visualization of temperature is provided through both horizontal and cross-sectional plots. Horizontal temperature plots at 13 UTC show a warm CV alongside cooler elevated terrain (Fig. 29). A smaller Δx results in better resolution of detailed temperature changes within complexities of the terrain. This is also apparent in the north-south CV temperature cross-section, as the 12 km and 4 km domains smooth over temperature differences that are resolved in the 1.33 km and 0.444 km domains (Fig. 30). Afternoon temperatures are not provided as PBL mixing leads to little temperature variation within the subdomains.

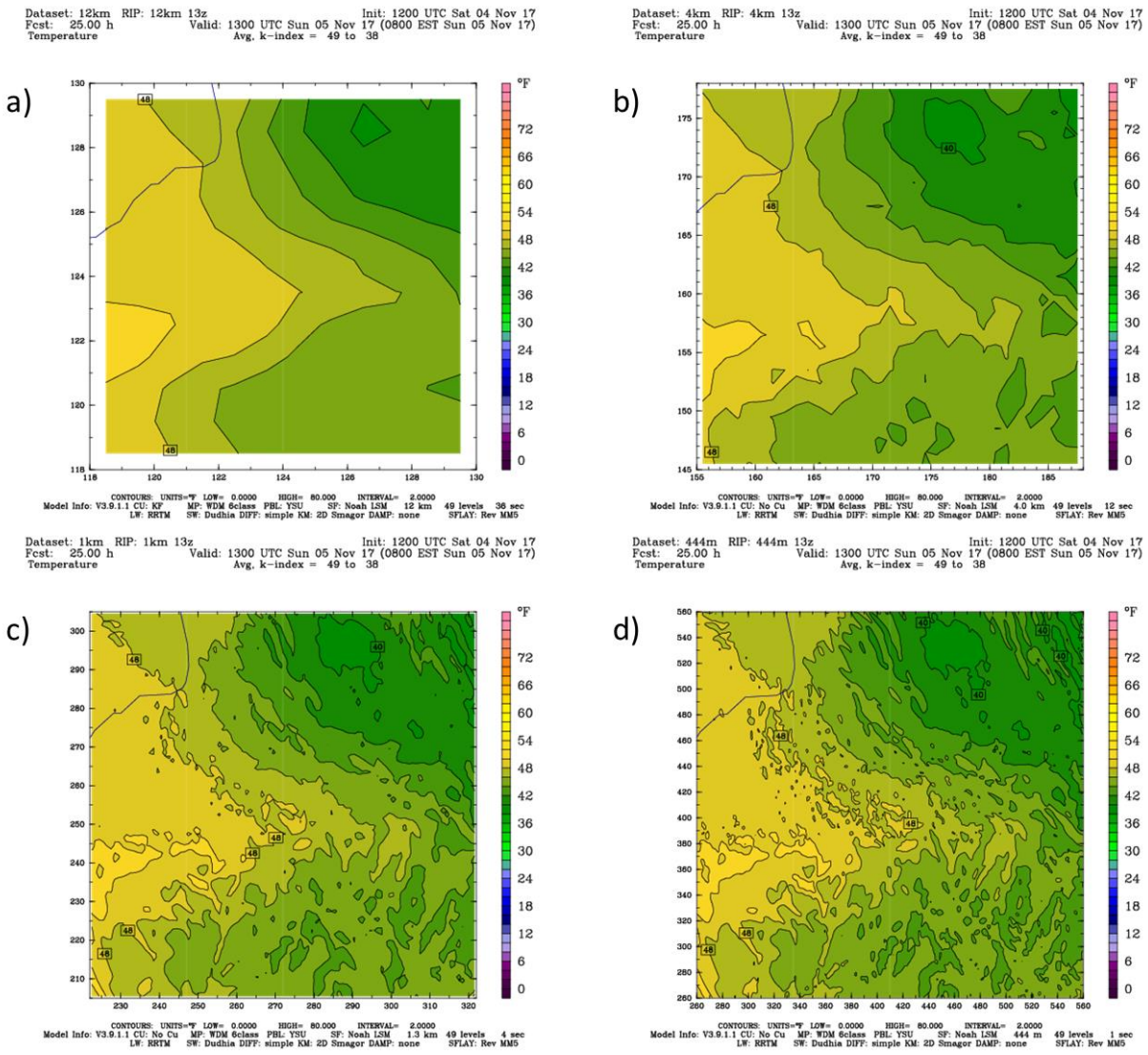

Fig. 29: Average low-level (surface up to model level 38: approximately 1600 ft MSL) temperature (°F) within each subdomain at 13 UTC: a) 12 km, b) 4 km, c) 1.33 km, d) 0.444 km. Yellow contours are indicative of higher temperatures.

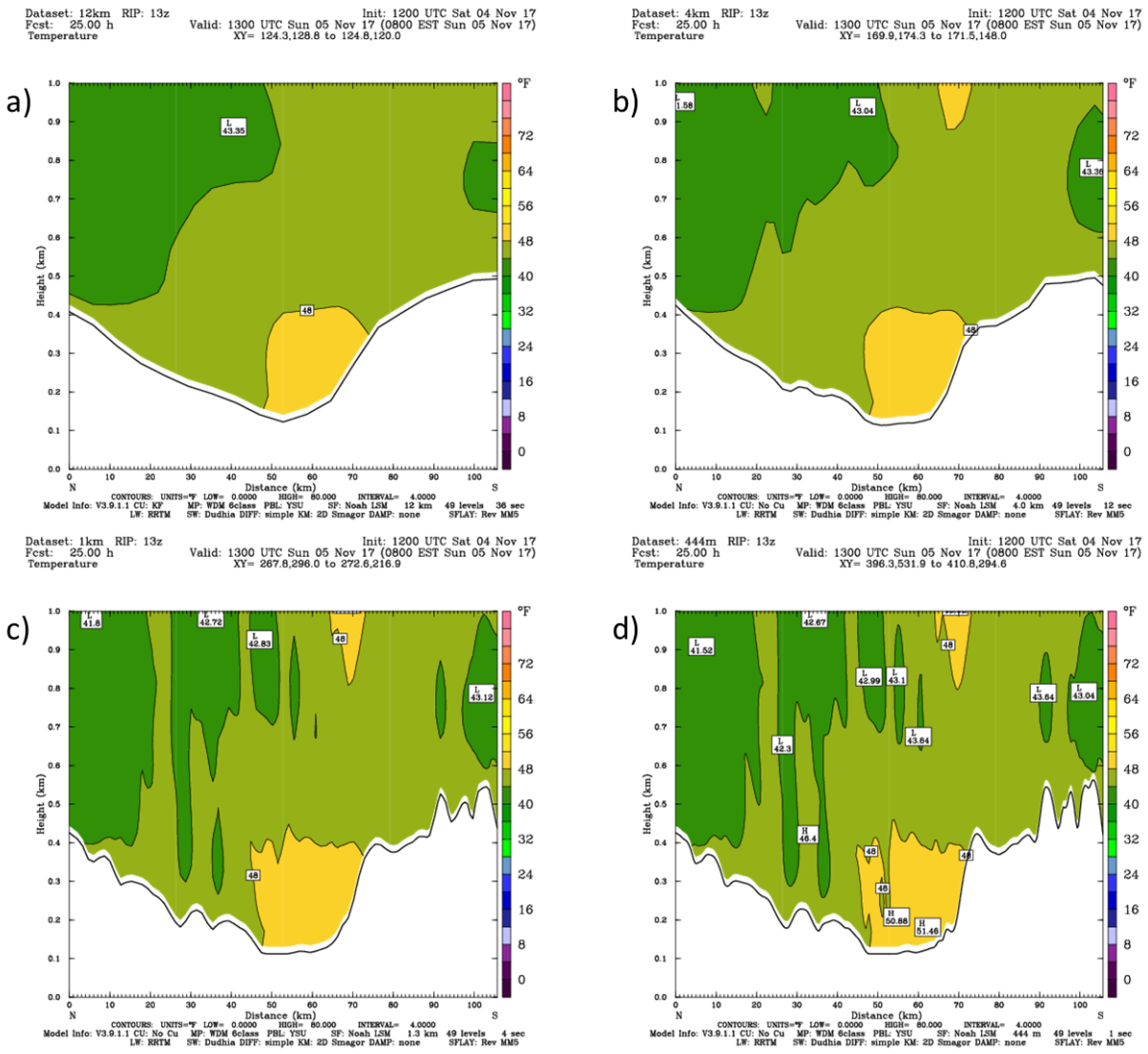

Fig. 30: North-south cross-sections of temperature (°F) at 13 UTC: a) 12 km, b) 4 km, c) 1.33 km, d) 0.444 km. Yellow contours are indicative of higher temperatures.

f. Airflow Stability

An estimation of whether airflow is turbulent or laminar — airflow stability — is provided by plotting the R_B. Unlike previous figures, Fig. 31 & Fig. 32 showcase an east-west CV axis cross-section as opposed to the north-south cross-section, as depicted in Fig. 13. Air is subject to

be turbulent throughout the north-south cross-section, apart from the CV's axis – therefore, R_B is better represented by an east-west cross-section. Turbulent surface flow is expected on the eastern side of the CV, while a stable layer of air ~50 m thick is simulated in each domain at 13 UTC (Fig. 31). This stable layer is rather smooth for the 12 km and 4 km Δx intervals. The 1.33 km and 0.444 km domains show more variation, likely resolving turbulent pockets of air within the stable layer and 300 m – 500 m above the surface. Furthermore, the 0.444 km domain shows pockets of unstable air aloft and turbulent air near the CV surface that are not detected with any other domain. By 21 UTC, the stable layer is much smaller in the 12 km, 4 km, and 1.33 km domains and non-existent in the 0.444 km domain (Fig. 32). Each domain suggests that turbulent flow may be present from the surface up to ~800 m, while more detailed pockets of turbulent air are resolved with higher resolution.

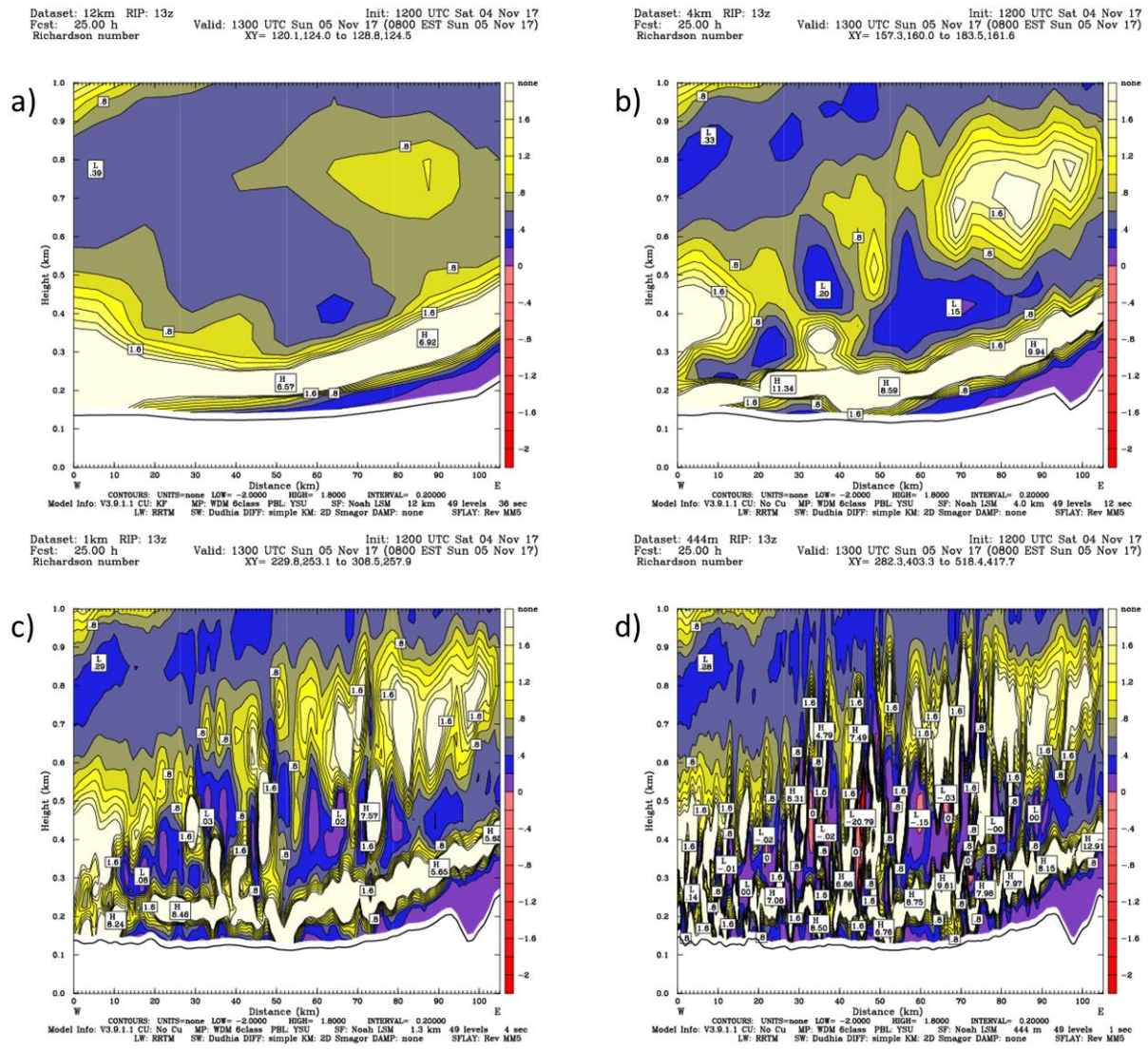

Fig. 31: East-west cross-section of R_B (unitless) at 13 UTC: a) 12 km, b) 4 km, c) 1.33 km, d) 0.444 km. Air becomes turbulent when $R_B \leq \sim 0.25$, as expressed by the purple contours. Red contours show unstable air that is likely turbulent. If turbulent air is present in the blue contours, it will remain turbulent. Turbulent airflow will become laminar for a $R_B \geq 1$, as indicated by the yellow and white contours. If laminar airflow enters an area of the blue contours, it will remain laminar.

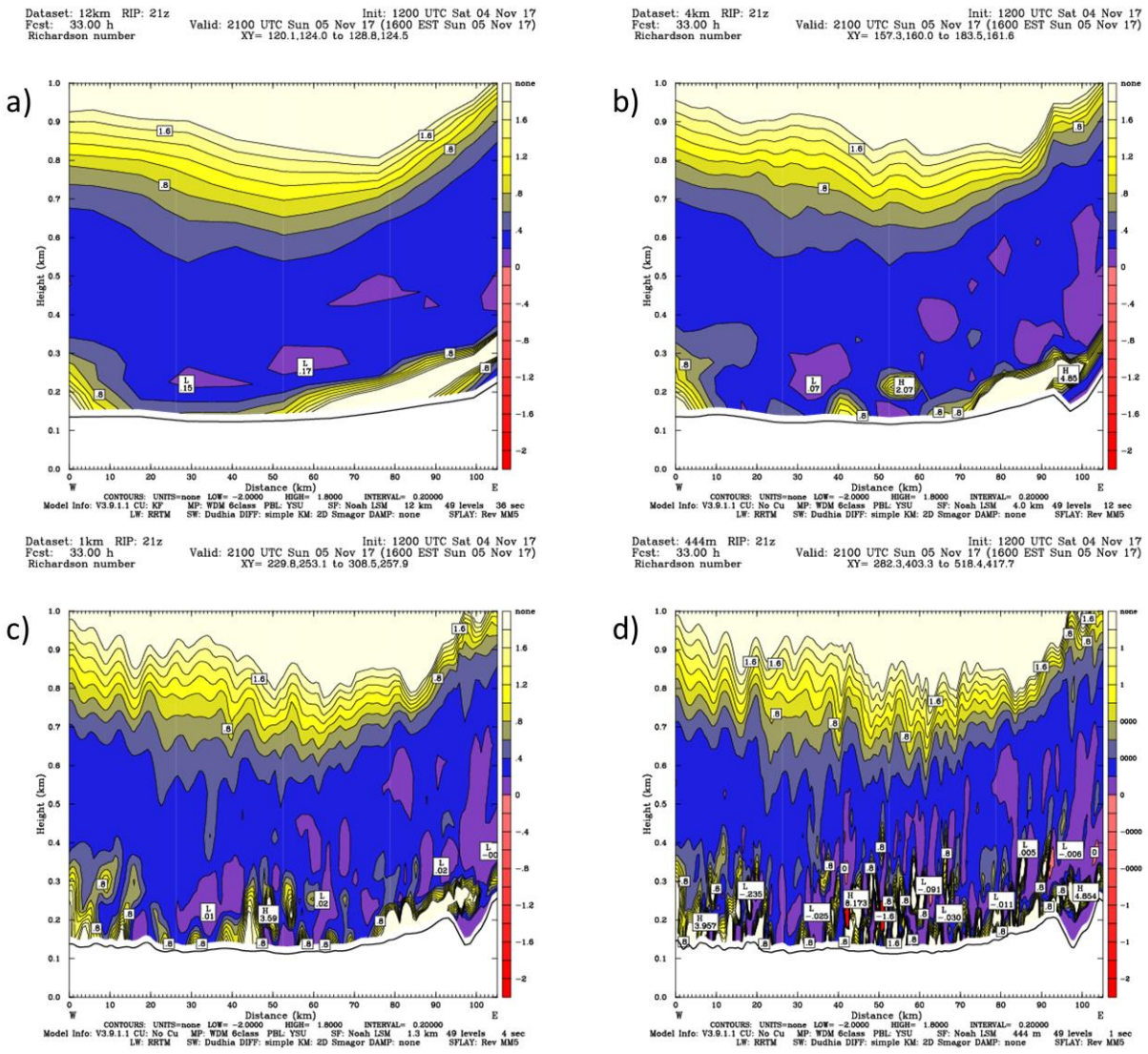

Fig. 32: As in Fig. 31, but at 21 UTC.

6. DISCUSSION

Comparison of model output to surface observations as a means of verification reveals difficulties with accurate replication of local wind speeds, while wind direction is generally well-simulated. The errant morning wind direction at the FAYE and JORD locations is likely relieved by the afternoon mixing of uniform southerly flow. Afternoon wind direction error at WEST

cannot be explained by the same means. Model errors in both wind speed and direction could rely upon the incorrect spatial and temporal simulation of wind features. In accordance to Wendell (1972), the passing of a warm front and its associated precipitation are subject to disturb the timing of local wind variations. The error in timing and intensity of model-produced precipitation is a likely contributor to this wind vector error. Error at the WEST location appears to be a result of the model simulation mistiming an atmospheric boundary – apparent by the phase shift between observations and model output in Fig. 17e. Each of these locations that exhibited notable wind direction error lie on the windward side of a drop off in terrain height, specifically the AP to the CV.

Terrain resolution remains imperfect – even with smaller Δx values. Terrain smoothing can result in the misrepresentation of NYSM locations within model output, suggesting that certain stations will experience larger model wind speed and/or direction error than others. Wind speed error is specifically notable at the WGAT and TULL locations; model output wind speed is a consistent overestimation at WGAT and underestimation at TULL (Fig. 14). WGAT is located north-east of the CV on the Adirondack Mountain slopes, while the TULL station resides within the AP (Fig. 12). In addition to terrain resolution issues, the wind speed bias in WRF is likely contributing to these errors. Utilizing the YSU and topo_wind schemes while compacting vertical σ levels within the lower atmosphere reduced the magnitude of error at WGAT and other NYSM locations by ~3 m s^{-1} when compared to previous model attempts. Such wind speed differences may also be the product of an increase in temperature resolution with a smaller Δx (Fig. 29 depicts the notable temperature variation within CNY's complex terrain). Further, higher resolution domain soundings better depicted inversion depth (Fig. 28). Increased resolution of local temperature inversions and gradients should enable better localized wind vector forecasts. In

addition, the 12 km simulation has the best wind-speed performance at WGAT. This relationship is also depicted by the five-minute data at GFLD; however, the opposite relationship is evident at OSCE (Fig. 15). Table 4 displays that, on average, the higher resolution domains incur higher wind speed errors while better capturing, at times overestimating, wind speed variability when compared to the coarse resolutions. The higher resolution wind speed errors are hypothesized to be a result of unoptimized parameterization performance at higher resolutions. The error discrepancy between model resolutions at certain station locations and the spikes in wind speed error are hypothesized to be a result of representativeness error. While an average error of ±1.9 m s^{-1} is encouraging to wind forecasts, the larger magnitude errors (e.g. -8 m s^{-1} at TULL) within the simulation window must be improved upon.

Differences between model output and observations impact a quality sUAS-centric forecast. Safe flights are enabled by risk evaluation, which is less accurate with an average error of ±1.9 m s^{-1} in areas of complex terrain along expected flight paths. Optimal flight path wind hazard identification would require reliable wind speed output. An operator's awareness of the modeled wind speed errors could result in delays or cancellation of flight – even when wind speeds are suitable for safe flight. With the incorporation of errors indicating an exceedance of a wind speed threshold, the operator would be taking a risk in conducting a planned flight. Over time, assimilation of sUAS flight observations will hopefully act to fill the sensing gaps and reduce wind speed errors by providing better knowledge of local wind patterns. This would immensely benefit the verification and accuracy of sUAS-centric modeling.

Discrepancies related to Δx are evident within the model output. While dependence of wind speed and direction on Δx show little difference for most locations, the features resolved by different Δx are significant. This agrees with the findings of Davis et al. (1999), where model

produced wind speed was similar for 80 km and 1.11 km Δx, but locally-forced circulations within the mountainous western United States were accurately depicted in the 1.11 km Δx. Comparison of the 12 km and 4 km domains with the 1.33 km and 0.444 km Δx domains exemplifies this, where wave activity is clear in the higher-resolution domains but mostly absent in lower-resolution domains. This level of detail comes about through the decreasing Nyquist frequency associated with a smaller Δx, allowing higher frequency waves to be replicated within model output. It is evident that an increase in terrain resolution with a decrease in Δx allows for a better simulation of overall wind structure. Resolution of these wave features causes differences in the spatial variation, and subsequent temporal evolution, of wind speed, wind direction, vertical velocity, temperature, and flow stability.

On the Weisman et al. (1997) premise that a successful simulation relies upon the onset of a phenomena, a smaller Δx is needed for a sUAS-centric model. Resolution of gravity wave activity reveals levels of both speed and directional wind shear, the presence and magnitude of vertical motions, and pockets of turbulent air. Wind shear identification, whether speed or directional, is crucial to proper battery management and flight safety, as the misidentification of a shear level can lead to an unexpected loss of battery life and result in a sUAS becoming significantly displaced. This displacement could force a sUAS into a pocket of turbulent air or an updraft that leads to a MAC or further loss of control, as was depicted in Fig. 5 & Fig 6. Identification of such features is first detected in the 4 km domain, but first notable in the 1.33 km Δx. For example, an operator flying on the simulated day in the CV would be encouraged to conduct a morning mission within laminar flow along the valley axis. Pockets of turbulent air within this laminar flow become more evident with a decrease in Δx (Fig. 31). The better identification of a near-neutral R_B alongside a more detailed vertical PBL profile, as depicted in

Fig. 28, will aid in avoiding areas prone to wind gusts, encouraging a safer flight (Gutiérrez and Fovell 2018). Assuming the use of a multi-rotor sUAS with an average flight speed of 15 m s^{-1} (Fig. 3), morning shear simulated at higher resolutions indicates both flyable and hazardous altitudes when compared to the coarser resolutions (Fig. 20 & Fig. 24). This increase in shear resolution with a decrease in Δx encourages better battery management and efficiency. Further, while 4 km output fails to detect apparent vertical motion on the windward side of the valley, investigation of the 1.33 km and 0.444 km Δx intervals suggests that pilots should avoid that area (Fig. 26). Essentially, use of a $\Delta x \leq 1.33$ km helps in identifying areas to avoid, enabling safer flight.

In terms of valley flow dynamics, the simulated case exhibits downward transport of momentum. Strong southerly flow acts to mix momentum aloft with the stable valley air, eroding the morning drainage flow from above, while surface heating acts to deepen the PBL within the valley. The combined mixing unifies overall wind direction by the afternoon. The downward transport of momentum was noted to be more common in wide valleys that are flat along their axis (Whiteman and Doran 1993); with the CV possessing these characteristics, the occurrence of this phenomenon is expected. This behavior is demonstrated by the higher resolution domains. It is hypothesized that the coarse resolutions couple the CV airflow with momentum aloft through the PBL mixing parameterization. Forced convection is encouraged by the high wind speeds, while free convection within the warming valley helps to link both regimes of airflow.

A gap flow was not present in this experiment. Wind channeling behavior was also not observed for any of the domains. Future experiments with conditions more conducive of both phenomena should consider the potential impacts upon sUAS.

Lower resolution simulations do provide value. While the higher resolution simulations better depict wave activity, the lower resolutions simulations can better depict the synoptic and higher bounds of the meso-alpha scales. This study revealed a morning VC with sinking slope winds, rising air in the center of the CV, and drainage flow. While the drainage flow was evident for each domain, the coarse resolutions best show slope wind behavior (Fig. 26). A smaller Δx captures local vertical motions that make it harder to visualize larger-scale ascent/descent that is apparent with coarser domains. Filtering the high frequency wavelengths resolved within the high-resolution domains allows for better visualization of the larger scale flow patterns (Fig. 33). Understanding flow at multiple scales allows a forecaster to better identify the overall flow dynamic – resulting in a better forecast. In addition, results show that the coarse domains handled the afternoon hours rather well. Aside from the resolution of thermals, PBL mixing appears to be handled well for each domain. Such behavior is apparent in the minor differences for afternoon temperatures and overall wind speeds in each domain. More notable is the magnitude of the wind speed maximum above the windward side of the CV, where the afternoon instability works to reduce its magnitude across each domain equally.

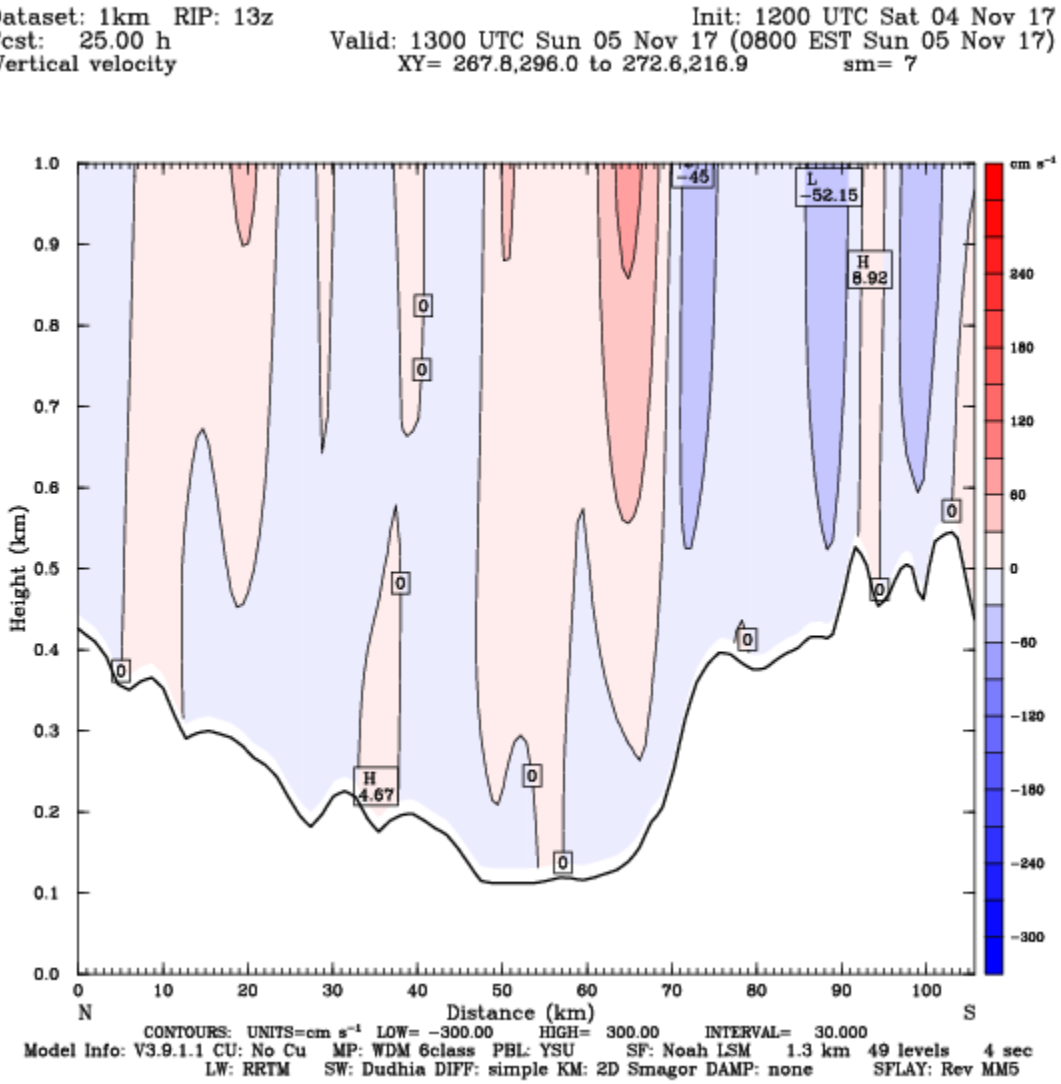

Fig. 33: North-south cross-section of vertical velocity (cm s^{-1}) at 13 UTC for the 1.33 km domain with a 7-factor Cressman weighting function applied. Blue contours indicate a sinking air and red contours illustrate rising air.

Further value of coarse domains derives from their quick execution. The same amount of computational power to produce one high-resolution deterministic simulation can be used to produce several relatively coarse resolutions simultaneously. The latter, an ensemble approach,

provides multiple realizations of model output that can help with forecasting wind hazards. With enough computational power, this ensemble could be improved upon, utilizing several PBL parameterizations and resolutions. The resulting probabilistic product, previously referred to as a threat index, could best allow a sUAS operator to conduct safe and efficient flight. Results encourage a sUAS-centric ensemble approach to include simulations with a Δx of at least 1.33 km. However, computational cost for such simulations can be a significant barrier.

High spatial and temporal resolutions inevitably incur higher computational cost. However, high resolution simulations allow for the visualization of output data at a high spatial density and temporal frequency, supporting precise sUAS mission planning. When attempting to plan a local mission, the spatial density of small Δx simulations provides drastically more information than that associated with a large Δx simulation (Fig. 34). Except for the 12 km image, each domain in Fig. 34 is filtered to enable readability; the 4 km, 1.33 km, and 0.444 km domain images show wind barbs every second, fifth, and twelfth grid point, respectively. Thus, local wind fields and inversion heights are best depicted by the spatially dense smaller Δx intervals. In addition, the affordability of computational storage should alleviate any issues associated with the file size of model output and allow for visualizations having high-temporal resolution.

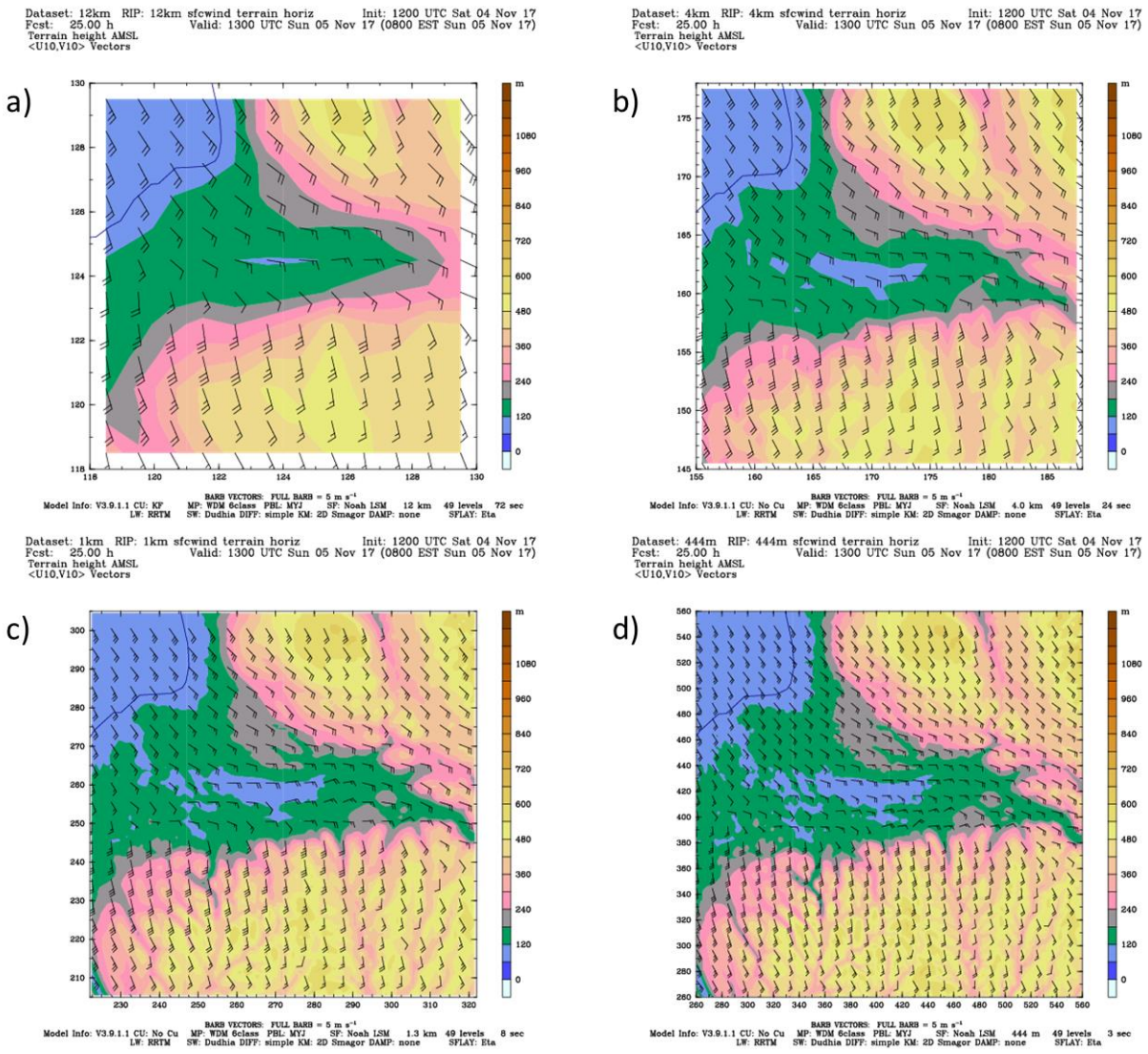

Fig. 34: Contoured MSL terrain along with 10 m wind barbs (m s^{-1}) within each subdomain at 13 UTC: a) 12 km, b) 4 km, c) 1.33 km, d) 0.444 km. Full wind barb depicts 5 m s^{-1}.

Decreasing both Δx and Δt becomes necessary to spatially and temporally resolve wave patterns that are relevant to ensuring safe sUAS flight. Results show that a Δx as small as 1.33 km may be necessary to resolve these wave features. Resolution of wave features is crucial to the entrainment process, as it determines the local inversion height within a valley and, thus, a local

wind shear maximum. A Δx smaller than 1.33 km, such as the 0.444 km domain, intensifies the detected wave features, suggesting that terrain complexities smaller than the CV system may require smaller Δx—a Large-Eddy Simulation (LES)—to ensure safe flight. The associated decrease in Δt causes for an increase in simulation time. In order to maintain stability with a high concentration of vertical levels within the sUAS flight altitudes, a required decrease in Δt can effectively double simulation time. Access to a supercomputer or private computer built and budgeted specifically for modeling at a small Δx then becomes necessary for producing model output. Operators may be required to wait for a model simulation to finish before conducting flight – a temporally efficient simulation is desirable. Simulating up to 1.33 km would reduce the present experiment's 4-hour simulation time by a significant amount, and, with proper planning, would allow for consistent, temporally available model output.

a. Future Work

The shortcomings of this experiment hinge upon verification and ambient weather conditions. A less complex simulation day could enable a better evaluation of wind vectors; this experiment's precipitation complicates the already complicated issue of resolving localized wind flows. However, situations similar to this simulation day are when NWP will be most needed and relied upon by sUAS operators. Therefore, future investigation of each weather parameter discussed in Chapter 2 and their associated phenomena resolved within higher resolutions is ideal for defining an optimal approach to sUAS-centric modeling.

In order to achieve a computationally desirable model simulation, experiments like this should be conducted for a variety of wind flow regimes in areas of varying terrain. These tests should consider the influences of: the season being simulated, surrounding complex terrain, removal/addition of condensed PBL vertical levels, and different available parameterizations.

Additional or different parameterizations could enhance high resolution model output. An estimate of Turbulent Kinetic Energy (TKE), the intensity of turbulence, is produced by the Mellor-Yamada-Janjic (MYJ) PBL scheme. Such an estimate could better identify areas hazardous to sUAS. Further, implementing a well-tested, regional gust factor parameterization would be invaluable to sUAS wind hazard detection. Use of the aforementioned "slope_rad" and "topo_shading" options could also prove beneficial for WRF model simulations within areas of complex terrain.

7. CONCLUSIONS

The WRF model is a valuable tool for predicting hazardous wind regimes. The goal of the present study is to depict the dependence of winds on resolution. The CNY area, specifically the CV, was chosen to analyze how wind behavior within complex terrain would change with an increasing resolution. The primary application of this study pertains to sUAS. Efficient commercial operation of sUASs will rely upon quality wind forecasts. NWP can help operators identify and avoid areas of hazardous winds that can result in loss of sUAS control.

Wind speed simulation with WRF has been shown to include a bias within areas of complex terrain (Jimenez and Dudhia 2012; Lee et al. 2015). While application of the topo_wind parameterization and increased low level vertical resolution help in reducing the bias, some bias persists. This is apparent through comparison of NYSM observation and model output data, where errors were as large as -8 m s^{-1} at TULL, a station surrounded by complex terrain, for all domains. Hypotheses for wind speed error, aside from the WRF model's bias, are the unoptimized parameterization performance at higher resolutions and representativeness error. Data assimilation

and better verification metrics supplied by localized sUAS flight data for future simulations may help to reduce this error. Further, the integration of artificial intelligence/machine learning could help with identification and avoidance of areas that prove to be frequently hazardous.

Identification of a VC within this simulation was best visualized through use of each resolution. Detail that arises with use of higher resolution reveals the entrainment of turbulent air aloft with the CV's stable regime. While each domain displayed similar performance for the afternoon hours, the temporal evolution of atmospheric waves is captured better with higher resolutions. Use of small Δx intervals and compacted vertical levels enables the better simulation of a wind hazard's magnitude and temporal evolution.

Enhancing wind hazard identification through use of higher resolutions is necessary to ensure safe sUAS operations. It is important to consider that even with small Δx (and corresponding Δt values), a correct forecast is not guaranteed (Rife et al. 2004). The value in reducing these intervals pairs well with human interpretation. Comparison of model output shows that a deterministic simulation using 1.33 km grid spacing can provide enough information to support a well-informed, human interpreted forecast that helps sUAS operators avoid of hazardous winds. A nested simulations approach allows for a forecaster to evaluate coarse resolutions as well, in this case the 12 km and 4 km domains, to better understand large-scale impacts on local forcing. This can be improved upon with an ensemble approach, provided computational power is available. An optimal high-resolution simulation is hypothesized by Mass et al. (2002), in which an ensemble model is used to resolve relatively large-scale motions that are then weighted based upon performance to produce an average. This average would then provide the forcing conditions for a set of higher resolution simulations. Conducting several simulations that utilize various PBL

schemes and resolutions will improve a sUAS centric forecast – especially if ensemble output is paired with human interpretation (e.g. a forecast discussion).

APPENDIX

List of Acronyms

(in order of appearance):

small Unmanned Aircraft System (sUAS)

Beyond Visual Line Of Sight (BVLOS)

Line Of Sight (LOS)

Unmanned Aircraft (UA)

Federal Aviation Administration (FAA)

Central New York (CNY)

Allegheny Plateau (AP)

Central Valley (CV)

Numerical Weather Prediction (NWP)

Weather Research and Forecasting (WRF) model

Horizontal Grid Spacing (Δx)

New York State Mesonet (NYSM)

Unmanned Aircraft System (UAS)

Visual Line of Sight (VLOS)

Detect And Avoid (DAA)

Mid-Air Collision (MAC)

Above Ground Level (AGL)

Planetary Boundary Layer (PBL)

Mixed Layer (ML)

Mean Sea Level (MSL)

Valley Circulation (VC)

North American Regional Reanalysis (NARR)

United States Geological Survey (USGS)

Cumulus Parameterization (CP)

WRF Double Moment Six Class scheme (WDM6)

Microphysical Parameterization (MP)

Land Surface Model (LSM)

Longwave (LW)

Shortwave (SW)

Rapid Radiative Transfer Model (RRTM)

Yonsei University Scheme (YSU)

Model Time-Step (Δt)

University Corporation for Atmospheric Research (UCAR)

National Center for Atmospheric Research (NCAR)

Computational and Information Systems Lab (CISL)

Bulk Richardson Number (R_B)

Belleville (BELL)

Camden (CAMD)

Cold Brook (COLD)

Central Square (CSQR)

Fayetteville (FAYE)

Glenfield (GFLD)

Harrisburg (HARR)

Herkimer (HERK)

Jordan (JORD)

Morrisville (MORR)

Osceola (OSCE)

Redfield (REDF)

Tully (TULL)

Westmoreland (WEST)

Woodgate (WGAT)

Read Interpolate Plot (RIP)

Large Eddy Simulation (LES)

Turbulent Kinetic Energy (TKE)

Mellor-Yamada-Janjic (MYJ)

REFERENCES

Askelson, M., B. M. Trapnell, C. Theisen, R. Arthur, T. Young, and H. Reza, 2013: Airspace Risk Mitigation System.

Brouwers, E. W., J. L. Palacios, E. C. Smith, and A. A. Peterson, 2010: THE EXPERIMENTAL INVESTIGATION OF A ROTOR HOVER ICING MODEL WITH SHEDDING. 17.

Carrera, M. L., J. R. Gyakum, and C. A. Lin, 2009: Observational Study of Wind Channeling within the St. Lawrence River Valley. *J. Appl. Meteorol. Climatol.*, **48**, 2341–2361, https://doi.org/10.1175/2009JAMC2061.1.

Carvalho, D., A. Rocha, M. Gómez-Gesteira, and C. Santos, 2012: A sensitivity study of the WRF model in wind simulation for an area of high wind energy. *Environ. Model. Softw.*, **33**, 23–34, https://doi.org/10.1016/j.envsoft.2012.01.019.

Davis, C., T. Warner, E. Astling, and J. Bowers, 1999: Development and application of an operational, relocatable, mesogamma-scale weather analysis and forecasting system. *Tellus Dyn. Meteorol. Oceanogr.*, **51**, 710–727, https://doi.org/10.3402/tellusa.v51i5.14490.

Drone Registration, 2016: Safety Tips for Using Lithium Polymer (Li-Po) Batteries. https://drone-registration.net/safety-tips-li-po-batteries/ (Accessed August 28, 2019).

Dudhia, J., 1988: Numerical Study of Convection Observed during the Winter Monsoon Experiment Using a Mesoscale Two-Dimensional Model. *J. Atmospheric Sci.*, **46**, 3077–3107, https://doi.org/10.1175/1520-0469(1989)046<3077:NSOCOD>2.0.CO;2.

FAA, 1975: Aviation Weather for Pilots and Flight Operations Personnel. *Icing Cloud Types*. https://www.aviationweather.ws/053_Icing_and_Cloud_Types.php.

——, 2016: Operation and Certification of Small Unmanned Aircraft Systems. *Fact Sheet – Small Unmanned Aircr. Regul. Part 107*. https://www.faa.gov/news/fact_sheets/news_story.cfm?newsId=20516.

Gross, G., and F. Wippermann, 1987: Channeling and Countercurrent in the Upper Rhine Valley: Numerical Simulations. *J. Clim. Appl. Meteorol.*, **26**, 1293–1304, https://doi.org/10.1175/1520-0450(1987)026<1293:CACITU>2.0.CO;2.

Gutiérrez, A., and R. G. Fovell, 2018: A new gust parameterization for weather prediction models. *J. Wind Eng. Ind. Aerodyn.*, **177**, 45–59, https://doi.org/10.1016/j.jweia.2018.04.005.

Hansman, R. J., and A. P. Craig, 1987: Low Reynolds number tests of NACA 64-210, NACA 0012, and Wortmann FX67-K170 airfoils in rain. *J. Aircr.*, **24**, 559–566, https://doi.org/10.2514/3.45476.

Harris, A. R., and J. D. W. Kahl, 2017: Gust Factors: Meteorologically Stratified Climatology, Data Artifacts, and Utility in Forecasting Peak Gusts. *J. Appl. Meteorol. Climatol.*, **56**, 3151–3166, https://doi.org/10.1175/JAMC-D-17-0133.1.

Hong, S.-Y., and J. Dudhia, 2012: Next-Generation Numerical Weather Prediction: Bridging Parameterization, Explicit Clouds, and Large Eddies. *Bull. Am. Meteorol. Soc.*, **93**, ES6–ES9, https://doi.org/10.1175/2011BAMS3224.1.

——, Y. Noh, and J. Dudhia, 2006: A New Vertical Diffusion Package with an Explicit Treatment of Entrainment Processes. *Mon. Weather Rev.*, **134**, 2318–2341, https://doi.org/10.1175/MWR3199.1.

Jiménez, P. A., and J. Dudhia, 2012: Improving the Representation of Resolved and Unresolved Topographic Effects on Surface Wind in the WRF Model. *J. Appl. Meteorol. Climatol.*, **51**, 300–316, https://doi.org/10.1175/JAMC-D-11-084.1.

——, J. F. González-Rouco, E. García-Bustamante, J. Navarro, J. P. Montávez, J. V.-G. de Arellano, J. Dudhia, and A. Muñoz-Roldan, 2010a: Surface Wind Regionalization over Complex Terrain: Evaluation and Analysis of a High-Resolution WRF Simulation. *J. Appl. Meteorol. Climatol.*, **49**, 268–287, https://doi.org/10.1175/2009JAMC2175.1.

——, ——, J. Navarro, J. P. Montávez, and E. García-Bustamante, 2010b: Quality Assurance of Surface Wind Observations from Automated Weather Stations. *J. Atmospheric Ocean. Technol.*, **27**, 1101–1122, https://doi.org/10.1175/2010JTECHA1404.1.

——, J. Dudhia, J. F. González-Rouco, J. Navarro, J. P. Montávez, and E. García-Bustamante, 2011: A Revised Scheme for the WRF Surface Layer Formulation. *Mon. Weather Rev.*, **140**, 898–918, https://doi.org/10.1175/MWR-D-11-00056.1.

Kain, J. S., 2004: The Kain–Fritsch Convective Parameterization: An Update. *J. Appl. Meteorol.*, **43**, 170–181, https://doi.org/10.1175/1520-0450(2004)043<0170:TKCPAU>2.0.CO;2.

Lee, J., H. H. Shin, S.-Y. Hong, P. A. Jiménez, J. Dudhia, and J. Hong, 2015: Impacts of subgrid-scale orography parameterization on simulated surface layer wind and

monsoonal precipitation in the high-resolution WRF model. *J. Geophys. Res. Atmospheres*, **120**, 644–653, https://doi.org/10.1002/2014JD022747.

Lim, K.-S. S., and S.-Y. Hong, 2009: Development of an Effective Double-Moment Cloud Microphysics Scheme with Prognostic Cloud Condensation Nuclei (CCN) for Weather and Climate Models. *Mon. Weather Rev.*, **138**, 1587–1612, https://doi.org/10.1175/2009MWR2968.1.

Markowski, P., and Y. Richardson, 2010: *Mesoscale Meteorology in Midlatitudes*. John Wiley & Sons, Ltd, 407 pp.

Marshall, D. M., R. K. Barnhart, E. Shappee, and M. Most, 2016: *Introduction to Unmanned Aircraft Systems*. Second Edition. CRC LLC, 1–2 pp.

Mass, C. F., D. Ovens, K. Westrick, and B. A. Colle, 2002: Does increasing horizontal resolution produce more skillful forecasts? *Bull. Am. Meteorol. Soc.*, **83**, 407–430, https://doi.org/10.1175/1520-0477(2002)083<0407:DIHRPM>2.3.CO;2.

Mayr, G. J., and Coauthors, 2007: Gap flows: Results from the Mesoscale Alpine Programme. *Q. J. R. Meteorol. Soc.*, **133**, 881–896, https://doi.org/10.1002/qj.66.

Mlawer, E. J., S. J. Taubman, P. D. Brown, M. J. Iacono, and S. A. Clough, 1997: Radiative transfer for inhomogeneous atmospheres: RRTM, a validated correlated-k model for the longwave. *J. Geophys. Res. Atmospheres*, **102**, 16663–16682, https://doi.org/10.1029/97JD00237.

Monin, A. S., and A. M. Obukhov, 1954: Basic laws of turbulent mixing in the surface layer of the atmosphere. 30.

NOAA, 2013: Definitions: Wind Gust. *Wind Gust*. http://graphical.weather.gov/definitions/defineWindGust.html (Accessed August 28, 2019).

Pérez, J. C., J. P. Díaz, A. González, J. Expósito, F. Rivera-López, and D. Taima, 2014: Evaluation of WRF Parameterizations for Dynamical Downscaling in the Canary Islands. *J. Clim.*, **27**, 5611–5631, https://doi.org/10.1175/JCLI-D-13-00458.1.

Politovich, M. K., 2015: *Encyclopedia of Atmospheric Sciences*. Second. Elsevier, 160–165 pp.

Rampanelli, G., D. Zardi, and R. Rotunno, 2004: Mechanisms of Up-Valley Winds. *J. Atmospheric Sci.*, **61**, 3097–3111, https://doi.org/10.1175/JAS-3354.1.

Rife, D. L., C. A. Davis, Y. Liu, and T. T. Warner, 2004: Predictability of Low-Level Winds by Mesoscale Meteorological Models. *Mon. Weather Rev.*, **132**, 2553–2569, https://doi.org/10.1175/MWR2801.1.

——, ——, and J. C. Knievel, 2009: Temporal Changes in Wind as Objects for Evaluating Mesoscale Numerical Weather Prediction. *Weather Forecast.*, **24**, 1374–1389, https://doi.org/10.1175/2009WAF2222223.1.

Roebber, P. J., and J. R. Gyakum, 2003: Orographic Influences on the Mesoscale Structure of the 1998 Ice Storm. *Mon. Weather Rev.*, **131**, 27–50, https://doi.org/10.1175/1520-0493(2003)131<0027:OIOTMS>2.0.CO;2.

Rontu, L., 2006: A study on parametrization of orography-related momentum fluxes in a synoptic-scale NWP model. *Tellus Dyn. Meteorol. Oceanogr.*, **58**, 69–81, https://doi.org/10.1111/j.1600-0870.2006.00162.x.

Shin, H. H., and S.-Y. Hong, 2013: Analysis of Resolved and Parameterized Vertical Transports in Convective Boundary Layers at Gray-Zone Resolutions. *J. Atmospheric Sci.*, **70**, 3248–3261, https://doi.org/10.1175/JAS-D-12-0290.1.

Skamarock, C., and Coauthors, 2008: A Description of the Advanced Research WRF Version 3. https://doi.org/10.5065/D68S4MVH.

Steeneveld, G.-J., and J. Vilà-Guerau de Arellano, 2019: Teaching Atmospheric Modeling at the Graduate Level: 15 Years of Using Mesoscale Models as Educational Tools in an Active Learning Environment. *Bull. Am. Meteorol. Soc.*, **100**, 2157–2174, https://doi.org/10.1175/BAMS-D-17-0166.1.

Stoelinga, M. T., and Coauthors, 2018: Users' Guide to RIP Version 4.7: A Program for Visualizing Mesoscale Model Output. https://www2.mmm.ucar.edu/wrf/users/docs/ripug.htm.

Tewari, M., F. Chen, W. Wang, J. Dudhia, M. A. LeMone, G. Gayno, J. Wegiel, and R. H. Cuenca, 2004: 14.2A IMPLEMENTATION AND VERIFICATION OF THE UNIFIED NOAH LAND SURFACE MODEL IN THE WRF MODEL. 6.

UAS Summit, 2019: UAS Summit & Expo. *Speak. Present. Available UAS Connect 2019*. http://www.theuassummit.com/ema/DisplayPage.aspx?pageId=Past_Presentations (Accessed August 27, 2019).

Warner, J. T., 2015: *The Handbook of Lithium-Ion Battery Pack Design*. Elsevier Amsterdam, 65–130 pp.

Warner, T. T., 2011: *Numerical Weather and Climate Prediction*. Cambridge University, 526 pp.

Weigel, A. P., F. K. Chow, M. W. Rotach, R. L. Street, and M. Xue, 2006: High-Resolution Large-Eddy Simulations of Flow in a Steep Alpine Valley. Part II: Flow Structure and Heat Budgets. *J. Appl. Meteorol. Climatol.*, **45**, 87–107, https://doi.org/10.1175/JAM2323.1.

Weisman, M. L., W. C. Skamarock, and J. B. Klemp, 1997: The Resolution Dependence of Explicitly Modeled Convective Systems. *Mon. Weather Rev.*, **125**, 527–548, https://doi.org/10.1175/1520-0493(1997)125<0527:TRDOEM>2.0.CO;2.

——, C. Davis, W. Wang, K. W. Manning, and J. B. Klemp, 2008: Experiences with 0–36-h Explicit Convective Forecasts with the WRF-ARW Model. *Weather Forecast.*, **23**, 407–437, https://doi.org/10.1175/2007WAF2007005.1.

Wendell, L. L., 1972: Mesoscale Wind Fields and Transport Estimates Determined From a Network of Wind Towers. *Mon. Weather Rev.*, **100**, 565–578, https://doi.org/10.1175/1520-0493(1972)100<0565:MWFATE>2.3.CO;2.

Whiteman, C. D., and J. C. Doran, 1993: The Relationship between Overlying Synoptic-Scale Flows and Winds within a Valley. *J. Appl. Meteorol.*, **32**, 1669–1682, https://doi.org/10.1175/1520-0450(1993)032<1669:TRBOSS>2.0.CO;2.